Dynamics of Antibodies in Solution: from Individual Proteins to Phase Separation Domains

Dissertation

der Mathematisch-Naturwissenschaftlichen Fakultät

der Eberhard Karls Universität Tübingen

zur Erlangung des Grades eines

Doktors der Naturwissenschaften

(Dr. rer. nat.)

vorgelegt von

Anita Girelli
aus Soave, Italien

Tübingen
2022

Gedruckt mit Genehmigung der Mathematisch-Naturwissenschaftlichen Fakultät der Eberhard Karls Universitübingen.

Tag der mündlichen Qualifikation:	22.09.2022
Dekan:	Prof. Dr. Thilo Stehle
1. Berichterstatter:	PD Dr. Fajun Zhang
2. Berichterstatter:	Prof. Dr. Martin Oettel

A Carla Girelli

Abstract

Antibodies are a fundamental part of the immune system. They are injected subcutaneously to treat different diseases, such as SARS-CoV-2. The concentration of antibodies of these solutions is elevated, to minimize the number of injections. It is important to study these highly concentrated solutions to avoid unwanted behavior, for example aggregation, phase separation or very high viscosity, which do not permit a painless injection. Phase separation is a type of phase transition that has been studied for many years by various disciplines, such as physics, chemistry, biology and engineering. In recent years it was discovered that phase separation is ubiquitous in cells, and in general in biological organisms. The phase separation of a solution starts at the molecular level, where the particle-particle interactions induce the formation of domains, which then grow with time until, eventually, the system reaches macroscopic phase separation. It has been shown that this process can be slowed down to the point where the growth of the domains is arrested. To obtain this, the molecular diffusion properties of the two phases have to be very different, meaning that the value of the mobility of the particle in one of the two phases has to be much smaller than in the other. By controlling these phenomena, it is possible to tune the morphology of the system to grant, for example, specific mechanical properties to the system. However, the mechanism through which the mobility is reduced is not completely understood.

In this thesis, the diffusion of antibodies is probed while in aqueous solution with polymers. The dynamics is monitored on different time and length scales to identify which type of motion the particles are subjected to. With this, we hope to clarify the connection between the microscopic and macroscopic properties of the solution. To achieve this, we probed the solution during phase separation and in the single-phase state with neutron, light and X-ray scattering techniques.

In the first study the system was probed on a micrometer length scale via light and X-ray scattering. The intensity collected via small angle scattering shows a typical spinodal peak, with which the kinetics of the phase separation can be monitored. For deep quenches, the phase separation is slowed down, reaching an almost complete arrest of the growth within

the experimental time frame. The correlation functions collected via X-ray photon correlation spectroscopy during the phase separation show that two relaxation modes are present. Both of them have typical characteristics of ballistic motion as seen for colloidal gels. When measuring the system in the one-phase region via dynamic light scattering, the correlation functions show two decays as well. However, the type of diffusion is different: The fast mode, which we interpret as the diffusion of the monomers, indicates Brownian motion. The slow mode is more difficult to interpret due to the high concentration of the solution. The experimental results during the phase separation are compared with simulated data based on the Cahn-Hilliard equations. Qualitative comparability is obtained only if a strong dependence of the mobility on protein concentration is introduced. The limitations of the model are visible and we speculate that they are due to the lack of visco-elasticity in the model.

In the second study, the diffusion on molecular length scale and below was measured with quasi-elastic neutron spectroscopy. The signal was collected at three different temperatures, i.e. when the solution is 1) in a single phase, 2) in phase separation and 3) in arrested phase separation. In the two latter states, the dense phase, which occupies the majority of the volume and has a higher concentration, is the main contributor to the overall signal. This means that the system can be monitored while the concentration increases, providing an estimate of the change of the diffusion coefficient with protein concentration. The results further validate the results of the first study, as the diffusion coefficient has a strong dependence on protein concentration. A discrepancy between the temperature dependency of the diffusion coefficient we obtain via neutron spin echo and neutron back-scattering is evident. This can be explained considering the different length scales covered by the two methods via a simple model which takes into account the motion of the lobes of the protein. According to this model, while the global diffusion of the protein is strongly affected by the crowding, the single lobes' motion is not hindered to the same extent since their size is smaller.

In the third study, the measurements performed on a molecular length scale, as in the second study, but with the goal of accessing the long-time diffusion and not the short-time as done in the previous study. To access these large time scales ($\gtrsim 500$ ns) X-ray photon correlation spectroscopy was employed. To have a sufficient signal the photon density on the sample has to be much larger than the first study, which implies a much higher dose on the sample. Beam effects on the structure and the diffusion of the particles are observed and quantified. Although the dynamics is influenced by X-ray effects, it is possible to see that the correlation is not completely lost, meaning that the decay time is in a time range above seconds. Furthermore, the samples in the arrested state presents q dependent aging. At large q, the diffusion does not

seem to be dependent on waiting time, which is consistent with the absence of aging seen in the second study on the short-time diffusion. This is a clear difference with the results of the simulations of colloidal system.

In conclusion, we connect the kinetics and dynamics of phase separation with the molecular diffusion of the proteins via the Cahn-Hilliard equation. The model we used describes the kinetics and qualitatively the dynamics of the phase separation. The diffusion on micrometer length scale is of different type in the single phase and in the phase separation region, but, interestingly, it does not show a sharp transition between a classical phase separation and an arrested phase transition. This suggests a smooth transition between the liquid state to the gel state.

Kurzfassung

Antikörper sind ein wesentlicher Bestandteil des Immunsystems. Sie werden zur Behandlung verschiedener Krankheiten, wie z. B. SARS-CoV-2, subkutan injiziert. Die Konzentration der Antikörper in diesen Lösungen ist hoch, um die Anzahl der Injektionen zu minimieren. Es ist wichtig, diese hochkonzentrierten Lösungen zu untersuchen, um unerwünschtes Verhalten zu vermeiden, z. B. Aggregation, Phasentrennung oder sehr hohe Viskosität, das eine schmerzfeie Injektion verhindert. Phasentrennung ist eine Art von Phasenübergang, die seit vielen Jahren von verschiedenen Disziplinen wie der Physik, Chemie, Biologie und dem Ingenieurswesen untersucht wird. Daher ist bekannt, dass Phasentrennung in Zellen und und biologischen Organismen im Allgemeinen allgegenwärtig ist. Die Phasentrennung einer Lösung beginnt auf molekularer Ebene, wo die Teilchen-Teilchen-Wechselwirkungen die Bildung von Domänen hervorrufen. Diese wachsen dann mit der Zeit, bis das System schließlich eine makroskopische Phasentrennung erreicht. Es wurde gezeigt, dass dieser Prozess soweit verlangsamt werden kann, bis das Wachstum der Domänen gestoppt wird. Um dies zu erreichen, müssen die molekularen Diffusionseigenschaften der beiden Phasen sehr unterschiedlich sein, das heißt, die Mobilität der Teilchen in einer der beiden Phasen muss viel kleiner sein als in der anderen. Durch die Steuerung dieses Phänomens ist es möglich, die Morphologie des Systems zu beeinflussen, um dem System beispielsweise bestimmte mechanische Eigenschaften zu verleihen. Der Mechanismus, durch den die Mobilität verringert wird, ist jedoch nicht vollständig geklärt. Während einige Forschungsarbeiten darauf hindeuten, dass das Phänomen auf den Glasübergang zurückzuführen ist, vermuten andere, dass es sich um einen Gelübergang handelt, der die Mobilität einer der beiden Phasen verringert.

In dieser Arbeit wird die Diffusion eines Gemischs aus einem Antikörper und einem Polymer in Lösung auf verschiedenen Zeit- und Längenskalen untersucht, um zu klären, welcher Art von Bewegung die Teilchen unterworfen sind. Damit hoffen wir, den Zusammenhang zwischen den mikroskopischen und makroskopischen Eigenschaften der Lösung klären zu können. Um dies zu erreichen, haben wir die Lösung während der Phasentrennung und in der Einzelphase mit Neutronenstreuung, Lichtstreuung und Röntgenstreuung untersucht.

In der ersten Studie wurde das System auf einer Mikrometer-Längenskala mittels Licht- und Röntgenstreuung untersucht. Die Intensität zeigt einen typischen spinodalen Peak, mit dem die Entwicklung der Phasentrennung verfolgt werden kann. Bei tiefen Temperaturabfällen verlangsamt sich die Phasentrennung und erreicht in der Versuchszeit einen fast vollständigen Stillstand des Wachstums. Die Korrelationsfunktionen, die mittels Röntgenphotonenkorrelationsspektroskopie während der Phasentrennung gesammelt wurden, zeigen, dass zwei Relaxationsmechanismen vorhanden sind. Beide haben die typischen Merkmale einer ballistischen Bewegung, wie sie für kolloidale Gele charakteristisch sind. Bei der Messung des Systems im einphasigen Bereich mittels dynamischer Lichtstreuung zeigen die Korrelationsfunktionen ebenfalls zwei Abklingvorgänge, aber die Art der Diffusion ist unterschiedlich, wobei der schnellere der beiden auf eine Brownsche Bewegung hindeutet. Die experimentellen Ergebnisse werden mit simulierten Daten auf der Grundlage der Cahn-Hilliard-Gleichungen verglichen. Qualitative Vergleichbarkeit wird nur erreicht, wenn eine starke Abhängigkeit der Mobilität von der Proteinkonzentration besteht. Die Einschränkungen des Modells sind erkennbar, und wir vermuten, dass sie auf das Fehlen von Viskoelastizität im Modell zurückzuführen sind.

In der zweiten Studie wurde die Diffusion auf der molekularen Längenskala und darunter mit quasi-elastischer Neutronenstreuung gemessen. Das Signal wird bei Temperaturen erfasst, bei denen sich die Lösung in 1) einer einzigen Phase, 2) in der Phasentrennung und 3) in der gestoppten Phasentrennung befindet. In den beiden letztgenannten Zuständen ist die dichte Phase, die den größten Teil des Volumens einnimmt und eine höhere Konzentration aufweist, der Hauptfaktor für das Gesamtsignal. Dies bedeutet, dass das System untersucht werden kann, während die Konzentration steigt, was eine Schätzung der Änderung des Diffusionskoeffizienten in Abhängigkeut der Proteinkonzentration ermöglicht. Die Ergebnisse bestätigen die Resultate der ersten Studie, da der Diffusionskoeffizient eine starke Abhängigkeit von der Proteinkonzentration aufweist. Vergleicht man die Ergebnisse, die mittels Neutronenspinecho und Neutronenrückstreuung erzielt wurden, so zeigt sich eine Diskrepanz zwischen der Temperaturabhängigkeit des Diffusionskoeffizienten. Dies lässt sich unter Berücksichtigung der unterschiedlichen Längenskalen, die von den beiden Instrumenten abgedeckt werden, durch ein einfaches Modell erklären, das die Bewegung der Lappen des Proteins berücksichtigt. Diesem Modell zufolge wird die globale Diffusion des Proteins durch die Verdichtung stark beeinträchtigt, während die Bewegung der einzelnen Lappen nicht in gleichem Maße behindert wird, da ihre Größe geringer ist.

In der dritten Studie wurden die Messungen auf der selben molekularen Längenskala wie in

der zweiten Studie durchgeführt, jedoch mit dem Ziel, die Langzeitdiffusion zu erfassen. Für den Zugang zu diesen großen Zeitskalen ($\gtrsim 500\,\mathrm{ns}$) wurde Röntgenphotonenkorrelationsspektroskopie eingesetzt. Um ein ausreichendes Signal zu erhalten, muss die Photonendichte auf der Probe viel höher sein als in der ersten Studie, was eine viel höhere Strahlendosis auf der Probe impliziert. Die Auswirkungen des Strahls auf die Struktur und die Diffusion der Teilchen werden beobachtet und quantifiziert. Obwohl die Dynamik durch Strahleinflüsse beeinflusst wird, ist es möglich zu sehen, dass die Korrelation nicht vollständig verloren geht, was bedeutet, dass die Abklingzeit in einem Zeitbereich über Sekunden liegt. Außerdem zeigen die Proben im arretierten Zustand eine q-abhängige Alterung. Bei großen q-Werten scheint die Diffusion nicht von der Wartezeit abhängig zu sein, was mit dem Fehlen der Alterung in der zweiten Studie übereinstimmt, was einen deutlichen Unterschied zu den Ergebnissen der Simulationen des kolloidalen Systems darstellt.

Zusammenfassend lässt sich sagen, dass wir die Kinetik und Dynamik der Phasentrennung über die Cahn-Hilliard-Gleichung mit der molekularen Diffusion der Proteine verbinden. Das von uns verwendete Modell beschreibt die Kinetik und qualitativ die Dynamik der Phasentrennung, wahrscheinlich aufgrund der fehlenden Berücksichtigung der viskoelastischen Eigenschaften im Modell. Die Diffusion auf der Mikrometerskala zeigt verschiedene Arten der Diffusion in der Einzelphase und in der Phasentrennungsregion, aber interessanterweise keinen scharfen Übergang zwischen einer klassischen Phasentrennung und einem festgehaltenen Phasenübergang. Dies deutet auf einen sanften Übergang zwischen dem flüssigen Zustand und dem Gelzustand hin.[1]

[1]Ich danke Alessandro Greco und Zarah Weiss für ihre Unterstützung bei der Übersetzung des Abstracts ins Deutsche.

Contents

Part I

Scientific Background

Chapter 1

Introduction

This chapter covers the fundamentals and theory on protein liquid-liquid phase separation. It is divided in two parts, where the first one provides an introduction on the phase behavior of protein systems, including theories and recent studies to understand and predict the evolution of liquid-liquid phase separation (LLPS). The second focuses on the diffusion of particles during LLPS.

1.1 Liquid-liquid phase separation in protein solution

LLPS is ubiquitous in nature as well as in our everyday life. An everyday example of this phenomenon is when oil naturally separates from water or vinegar in a salad dressing. In the same way other solutions can separate into multiple coexisting liquid phases. This is a thermodynamically driven transition that can be due to the interaction of particles with the solvent, or the interaction between one or more species of particles, or a combination of the two [1]. The entropic loss caused by the separation into two phases is balanced by the energy gain due to the inter-molecular interaction. For this reason, the molecules start to separate microscopically, and increase the size of the domains with time until macroscopic separation occurs.

LLPS was studied in different disciplines: chemistry and physics by researchers like van der Waals, [2], Landau [3], Cahn and Hilliard [4] to obtain a general, fundamental understanding of this phenomenon. LLPS has also been studied in the context of engineering to explore the possibility of producing materials with tunable properties, and lately also biology [5]. The fact that liquid droplets are present in living cells was already observed a long time ago [6], but only recently the connection between such droplets and LLPS has been established [7].

Before that, ther studies of biological materials showing phase separation had been conducted, such as for α-crystallin solutions [8] as well as for phospholipid membranes [9], but never in vivo. After the realization that the P granules in the nucleus are, indeed, liquid and can dissolve or condense [7], LLPS was observed in many other parts of the cell such as in the cytoplasm [10] and in the plasma membrane [11] (for more details see Ref. [12]). The number of systems in which LLPS was observed has become so large that six different databases have been developed [13], in order to obtain a more general understanding of this phenomenon. LLPS has not only been linked physiological conditions, but also to pathological ones, for example to the development of cancer and neurodegenerative and inflammatory diseases [12].

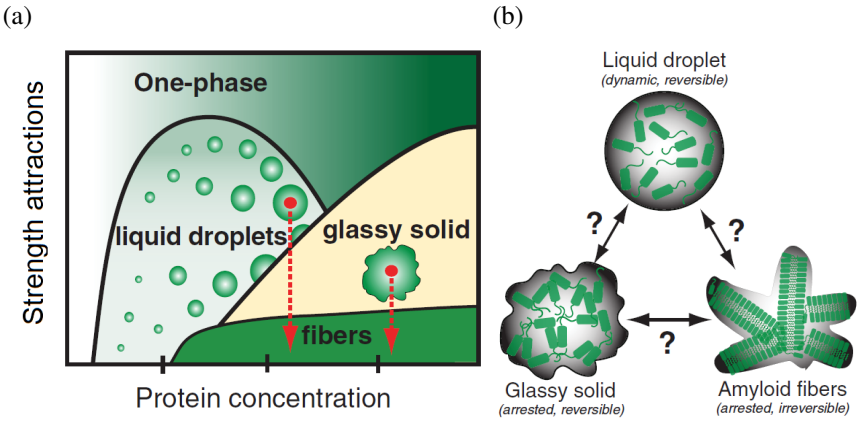

Figure 1.1: a) Phase diagram of a generic biological system. Depending on the position within the phase diagram the solution can be stable as a single phase, phase separate, undergoes arrested phase separation into a glassy phases and/or fibers form. b) Depending on the conditions, a protein can condense into different high-order structures such as liquids, glassy solids, or amyloid fibers. Images taken from Ref. [14].

These neurodegenerative diseases are due to the formation of amyloid fibers, which seems to nucleate within the dense phase of the LLPS [14; 15] (Fig. 1.1). When the concentration of protein in the dense phase is very large, it is possible that the condensates, also called dense domains, become glassy solids, which are dynamically arrested. These objects are reversible, i.e. they can desolve upon decreasing the interaction strength. However, in vitro studies show that this reversibility is limited to a few cycles and afterwards aggregation and finally fiber formation occurs [16]. It is, hence, important to understand the properties of this glassy solid condensates to establish their connection to the fibrillization (Fig. 1.1b). The complexity of biological systems, which are highly crowded and include many different components and

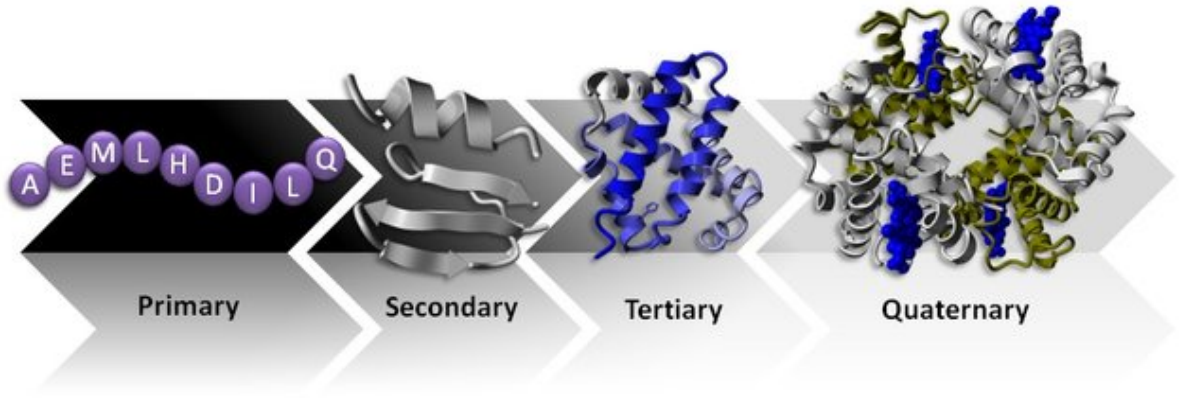

Figure 1.2: Depiction of the different structures that compose a protein. The image is from Ref. [20].

types of interaction between particles, hinder a comprehensive theoretical description of the condensates. However, soft matter physics approaches have been successful to understand the overall behavior of the solution during LLPS [17] by considering only a limited number of components and simplifying their interactions. A long-standing approach to describe proteins in physical terms is to consider them colloids [18]. This gives the possibility of making use of the extensive literature on phase diagrams in colloidal physics [19]. Given its importance, the next section will focus on this topic.

1.1.1 Proteins as colloids

Proteins have a complex and hierarchical structure (Fig. 1.2). They are composed of long chains of small building blocks, the amino acids. The length and the order of the amino acids in the chain, also called sequence, forms the primary structure and it determines all the characteristics of the protein. The interaction between the amino acids permits the formation of structures like α-helices or β-sheets, which composed the so called secondary structure of the protein. The three dimensional arrangement of these structures is giving the tertiary structure of the protein. A protein can be composed of more than one chain, in that case the arrangement of the different subunits is called quaternary structure. The quaternary structure, or tertiary in case of proteins composed only by one chain, is responsible for the shape of the protein.

In principle, to have a precise description of the system, it is necessary to take into account the movement and interactions of each atom of the proteins with the other proteins atoms,

the atoms of the solvent, and ions all the ions present in the solution. However, this is not the most efficient way to approach the problem, since many of this interactions are not relevant for predicting the phase diagram. The simplest approximation is to consider the proteins as spherical objects with some effective potential between them, which describes the interactions between the proteins. This has the advantage of being able to provide a theoretical framework developed for other spherical colloids which were already investigated. Colloids are suspended particles that have a size larger than atoms, do not precipitate and are not visible by eyes, meaning that their size is in the range between 1 nm and 1 µm. In colloidal science, often, the predictions of phase diagrams are estimated for colloids which are spherical and rigid. Different types of effective interactions have been used to describe the pair potential of two particles [21], some of them are: a) hard spheres with only repulsions that prevent interpenetration between particles, b) sticky hard spheres and square well potential which include an attractive well,c) a potential derived from the DLVO (Derjaguin-Landau-Verwey-Overbeek) theory, d) Yukawa potential which is an exponentially decaying function which can be in principle attractive or repulsive, but it is more often used as a double Yukawa potential, meaning two exponential decays one being attractive and one repulsive. The most relevant type of interaction for the investigation in this thesis is the Asakura and Oosawa theory, which describes depletion forces, meaning the forces induced by entropic effects, which are present in solutions of a mixture of colloids and non-absorbing polymers [22]. Polymer-protein mixtures have been extensively studied, because the addition of polymers to protein solutions induces not only phase separation, but also crystallization [23]. For this reason, it is easy to find colloidal approaches for these protein systems to understand their phase diagrams [24].

The predicting power of colloidal science as a tool to estimate protein phase behavior is further extended by the law of corresponding states [25]. This law states that the phase diagrams of different systems, which have different types of short range attractions and repulsions, are overlapping in a diagram in which the axes are volume fraction and reduced second virial coefficient B_2^*, which is the second virial coefficient normalized by the value second virial coefficient of the hard sphere with radius given by the effective radius of the particles. In other words, the details of the pair potential are not relevant for the qualitative determination of the phase diagram. This implies that the phase diagram can be predicted without knowing the type of interactions inside of the system, but simply by the value of B_2^*, which can be estimated experimentally for example via dynamic light scattering. The law of corresponding states was proved not only for generic spherical colloids, but also specifically for proteins [26].

A typical phase diagram of a protein system obtain from a colloidal science via Monte Carlo simulations or statistical mechanics approaches and validated by experimental data is depicted in Fig. 1.3 [27; 28; 18].

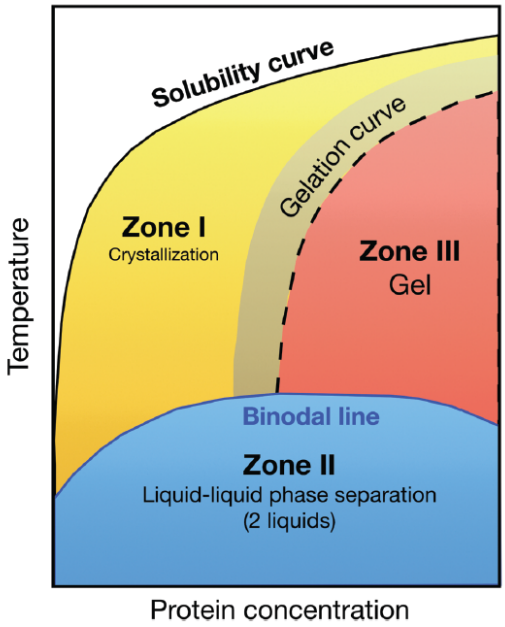

Figure 1.3: A generic phase diagram of a protein system. The samples in blue region, i.e. below the binodal line, separate into a dense and a dilute phase. Below the solubility line, the samples are metastable with respect to crystallization. The image was taken from Ref. [18].

While this approach can give many insights, like predicting the crystallization of proteins [27; 29], it is nevertheless only an approximation. An example of a system in which the approximation is not always valid is the protein investigated in this thesis, γ-globulin. This protein is an antibody, which is not spherical, but Y-shaped, and it is soft, meaning that the shape is not fixed and it is possible that two particles interpenetrate. Moreover, the pair potential is not necessarily isotropic. On the contrary, the directionality of the interactions is to be expected given its biological function, which requires the protein to selectively bind to certain molecules. It was shown that pure monoclonal antibodies solution have an LLPS region, which is broader on the high concentration branch in comparison with globular proteins [30; 18]. This suggests that the colloidal approximation is not holding for this protein. However, with the addition of Poly(ethylene glycol) (PEG), NaCl and using polyclonal antibodies the phase diagram is again symmetric [31], probably because the depletion interaction induced by the polymers is stronger than protein-protein interaction and it is isotropic. In conclusions,

it is not easy to predict if the colloidal approximation holds or not, and each case has to be evaluated separately.

1.1.2 Spinodal decomposition and Cahn-Hilliard equation

Given that most of experiments performed in the thesis were performed in the spinodal region of the phase diagram it is worth focusing on the theory and description of the evolution of the phase separation. This section was adapted from Refs. [1; 32].

As described in the previous sections, phase separation is thermodynamically driven. Hence, to be able to describe it, it is necessary to start from free energy of the system. This is dependent on the interaction between its components, which determines the internal energy U of the system and by their entropic contribution S, so that $F = U - TS$, with T being the temperature of the solution. Some estimations of F have already been done for colloid-polymer mixtures [33]. However, here, a simpler treatment is considered in which only the first terms of a Taylor expansion of the free energy are considered, following Landau's approach, to capture the physics of the phase separation. In this case [3] the free energy density is

$$F(c(\vec{r},t)) = F_0 + A(T - T_c)(c(\vec{r},t) - c_{crit})^2 + B(c(\vec{r},t) - c_{crit})^4, \tag{1.1}$$

where $c(\vec{r},t)$ is the protein concentration in position $\vec{r}$ at time t, and F_0, A, B, c_{crit} and T_c are constants. The linear and cubic terms are not present in Eq. 1.1, because of symmetry reasons, since it should be analogous to the free energy of a binary mixture, where the free energy is an even function of the control parameter $c - c_{crit}$.

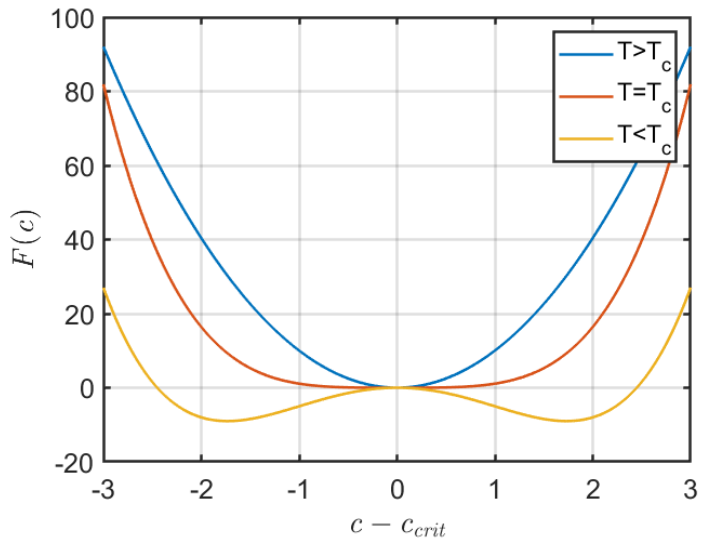

Figure 1.4: Free energy density for temperatures above, below and at the critical temperature T_c as a function of the concentration fluctuations $c - c_{crit}$ with Landau theory.

This is not necessarily true for any system, but some characteristics of Eq. 1.1 (Fig. 1.4) are generalizable:

- for $T > T_c$, the system is stable.
- for $T = T_c$, i.e. the system is at its critical temperature, there are strong concentration fluctuations and the equilibrium concentration is at c_{crit}.
- for $T < T_c$, the system has more than one equilibrium point, and they are different from c_{crit}.
- for $T < T_c$, three regions can be identified: The first one is at $c \sim c_{crit}$ the curvature of F is negative, hence an instability point. The other two regions can be found for a concentration in which $\mid c - c_{crit} \mid$ is larger. Here, the curvature of F becomes positive, which indicates the presence of a metastable state.

The spinodal region is defined as the region in which the curvature of F is negative. In this part of the phase diagram, the solution spontaneously phase separates into two phases. The value of the concentration of these two phases corresponds to the minima of F.

The time evolution of the concentration $c(\vec{r},t)$ has to follow the continuity equation (or otherwise called transport equation), which states that

$$\frac{\partial c(\vec{r},t)}{\partial t} + \vec{\nabla} \cdot \vec{j}(\vec{r},t) = 0, \tag{1.2}$$

with $\vec{j}(\vec{r},t)$ being the concentration current density. The concentration current is here assumed to be linked to the chemical potential $\mu(\vec{r},t)$ and the mobility M through the following equation

$$\vec{j}(\vec{r},t) = -M\nabla\mu(\vec{r},t). \tag{1.3}$$

For thermodynamical considerations, the chemical potential can be calculated as the derivative of the Helmholtz free energy $\mathcal{F}(c(\vec{r},t))$ with

$$\mu(\vec{r},t) = \frac{\delta\mathcal{F}(c(\vec{r},t))}{\delta c(\vec{r},t)}. \tag{1.4}$$

The Helmholtz free energy is connected to the free energy of Eq.1.1 via

$$\mathcal{F}(c(\vec{r},t)) = \int \frac{F(c(\vec{r},t))}{k_b T} + \frac{1}{2}\kappa^2(\nabla c)^2 d\vec{r}, \tag{1.5}$$

where T is the temperature and k_b is the Boltzmann constant. The term $\kappa^2(\nabla c)^2$ in Eq. 1.5 accounts for the free energy cost of inhomogeneous concentration distributions, in which κ is a constant. Inserting Eq. 1.5 into Eq. 1.4, we obtain

$$\mu(\vec{r},t) = \left(\frac{\partial F}{\partial c}\right)_T - \kappa^2 k_b T \nabla^2 c(\vec{r},t). \tag{1.6}$$

This expression for the chemical potential can be inserted into Eq. 1.3 to finally obtain the Cahn-Hilliard equation

$$\frac{\partial c(\vec{r},t)}{\partial t} = \vec{\nabla} \cdot \left[M \left(\nabla \left(\frac{\partial F}{\partial c} \right)_T - \kappa^2 k_b T \nabla^2 c(\vec{r},t) \right) \right]. \tag{1.7}$$

If we introduce the restriction that the mobility is a constant $M = \mu_0$, and renormalize the equation to reduce the number of constants [34; 35], the equation becomes

$$\frac{\partial \phi(\vec{r},t)}{\partial t} = \mu_0 \nabla^2 (\phi^3 - \varepsilon\phi - \nabla^2\phi). \tag{1.8}$$

The variable ε here is setting the quench depth, and $\phi(\vec{r},t)$ is a normalised concentra-

tion. This equation cannot be analytically solved. Nevertheless, a solution for $t \sim 0$ can be found through linearization. The concentration for very small times can be approximated by the initial concentration with the addition of a small concentration change $\delta\phi(\vec{r},t)$, hence, $\phi(r,t) = \phi_0 + \delta\phi(\vec{r},t)$. After inserting this equation into Eq. 1.7 and performing a spatial Fourier transform, the relation can be written as

$$\frac{\partial \delta\tilde{\phi}}{\partial t} = -\mu_0 q^2 (q^2 - \varepsilon + 3\phi_0^2)\delta\tilde{\phi}, \tag{1.9}$$

with $\delta\tilde{\phi} = \frac{1}{2\pi}\int \delta\phi(\vec{r},t)\exp(i\vec{q}\vec{r})d\vec{r}$.

The Fourier transform is not only useful to find a mathematical solution, but has a physical relevance since it is providing a connection with a measurable quantity that is the scattering intensity $I(q)$, which is the Fourier transform of the concentration of the sample. The solution $\delta\tilde{\phi} = \exp(R(q)t)$, can be rewritten in terms of intensity simply by adding a multiplying factor, with the result that

$$I(q,t) = A\exp(R(q)t). \tag{1.10}$$

The parameter $R(q)$ is given by $R(q) = -\mu_0 q^2(q^2 - \varepsilon + 3\phi_0^2)$. The phase separation is strongly dependent on this function, since it sets the region in which the intensity increases ($R(q) > 0$) or decreases ($R(q) < 0$). In case that $R(q) < 0$ at all values of q, the phase separation cannot occur. Otherwise the curve shows a peak as shown in Fig. 1.5. As a consequence the intensity curve will also show a peak, called spinodal peak.

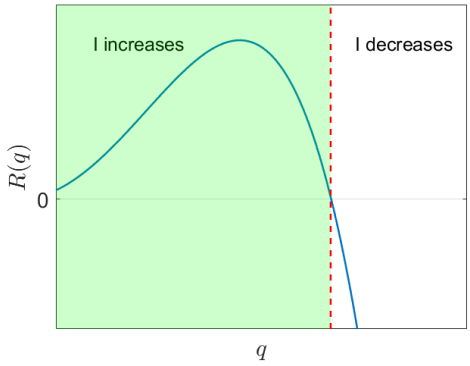

Figure 1.5: The curve $R(q)$, the green shaded area highlights the q values for which the intensity is increasing and the red dashed line show the point at which $R(q) = 0$ and the intensity is constant.

After the initial stage, non-linear terms start to contribute, and Eq. 1.10 is no longer fulfilled. In this stage, the domains of dense/dilute phase are formed and successively grow in size. The growth of the domains, referred also as coarsening, can be described by different models [36; 37; 38].

1.1.3 Arrested liquid-liquid phase separation

Even if phase separation has been studied for a long time, many aspects are still not clear. One of them is the arrested phase separation: this phenomenon arises when the diffusion properties, more specifically the diffusion coefficient, of the dilute and the dense phase strongly differ [39]. This is possible, for example, when the dense phase has a concentration so elevated that it is close to the glass transition concentration (see Fig. 1.6). In this case, after the initial stage of the phase separation where the domains form, the growth of the domains arrests. Here, two processes are competing: on the one hand the system is out of equilibrium and the concentration of the dense phase has to increase to reach the equilibrium concentration. On the other hand, the protein concentration reaches values so elevated that the proteins cannot move freely anymore. This results in the slowing down of the kinetics of the phase separation to the extent that the equilibrium concentration cannot be reached [40; 41]. In these cases, the dense phase forms an interconnected network of particles in which domains of dilute phase are embedded, and gives rise to a gel state. Depending on the distance from the glass line (Fig. 1.6), the phase separation kinetics is more or less affected by it. The two extreme case are: 1) the phase separation is not affected by the glass line (as represented in Fig. 1.6 with the shallow quench from the inital fluid phase) and 2) the phase separation is arrested (in the figure the quench to a lower temperature). The closer the quench is to the glass line, the slower is the kinetics of the phase separation.

A model system often used for obtaining an arrested phase separation is a polymer-colloid mixture. The colloid-colloid interaction is mediated by the polymers through depletion interaction, which have the advantage of being highly tunable [43; 44; 45]. In fact, the strength of the attractions can be controlled by changing the polymer concentration and the size of the polymer determine the range of the attractive potential [44]. The studies performed on polymer-colloid mixtures cover simulations, including Newtonian dynamics, Brownian dynamics [46; 47], coarse grained approaches [48; 34; 35], mode coupling theory [49; 50], and experiments [51; 52].

Protein systems show arrested phase transition as well. The most known system is lysozyme

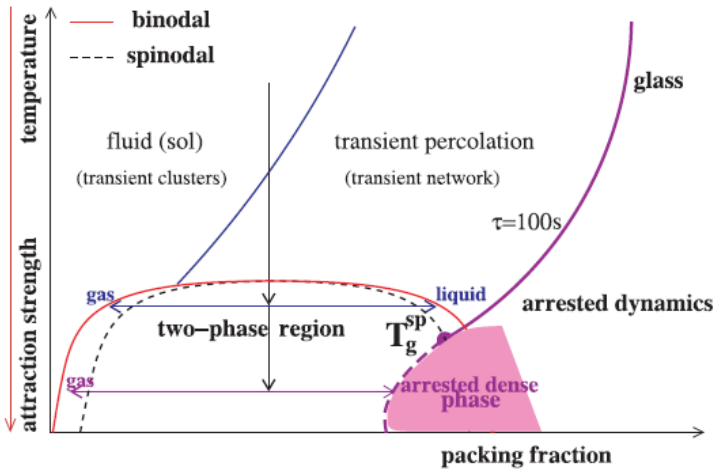

Figure 1.6: Representation of the phase diagram of a system presenting arrested spinodal decomposition from Ref. [42].

[53; 54]. However, also proteins such as γ-crystallin [8; 55; 56], tau protein [57], casein micelles [58; 59] and gluten [60] have been reported to arrest upon phase separation. Previous work in our group shows an arrested phase transition in two other protein systems: Bovine serum albumin with trivalent salts and γ-globulin with PEG [61; 31; 62]. Understanding arrested LLPS in protein systems is not only important for medical reasons as already outlined in the beginning of this section, but also for the application in food industry. Here it is important because it allows to form reversible gels with tunable mechanical properties [63; 59; 64; 65].

An experimental technique that is commonly used to monitor the kinetics of the arrested phase separation is small angle scattering. With this scattering technique, it is possible to monitor the evolution of the size of the domains by following the domain-domain correlation peak. This peak, also called spinodal peak, grows in height with time, and at the same time its position q_{max} moves to lower values of q. For an arrested spinodal decomposition or close to it, the peak growth is strongly reduced, and can be almost completely stopped depending on the position in the phase diagram. Following the correlation length $\xi = \frac{2\pi}{q_{max}}$, one obtains an estimate on the size of the domains. Hence, it is possible to use it to characterize the degree of the kinetics slowdown.

In previous studies on the system investigated in this thesis, namely water solution of γ-globulin and PEG, the phase diagram and the kinetics of the phase separation were characterized [31]. As shown in Fig. 1.7, at the lowest protein concentration $\xi \propto t^{1/3}$ as expected from a classical spinodal decomposition for all the quench temperature above 4°C. For the remain-

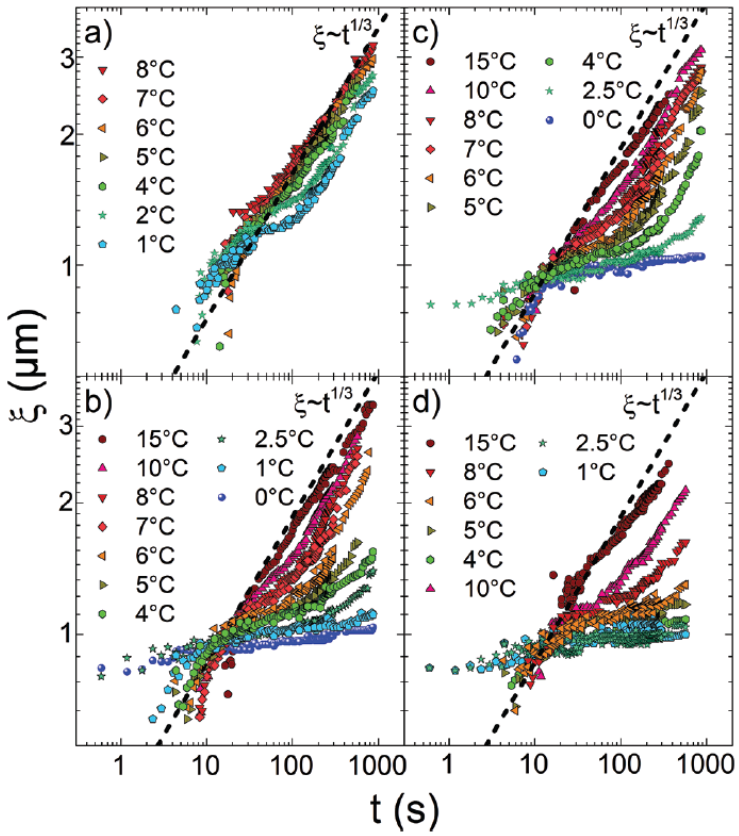

Figure 1.7: The time dependence of the correlation length ξ for a sample with a) 220 $\pm$ 30 mg/ml Ig and 3.8 $\pm$ 1.2 % PEG, b) 230 $\pm$ 30 mg/ml Ig and 4.3 $\pm$ 0.9 % PEG, c) 246 $\pm$ 20 mg/ml Ig and 4.4 $\pm$ 1.2 % PEG, d) 295 $\pm$ 30 mg/ml Ig and 2.7 $\pm$ 1.1 % PEG. The dashed line shows $\xi \propto t^{1/3}$. The image was taken from Ref. [31].

ing temperatures, a deviation from this proportionality is visible for a limited time interval. A similar trend was seen in colloidal systems which present a transient gel [66]. At higher protein concentrations, the temperature below which the deviation is visible is higher. Also the time interval where the deviation is present becomes larger, because the time in which the system is in a gel state increases. At the highest protein concentration and for the lowest temperatures, the peak position is almost constant and in the measured time the $\xi \propto t^{1/3}$ behavior is not recovered, indicating an arrested spinodal decomposition. This study indicates that by varying protein and PEG concentration, it is possible to obtain a transient or stable gel.

1.2 Protein diffusion in solution

The goal of this section is to provide the background knowledge to understand the diffusion of proteins during phase separation. To achieve this, the diffusion of proteins in solution is discussed from its basics, starting with the diffusion of globular proteins in simple liquids. The following part addresses specifically the study of the diffusion of antibodies in aqueous solution, and the information that can be retrieved by probing antibodies with scattering techniques. In the third part, the diffusion during (arrested) phase separation is treated considering not only protein solutions, but also colloid-polymer mixtures and in general colloidal particles with short range attractions. The last part of this section covers soft matter systems in which the diffusion was probed via XPCS. It focuses on systems which are related to the sample investigated in this thesis, namely colloidal suspensions, phoretic motion during phase separation, colloidal gel transition, and glass transition and the biological samples measured until now.

1.2.1 Diffusion of proteins in equilibrium solutions

Proteins have many widely different biological functions. They can have a structural functions like collagen, one of the most abundant protein in our body, or they act as pumps to permit the passage of proteins through membranes [67]. For many of them their function depends on their diffusion, for example enzymes, which enable some reaction, or proteins which act as carriers or signaling particles [67]. It is therefore biologically relevant to understand how to control their diffusion and hence their function.

The term diffusion of a particle does not define one specific motion, in fact depending on the time and the length scale probed different diffusion processes can be observed. This is true for spherical rigid objects, and for proteins, with their hierarchical structure, the complexity increases even further. To understand which type of motion a single rigid spherical particle is subjected to, typical times are defined and used as landmarks. The shortest one is the relaxation time of the solvent at $t_{\text{solvent}} \sim 10^{-14}$ s, the moving solvent molecules come in contact with the particles, and thus apply random forces which change with a typical time t_{solvent}. This is not the only effect that the solvent has on the particles, in fact once the particles are moving they will collide with the solvent molecules, which results in an overall friction force on the particle. This leads to the second important time scale, i.e. the typical time at which friction forces on a particle are noticeable $t_f = \frac{M}{\gamma}$ with M being the mass of the particle

and γ the friction coefficient. Hence, there is a time $t_{\text{solvent}} \ll t \ll t_f$, in which the particles are almost freely moving and their motion is ballistic, thus their mean square displacement has the following time dependence: $\langle \mid \vec{R}(t=0) - \vec{R}(t) \mid^2 \rangle \propto t^2$. At a time t_d with $t_d \gg t_f$ the friction forces do act on the particles and their movement can be described as Brownian with the mean square displacement depending linearly on time. This picture changes again when the time increases to an extent that the presence of other particles in the solution cannot be ignored. The particle at this time scale interacts with the neighboring particles. This induces a slow down of the diffusion, giving rise to a sub-diffusive regime ($\langle \mid \vec{R}(t=0) - \vec{R}(t) \mid^2 \rangle \propto \sqrt{t}$). The interaction time t_i can be estimated as the time that a particle requires to move a distance equal to its radius, hence $t_i = \frac{R_p^2}{D_0}$ with R_p being the radius of the protein and D_0 the short-time diffusion coefficient. The Brownian diffusion can be restored at $t \gg t_i$, if this is not the case the system will be classified as a system in which there is anomalous diffusion.

The rigid sphere behaviour can also be used as simplification to describe proteins, which was used succesfully especially for folded globular proteins. [68; 18]. Focusing on the time scales in which the particles diffusion follows a Brownian motion, there are many parameters that can control the diffusion, such as temperature, type of solvent, ionic strength, and pair interaction potential which can change the viscosity of the solution [68]. As already discussed in Section 1.1.1, there are many types of possible protein-protein interactions. Here, we will focus only on depletion interaction as it is the most relevant for the system investigated in this thesis. The addition of polymers to the solution changes the diffusion of proteins. This happens as a result of a change in the protein-protein interaction, but also because the polymer hinders the motion of the proteins increasing the crowding of the solution. Many models have been proposed to describe the decrease of the diffusion coefficient due to the addition of polymers by considering an additional hydrodynamical resistance due to the polymers [69], or a model in which the proteins are moving in the solution via jumps [70], however they are limited in describing the protein diffusion [71]. Another model was proposed based on the assumption that the movement of the particles is connected to the probability of finding an opening in the space occupied by the polymer chains [72]. In this model the diffusion coefficient D is

$$D = D_0 \int_{r*}^{\infty} g(r) dr, \tag{1.11}$$

thus it depends on the diffusion coefficient without the addition of polymer D_0, and the integral of $g(r)$, i.e. the probability of finding a space of size r, integrated from the minimum size $r*$

which allows for the particle passage. Assuming that the polymers are straight chains with infinitesimal thickness the previous equation can be rewritten as

$$D = D_0 \exp\left[-\pi\left(\frac{r_p + r_f}{k\phi^{-1} + 2r_f}\right)^2\right], \tag{1.12}$$

where r_p is the radius of the particles, r_f is the radius of the polymer, ϕ is the volume fraction of the polymer, and k depends on polymer and the solvent.

1.2.2 Antibodies diffusion studied with scattering techniques

The diffusion of antibodies has become a point of interest in the scientific community because of the combination of the scientific challenge of predicting the physical properties of particles which deviate in shape and interaction from isotropic colloids, but most importantly because of the relevance in pharmaceutical applications. One of the latest, and possibly the most commonly known, applications of monoclonal antibodies treatment was developed as a treatment against SARS-CoV-2 [73; 74]: The patients receive injections of highly concentrated monoclonal antibodies, which target specific regions of the proteins of SARS-CoV-2. Monoclonal antibodies treatments with sub-cutaneous delivery require the intake of a high number of antibodies [75; 76; 77]. This can be achieved by numerous injections, or by fewer injections with a higher concentration. The second option is clearly more convenient for the patients, but at the same time challenging [78]. In fact, the high concentration can induce aggregation [79; 80], phase separation [81; 82; 83; 84] and can make the solutions too viscous for injection [85]. Understanding how to control the viscosity and the phase behaviour of these solutions is essential to further develop and improve these drugs.

Colloid theories and soft matter approaches have been used to provide a picture for the estimation of the aggregation and rheological properties of highly concentrated antibodies solutions. One strand focuses on the structural properties of the solutions, meaning the conformation of the antibodies and their aggregation [31; 86; 87]. An example of this are the conformational changes that antibodies are subjected to when adding co-solutes like Na_2SO_4 and NaSCN [86]. Not only the conformation is important, but also the interaction between the particles, which can be estimated with small angle scattering curves in terms of the second virial coefficient or the structure factor [88; 89; 90].

A second strand focuses on the rheological macroscopic diffusion mainly with Dynamic Light Scattering (DLS), rheometry and electrophoretic mobility measurements. Here, the

interaction between proteins is estimated to understand the effect of crowding, ionic strength or specific co-solutes to predict the viscosity of the solution [91; 92; 93; 94; 95; 96; 97; 98; 85]

One further point of focus is the molecular diffusion of the antibodies. The typical techniques used are neutron quasi elastic scattering (NBS and NSE) [99; 100; 101], and fluorescence spectroscopy [102]. In this part the point of interest does not lie on the macroscopic properties, but rather in the diffusion of the single proteins to understand the possible movements of the proteins at different concentrations.

These three strands are complementary, hence they are often used together to provide a comprehensive picture. For example, with the combination of molecular diffusion and collective diffusion it was possible to understand the importance of protein–protein friction for the self-diffusion of the antibodies [102]. Another example of successful combination of these strands is the investigation of cluster formation and collective diffusion, where a correlation between cluster formation and viscosity increase was shown [103]. This result is also supported by the theory and by comparisons with other proteins [104].

1.2.3 Diffusion during (arrested) phase separation

To probe the diffusion in a system, the first question that has to be answered is which are the relevant time and length scales in the system. For an (arrested) phase separation the answer to this question is not trivial, not only because the system is out of equilibrium, meaning that the diffusion properties are changing with time, but also because of the different parts composing the system. A complete description of the system can be achieved by monitoring not only the diffusion of the proteins, but also the diffusion and growth of the phase separation domains.

For this reason, this section was divided into different parts: the first addresses the diffusion on molecular length scale, the second discusses the length scale of the domains, and the last focuses on protein systems.

1.2.3.1 Diffusion on the single particles length scale

The diffusion on molecular length scale of colloidal particles undergoing phase separation was studied with simulations [46; 47; 50], as well as with experiments [51; 52; 105; 106; 107].

Simulations with Brownian dynamics and Netwonian dynamics as well as the mode coupling theory show correlation functions that during arrested phase separation change with time after quench at all length scales probed. This is accompanied with the emergence of a plateau in the correlation functions, which indicates the arrest of some of the particles. Its height,

usually called non-ergodicity parameter, has modulations in q, for an effect that is similar to the De Gennes narrowing [108]. Mode coupling theory has been successful in predicting such oscillations [107; 109].

Many of these experiments were performed for colloids with a size that is much larger than the protein investigated in this thesis. Using particles in the range of micrometers permits the investigation of molecular diffusion with both microscopy techniques and light scattering to probe the molecular dynamics. With microscopy the real space images can directly access the motion of the single particles and their collective motion since their size is above the diffraction limit [40; 107]. Furthermore, with light scattering the reciprocal space can be monitored at the particle length scales since the beam wavelength is in the visible spectrum [110].

While in the beginning the molecular dynamics was studied to see the diffusion properties of the molecules or to locate the position of the gel line [110], lately the research concentrates more on the reason why the diffusion coefficient in the dense phase decreases to a very low value. Initially, it was associated with a glass transition [107], but this is not the only possible cause for the decrease of the particles diffusion coefficient [111; 44]. It was recently shown that the arrest is present when the particles are bonding [52], and it was argued that percolation and the dynamical arrest are connected [112; 113; 114; 45; 106], suggesting the mechanical properties are important for the arrest of the particles [52].

1.2.3.2 Diffusion on phase separation domains length scale

Starting with the simulation work of Refs. [115; 116], experimental studies have been performed to show that the correlation curves on the domain length scale are following a scaling law. This permits to predict the correlation curves given the time after quench and the spinodal peak position [117; 118; 119; 120]. In this early application of XPCS, the phase separation was monitored in the late stage, i.e. during the domains coarsening. Here, the correlation function $C(t_1,t_2,q)$ can be fitted with a Bessel function of the second kind [119]. To gain further insight in the system it is useful to look at correlation functions after a time normalization. The natural choice for the normalizing value is the time t_{max} at which the intensity $I(q)$ reaches its maximum value. In fact, in the coarsening regime of the spinodal decomposition, if we select a q-value q_0 that satisfy $q_0 < \frac{2\pi}{\xi(t)}$ with $\xi(t)$ being the domain-domain correlation length, the intensity $I(q_0)$ increases with time. The value of $\xi(t)$ increases with time too, since the domains are becoming larger. The increase of $I(q_0)$ continues until $q_0 = \frac{2\pi}{\xi(t=t_{max})}$. After this time

point $I(q_0)$ decreases because the domains are becoming larger than the probed length scale $\frac{2\pi}{q_0}$. After the time normalization, the correlation curves at different q values overlap to follow a master curve. The decorrelation is due to the movement of the interfaces of the domains, and the underling reason for the normalization is that this movement strongly depends on the size of the domains and on the length scale probed. The value t_{max} takes into account both, since at each q value the intensity reaches its maximum at different time which corresponds to the time at which the domain-domain distance has a value of $\frac{2\pi}{q}$.

In case of an arrested spinodal decomposition the growth of the domains is stopped, hence the rescaling law is not applicable. In those case the diffusion of the domains has to be taken into account. This has been already observed in Ref. [121], where the diffusion of an arrested phase separation of colloidal particles was probed. In the study, the correlation functions show two distinct decays: the fast one has Brownian features, with a quadratic dependence of the decorrelation rate on q, and the authors associate this decay with the thermal fluctuation of the clusters present inside of the dense phase. The slow decay, instead, shows characteristics that indicate an intermittent ballistic motion, to be interpreted as collective motions, as already seen for other colloidal gels [122]. An explanation for this is that the domains show a directional movement due to the internal rearrangement of the gel network.

1.2.3.3 Protein systems

The studies presented until now have focused on colloidal spheres, hence they do not include possible non-isotropic interaction potentials, softness of the particles, and non trivial shape of the particles such as the Y-shape of the protein investigated in this thesis. Therefore the approximation of the proteins could be not correctly describing the system [18; 123]. In this section other studies of protein diffusion close to or in the LLPS region are presented to allow for a comparison with the investigated system.

The diffusion of the protein γ_{II} in the vicinity of the critical point was measured with NSE and quasi-elastic light scattering [124]. In this study, it was shown that the correlation rate Γ has two components as predicted for a phase separating system and their q dependence follows the predicted values [125]. This picture changes if the concentration of the proteins is increased [56]. In this case, the effect of the glass line are visible in the deviation of the expected behavior. While the short time diffusion probed by NSE is not affected by the phase separation, the long time diffusion at much larger length scales shows an arrest.

The diffusion of casein micelles in water solution with PEO during arrested phase separa-

tion was also probed [59; 109]. A comparison between confocal laser scanning microscopy and diffusing wave spectroscopy, shows that the appearance of space-spanning networks with increasing attraction is present as well as a change of microscopic dynamics of the individual particles. Going from fluid clusters to liquid-liquid cluster, the diffusion decreases, but the correlation functions still decay, which is not the case for interconnected clusters [59].

Pig gastric mucus was also studied and the gel properties of the sample were linked to an arrested spinodal decomposition [126]. The decorrelation function of the sample shows a single decay. Its decorrelation time is increasing exponentially with waiting time, and q dependence which suggest ballistic motion.

In a recent study [127] fluorescence recovery after photobleaching (FRAP) was used to probe a mixture of PEG and α-Synuclein. The obtained apparent diffusion coefficient decreases with the age of the sample, suggesting a higher rigidity of the domains due to a change of their viscoelasticity, which can be connected to the aggregation of the proteins.

1.2.4 Diffusion measured via XPCS

Considering that the first measurement of speckles was reported 1991 [128], XPCS is a rather novel technique. In 30 years, the technique developed extensively thanks also to the improvement of the synchrotron sources, in particular the coherence properties of the beam [129]. Different materials can be investigated with it, among others: metallic glasses [130], ionic liquids [131], liquid crystals [132], liquid mixtures [133], and a variety of soft condensed matter systems like polymers [134], colloidal suspensions [135], colloidal gel [136; 133] and glasses [137]. The measurements can be performed in two geometries: transmission with Small Angle X-Ray Scattering (SAXS) and reflection with Grazing Incidence Small Angle Scattering (GISAXS) [138].

In this section, the focus will be on the applications of soft matter systems as they are the relevant part for the work of this thesis, namely transmission studies related to colloids, phase separation and biological samples.

1.2.4.1 Colloidal suspensions

Colloidal suspensions have been measured with XPCS for almost 30 years [139]. While in the first studies the solutions had a relatively low particle volume fraction, i.e. in a simple Brownian motion regime, more recently systems with non-negligible interaction between particles have been investigated [135; 140]. This was achieved by using charged particles [135]

or by increasing the volume fraction [140]. For interacting particles, the diffusion coefficient is dependent on the structure factor $S(q)$ and the hydrodynamics interactions $H(q)$, so that $D(q) = D_0 \frac{H(q)}{S(q)}$. Colloids were studied not only in liquids, but also in ice [141]. In this case the diffusion is not Brownian. Interestingly, the q dependence suggests a ballistic-like motion, but the decay of the correlation function is unusually stretched.

1.2.4.2 Phoretic motion during LLPS

The particles studied in this type of studies are Janus particles, i.e. particles that are composed of regions with different chemical or physical properties. Two regions are present, with different affinities for the two liquid phases. During phase separation, the particles are diffusing to reach the interface, resulting in an directional movement, which has ballistic features [142; 143; 144].

1.2.4.3 Colloidal gel transition and glass transition

XPCS has been extensively used to study colloidal suspensions and their behavior close to the glass and gel transition [145]. The glass transition consists in the transformation from a liquid state to solid disordered state. For a hard sphere suspension the transition can be seen at a volume fraction of $\phi = 0.58$ [146]. This threshold is lowered if the particles are attractive, because they bind with each other and they form a network which increases strongly the rigidity of the sample and hinders the particles movement [147; 140] .

The correlation functions in the liquid states show a single exponential decay, and as the glass/gel transition is approached, a second decay starts to become visible. In fact, its height $f(q)$, called non-ergodicity parameter, increases as the system is closer to the transition. Following a Debey-Waller factor interpretation $f(q) = \exp\left(-\frac{r_{loc}^2 q^2}{6}\right)$, with r_{loc} being the typical movement of the particles, which cannot move outside the cage formed by the neighboring particles. With the mode coupling theory, this localized length can be connected with the rheological properties of the sample [148], namely the elastic shear modulus G', through Eq. 1.13, where R is the radius of the particles.

$$\frac{G'R^3}{k_bT} = \frac{9\phi R^2}{10\pi r_{loc}} \tag{1.13}$$

The second decay is usually compressed with a linear q dependence of the decorrelation rate, which can be seen with XPCS and DLS [149; 150; 151]. This is not only limited to col-

loidal particles, or colloid polymer mixtures [152], but was also observed in metallic glasses, and segregated block copolymer [130; 153; 154]. While a unified understanding of these characteristics has not been found yet, there where attempts to understand the origin of these features with a simple model based on a continuous random walk [150; 130], and others base on strain from stress relaxation [122].

1.2.4.4 Biological samples

Measuring biological samples with XPCS is challenging because of their radiation sensitivity and their low scattering intensity. Recently, the theoretical possibility of performing protein XPCS was demonstrated [155; 156], and the first attempts of measuring biological systems were performed. In this section, we report the studies conducted so far on biological samples with XPCS excluding the studies in Chapters 6 and 8.

The first system studied with XPCS is a highly concentrated α-crystalline solution. It was measured with the goal to understand the behavior of the proteins at very high concentration, close to a glass transition. The samples were probed in SAXS range [157; 158; 159], to access the diffusion of the proteins out of the cage formed by the neighboring proteins. This was combined with NSE to additionally access the short-time diffusion and DLS to probe larger length scales [158]. Another protein investigated is α-Synuclein [160]. With this study it was possible to better understand the role of this protein in the membrane interactions between synaptic vesicles. The diffusion properties of the silica particles coated with a double membrane were measured to see their aggregation state with and without α-Synuclein. The diffusion of the casein micelles was also measured with XPCS [161] to get a better understanding of the process of acidification which is a step necessary to obtain dairy products like yogurt. Cartilage was probed to estimate the interactions between joint fluid and extracellular matrix [162]. The cartilage samples were exposed to different fluids: deionized water, PBS, synovial fluid, or sonicated synovial fluid. The diffusion properties were monitored, showing slower dynamics for more dehydrated samples and the fastest dynamics for synovial fluid. Mucus was investigated to understand its behavior when a modest stress is applied [163]. In the the microscopic dynamics of pig gastric mucus transiently accelerate by up to 2 orders of magnitude, due to the rearrangement dynamics of mucus at the microscopic scale.

The possibility of measuring a wide range of time and length scales gives the flexibility to measure many different system. The variety of the application of this technique shows how promising XPCS is for measuring biological samples.

Part II

Materials and Methods

Chapter 2

Materials and Sample preparation

In this chapter, the sample preparation, the materials, as well as the estimation of the protein concentration are discussed.

2.1 γ-globulin

The protein used for the investigation is an a polyclonal antibody, bovine γ-globulin, also named Ig, (purity $\geq 99\%$, Sigma-Aldrich, G5009), which is composed of different monoclonal antibodies: IgG (80%), IgM (10%) and IgA ($<10\%$) [83]. It is important to note that there are some differences in the proteins powders from different batches. This differences can cause a shift of the phase boundaries of the solutions, but the overall phase behavior remains the same. The concentration of PEG was chosen such that the phase conditions matched with the previous samples.

2.2 Polyethylene glycol

The polymer added to the solution as depletion agent is Poly(ethylene glycol) with a molecular weight of 1kDa (named hereafter "PEG 1000") (Sigma-Aldrich, 81188). The chemical formula of the molecule is $C_{2n}H_{4n+2}O_{n+1}$. Its structure chemical structure is depicted in Fig. 2.1. The number n varies with the molecular weight of the molecule.

This molecule is used for numerous different applications depending on the length of the molecule. It is used in creams and lotion for a Molecular Weight (MW) of 400-700, in toothpastes (MW 600-3350), in lubricants (MW 1450-8000), as a food additive (MW 200-9500), in laxatives (MW 3350-4000), and for cosmetic purposes (MW 3350-4000) [164] .

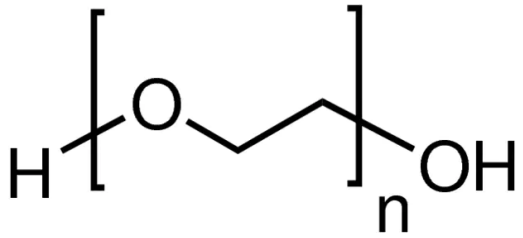

Figure 2.1: The chemical structure of PEG

2.3 Sample preparation

Sample preparation was performed following Refs. [31; 83].

The protein powder was dissolved in a buffer solution composed of H_2O or D_2O with 20 mM HEPES and 2 mM NaN_3 to prevent the growth of bacteria and fungi. The water was degassed before use. The solvent used for all the experiments employing neutron scattering is D_2O, to make use of the largely different cross section of H and D in neutron scattering, thereby increasing the contrast between solvent and protein. The pH was adjusted to a value of 7 by NaOH .

Stock solutions of NaCl (4 M), PEG, and protein were prepared in the buffer solution described previously. Each component was adjusted to the desired final concentration. All the solutions investigated were prepared at 21°C and stored at the same temperature for 1 day to obtain two well separated phases. In case the solution did not have a sharp meniscus the solution was shortly centrifuged. After this procedure the dilute phase was extracted and the dense phase was used to perform the experiments.

The parent solutions of samples used for the investigations reported in this thesis are listed in Table 2.1.

Sample Name	Protein (mg/ml)	PEG (w/v %)	Solvent	Used in
Sample A	200	9%	H_2O	Chapter 6
Sample B	100	6%	D_2O	Chapters 7 and 8
Sample C	200	10%	H_2O	Chapter 8

Table 2.1: Summary of the samples used in the studies reported in this thesis.

2.4 Concentration estimation

The concentration of the Ig stock solutions were determined with a Cary 50 Ultraviolet–Visible Spectroscopy (UV-vis) spectrophotometer, using an extinction coefficient ε =1.4 $mg^{-1}mLcm^{-1}$, a quartz cuvette with a thickness of $d = 1$ cm and the respective absorption values at 280 nm (Eq. 2.1). At this wavelength, the aromatic groups of the amino acids that form the proteins absorb light. Knowing the number of these residues per protein one can calculate the density of proteins in the solution.

$$c_p = \frac{A(\lambda = 280\ \text{nm})}{\varepsilon d} \tag{2.1}$$

The turbidity of a solution can affect the measurement, causing an additional absorbtion at the investigated wavelength. To avoid the turbidity due to the aggregation that is present in a pure Ig solution at low protein concentration [83], a water solution with NaCl was added to obtain a final NaCl concentration of 200 mM.

Chapter 3

Experimental Techniques

In this chapter the experimental methods used for this thesis are described.

The experimental techniques utilized in this work are: Small Angle Scattering, which includes both Small Angle Neutron Scattering (SANS) and Small Angle X-Ray Scattering (SAXS), X-Ray Photon Correlation Spectroscopy (XPCS), Dynamic Light Scattering (DLS), Neutron Spin-Echo (NSE) and Neutron Backscattering (NBS). All these are scattering techniques, and even if the sources and their interaction with matter are different, they share basic principles and some general formalism. For this reason, the first part includes the basics of scattering techniques that are shared by all techniques used. In the second part, small angle scattering is presented, including SAXS, Small Angle Neutron Scattering (SANS). The following section discusses photon correlation spectroscopy. When the source is visible light the technique is called DLS, while for synchrotron radiation and free electron laser it is called XPCS. The last section on the experimental techniques focuses on neutron quasi-elastic scattering, specifically NBS and NSE. The chapter ends with a description of the simulations employed for the rationalization of the results of the Ultra Small Angle X-Ray Scattering (USAXS) XPCS measurements.

The notions of this chapter are based on [32; 165; 166; 167; 168].

3.1 Basics of scattering techniques

A generic scattering measurement consists in the measurement of scattered intensity coming from a beam (X-rays, neutrons, light,...) impinging on a sample (Fig. 3.1).

The incoming beam is generated by a source, which can be a laser, a synchrotron, a nuclear reactor or others. Often before impinging on the sample the beam goes through different

processes to define its characteristics, for example a set of slits to define the size of the beam, a collimator or a monochromator. The beam can then interact with the sample, which is usually contained in capillaries or cuvettes for liquid samples. The intensity is collected by a detector positioned at a specific distance from the sample. For some techniques, it is necessary to have another set of elements to define some characteristics of the scattering intensity, for example a polariser, or a monochromator before the radiation reaches the detector.

The interaction of the incoming beam with the sample is highly dependent on the source, but there are quantities that can be used for neutrons, light as well as for X-rays sources. One of these is the momentum transfer $\vec{q}$. It is defined by the difference between the wavevector of the scattered beam $\vec{k_f}$ and of the incoming beam $\vec{k_i}$ (see inset of Fig. 3.1 and Eq. 3.1). If multiple scattering can be excluded and the scattering process is elastic or quasi-elastic, $\vec{k_f}$ and $\vec{k_i}$ differ only in their direction and not the modulus, hence the absolute value of $\vec{q}$ can be calculated as in Eq. 3.1 with 2θ being the scattering angle (Fig. 3.1) and λ the wavelength of the beam.

$$|\vec{q}| = |\vec{k_f} - \vec{k_i}| = \frac{4\pi}{\lambda}\sin(\theta) \tag{3.1}$$

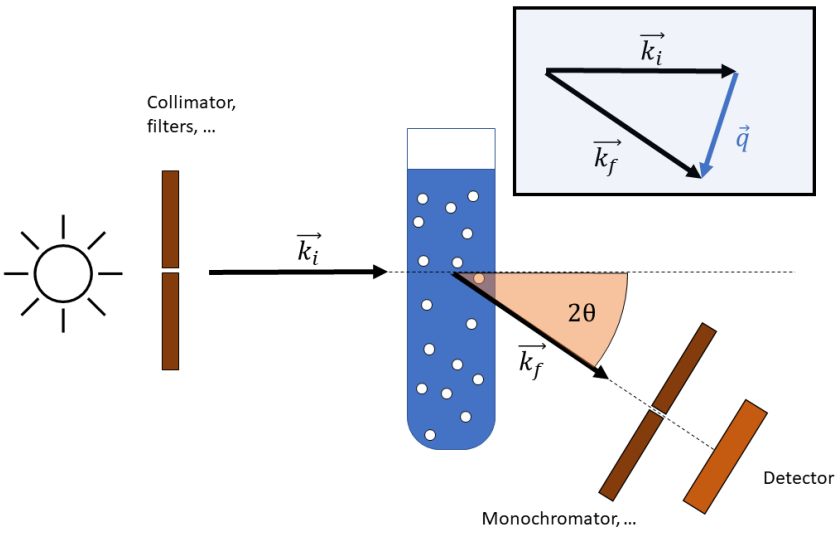

Figure 3.1: Sketch of a generic scattering setup. With the scattering vector $\vec{q}$, incoming $\vec{k_i}$ and outcoming $\vec{k_f}$ wavevector. The angle between $\vec{k_i}$ and $\vec{k_f}$ is defined as 2θ, and $\vec{q}$ is obtain by subtracting $\vec{k_i}$ from $\vec{k_f}$.

Given a volume V containing N particles with scattering length b_i, the density of scattering length is given by the sum of the density of scattered length of each particle, i.e. $\rho(r) = \sum_p b_p \rho_p(\vec{r})$, where $\rho_p(\vec{r})$ is the density of a single particle.

The local scattered amplitude is then given by

$$A(\vec{q}) = \int_V \rho(\vec{r}) e^{-i\vec{q}\vec{r}} d\vec{r}. \tag{3.2}$$

To calculate the intensity of a beam scattered by a system of N spherical particles, the assumption that there is no multiple scattering will be used. This assumption is almost always satisfied for X-ray and neutron scattering, but for light scattering it holds only for diluted solutions. The scattering intensity can then be expressed as

$$I(\vec{q}) = \frac{A(\vec{q})A^*(\vec{q})}{V} = \frac{1}{V}\int_V \int_V \rho(\vec{r}) e^{-i\vec{q}\vec{r}(t)} \rho(\vec{r}') e^{i\vec{q}\vec{r}'(t)} d\vec{r} d\vec{r}'. \tag{3.3}$$

Introducing the substitution $\vec{r} = \vec{r}_i + \vec{u}$ with $\vec{r}_i$ being the position of the i-th particle, the intensity can be written as:

$$I(\vec{q}) = \tfrac{1}{V} \sum_{i=1}^{N} e^{-i\vec{q}\vec{r}_i(t)} \int\limits_{V_{\text{par}}} \rho_i(\vec{u}) e^{-i\vec{q}\vec{u}} d\vec{u} \sum_{j=1}^{N} e^{i\vec{q}\vec{r}_j(t)} \int\limits_{V_{\text{par}}} \rho_j(\vec{v}) e^{i\vec{q}\vec{v}} d\vec{v}$$

Using $f_j(\vec{q}) = \int\limits_{V_{\text{par}}} \rho_j(\vec{v}) e^{-i\vec{q}\vec{v}} d\vec{v}$, the expression can be written as

$$I(\vec{q},t) = \frac{1}{V} \sum_{j=1}^{N} \sum_{i=1}^{N} e^{-i\vec{q}\vec{r}_i(t)} e^{i\vec{q}\vec{r}_j(t)} f_i(\vec{q}) f_j^*(\vec{q}). \tag{3.4}$$

This is the case only for spherical particles, otherwise the terms $f_i(\vec{q})$ have to include also a factor that takes into account the orientation of each particle. If we introduce the assumption that the system is monodispersed, meaning that all the particles are identical, then $f_1(\vec{q}) = f_2(\vec{q}) = ...f_N(\vec{q}) = f(\vec{q})$, and the previous equation can be rewritten as

$$I(\vec{q},t) = |f(\vec{q})|^2 \frac{1}{V} \sum_{j=1}^{N} \sum_{i=1}^{N} e^{-i\vec{q}\vec{r}_i(t)} e^{i\vec{q}\vec{r}_j(t)}. \tag{3.5}$$

This expression has a term that contains the shape of the particles $|f(\vec{q})|^2$, also called form factor, and a part that depends on the position of the individual scatterers $\sum_{j=1}^{N} \sum_{i=1}^{N} e^{-i\vec{q}\vec{r}_i(t)} e^{i\vec{q}\vec{r}_j(t)}$. The latter part will be important to obtain information about the diffusion of particles.

3.1.1 Van Hove function

The Van Hove function [169] is a useful tool to get more quantitative insight on the diffusion and structural properties of a solution in isotropic samples. It is defined as the probability of finding a particle at distance $\vec{r}$ and after a time t with respect to an initial particle. In a system with N particles the corresponding mathematical expression is

$$G(\vec{r},t) = \frac{1}{N}\langle\sum_{i=1}^{N}\sum_{j=1}^{N}\delta(\vec{r}+\vec{r}_i(0)-\vec{r}_j(t))\rangle, \tag{3.6}$$

where the brackets $< \cdot >$ are an average over the possible configurations in the system. The function $G(\vec{r},t=0)$ is the average spatial arrangement of the particles in a system. It is informative, for example, to see the presence or lack of crystal structure, the average inter-particle distance and, in general, it is linked to the pair interaction potential of two particles. If the time t is not fixed to 0, the function $G(\vec{r},t)$ describes how the arrangement of the particles changes in time and can be divided in two parts: the self part, meaning the probability of finding the same particle at distance $\vec{r}$ after a time t, or the distinct part, i.e. the probability of finding any particle that is not the one considered at distance $\vec{r}$ after a time t. The previous equation can be divided in

$$\begin{aligned} G(\vec{r},t) &= \frac{1}{N}\langle\sum_{i=1}^{N}\delta(\vec{r}+\vec{r}_i(0)-\vec{r}_i(t))\rangle + \frac{1}{N}\langle\sum_{i=1}^{N}\sum_{j=1}^{N}\delta(\vec{r}+\vec{r}_i(0)-\vec{r}_j(t))\rangle = \\ &= G_s(\vec{r},t) + G_d(\vec{r},t). \end{aligned} \tag{3.7}$$

Many scattering techniques employed in this thesis cannot obtain directly Van Hove function, but either its spatial and temporal Fourier transform the structure factor $S(q,\omega)$, defined as

$$\begin{aligned} S(q,\omega) &= \int G(\vec{r},t)\exp(i(\vec{q}\vec{r}-\omega t))d\vec{r}dt = \\ &= \int (G_s(\vec{r},t)+G_d(\vec{r},t))\exp(i(\vec{q}\vec{r}-\omega t))d\vec{r}dt = \\ &= S_{\text{self}}(q,\omega) + S_{\text{collective}}(q,\omega). \end{aligned} \tag{3.8}$$

Another quantity often used is its spatial Fourier transform, the intermediate scattering function ISF (also called $g_1(q,t)$), which can be written as

$$\begin{aligned} \mathrm{ISF}(q,t) &= \int G(\vec{r},t)\exp(i(\vec{q}\vec{r}))d\vec{r} = \\ &= \int \frac{1}{N}\langle\sum_{i=1}^{N}\sum_{j=1}^{N}\delta(\vec{r}+\vec{r}_i(0)-\vec{r}_j(t))\rangle\exp(i(\vec{q}\vec{r}))d\vec{r} = \\ &= \frac{1}{N}\langle\sum_{i=1}^{N}\sum_{j=1}^{N}\exp(i(\vec{q}(\vec{r}_i(0)-\vec{r}_j(t))))\rangle. \end{aligned} \tag{3.9}$$

The Fourier transform of the single terms $G_s(\vec{r},t)$ and $G_d(\vec{r},t)$ are defined as a self part $S_{\mathrm{self}}(q,\omega)$ and a distinct (also called collective) part $S_{\mathrm{collective}}(q,\omega)$ of the structure factor.

The two parts of the structure factor permit the monitoring of the self diffusion and the collective diffusion. The self-diffusion addresses the question how a single particle moves while interacting with its surrounding of particles. With the collective diffusion it is possible to access the movement of many particles simultaneously. This at first glance subtle difference, can be appreciated more though a practical example: the self diffusion is observed by looking at the movement of a single particle in a microscope, the effects of collective diffusion on the other hand can be seen when adding a droplet of ink in water solution, the spread of the ink in this case is given by a multitude of particles which diffuse collectively.

3.1.2 From correlation functions to diffusion

It is intuitive that the time dependent spatial distribution of the particle $G(\vec{r},t)$ is strictly connected to the diffusion properties of the particle. To have a more quantitative description, it is necessary to see how the Van Hove function can be obtained for certain types of diffusion. In this section, different types of motion are presented and the corresponding Van Hove function or structure factor is calculated, starting with Fickian diffusion also called Brownian motion, to then treat the more general anomalous diffusion.

3.1.2.1 Brownian motion

Given a system with N particles, the density of particles in the system can be written as $\rho(\vec{r},t) = \sum_{n=1}^{N}\delta(\vec{r}-\vec{r}_n(t))$. It is known since Brown observed the movement of pollen particles with a microscope [170] that each particle is not immobile, but performs a motion that is called Brownian motion. In the limit of high dilution, where the particles are not interacting with each other, their diffusion can be described by the diffusion equation [171]

$$\frac{\partial \rho(\vec{r},t)}{\partial t} = D\nabla^2 \rho(\vec{r},t), \tag{3.10}$$

where the diffusion coefficient D depends on the temperature T, the viscosity of the solution η and the hydrodynamic radius of the particles R_h following the so called Stokes-Einstein relation (Eq. 3.11).

$$D = \frac{k_b T}{6\pi\eta R_h}. \tag{3.11}$$

The function $G(\vec{r},t)$ also has to satisfy the same equation [172], hence

$$\frac{\partial G(\vec{r},t)}{\partial t} = D\nabla^2 G(\vec{r},t). \tag{3.12}$$

This equation can be simplified by solving its Fourier transform, which becomes

$$\frac{\partial \mathrm{ISF}(\vec{q},t)}{\partial t} = -Dq^2 \mathrm{ISF}(\vec{q},t). \tag{3.13}$$

A solution of this simplified equation is then $\mathrm{ISF}(t,q) = \exp(-Dq^2 t)$, which implies that

$$G(r,t) = \sqrt{(4\pi Dt)^d}\exp(-\frac{r^2}{4Dt}), \tag{3.14}$$

where d is the dimensionality of the system.

Since in the considered case the particles are not interacting with each other $G(r,t) = G_s(r,t)$, hence from the Van Hove function it is possible to calculate directly the mean squared displacement $\langle \Delta R(t) \rangle^2$ via

$$\langle \Delta R(t) \rangle^2 = \int r^2 G_s(r,t) dr = 2dDt \tag{3.15}$$

The proportionality $\langle \Delta R(t) \rangle^2 \propto t$ is a distinctive trait of Brownian motion. This type of diffusion is ubiquitous in nature, thus it is also referred as simple diffusion, in contrast to the anomalous diffusion, where the transport properties are such that $\langle \Delta R(t) \rangle^2 \propto t^\alpha$ with $\alpha \neq 1$.

3.1.2.2 Anomalous diffusion

In biological systems, the diffusion processes are very complex, even without the presence of biological pumps the high concentration and polydispersity do not permit simple diffusion, but cause an anomalous one [173; 174].

Different anomalous diffusion types are classified in two categories based on their transport properties, which are estimated through the mean squared displacement. As already mentioned in the previous section anomalous diffusion does not follow $\langle \Delta R(t) \rangle^2 \propto t$. To have an expression for $\langle \Delta R(t) \rangle^2$ that includes anomalous diffusion, it is necessary to use a generalised expression [175], where the diffusion coefficient D_α has units that depend on the value of α

$$\langle \delta R \rangle^2 = 2dD_\alpha t^\alpha. \tag{3.16}$$

With this equation we can now define the two aforementioned categories: the first one is composed by the diffusion phenomena for which $0 < \alpha < 1$ and are therefore called subdiffusive, since the mean squared displacement grows faster in time than for Brownian motion. The others, where $\alpha > 1$, are called hyperdiffusive or superdiffusive, since the mean squared displacement is increasing faster in time than it would for Brownian motion. This differentiation does not imply that hyperdiffusion is a fast motion, or that particles that are hyperdiffusive are faster than subdiffusive particles, since this depends on the diffusion coefficient D_α, but only on the different time dependence of the mean square displacement. For example hyperdiffusion is a typical feature of glass or gel dynamics [150], with decorrelation times in the orders of 100 s, but also the diffusion of an ideal gas is hyperdiffusive and its relaxation times are many orders of magnitude smaller.

With the following simple model it is possible to describe a variety of diffusion phenomena in a general manner to be able to compare the different type of diffusion and was used to explain a variety of systems such as glassy colloidal solutions [122], gel of hen egg white [136], supercooled liquids [176] in the liquid as well as in the glass state.

The diffusion of the particles is discretize in single events, which cause a loss of correlation. The probability of N events $P_t(N)$ to happen is given by a Poisson distribution with a mean value given by $\Gamma_0 t$ (continuous random walk), so that one event is happening with a rate of Γ_0, hence

$$P_t(N) = \frac{\exp(-\Gamma_0 t)}{N!}(\Gamma_0 t)^N. \tag{3.17}$$

The amount of correlation lost in N events $h(q,N)$ can be calculated via

$$h(q,N) = \exp\left[q^2(N^{\frac{\alpha}{2}}\delta^2)\right], \tag{3.18}$$

with δ being the mean displacement due to one event and α is the constant defined at the

beginning of the section.

To understand the reason of this, one has to calculate the mean squared displacement of this quantity. To do so, it is first necessary to calculate the Van Hove function from the ISF. The intermediate scattering function is

$$\mathrm{ISF}(q,t) = \sum_{N=0}^{\infty} P_t(N)h(q,N) = \sum_{N=0}^{\infty} \frac{\exp(-\Gamma_0 t)}{N!}(\Gamma_0 t)^N \exp(-(qN^{\frac{\alpha}{2}}\delta)^2) \tag{3.19}$$

and its Fourier transform is given by

$$\begin{aligned} G(r,t) &= \sum_{N=0}^{\infty} \frac{\exp(-\Gamma_0 t)}{N!}(\Gamma_0 t)^N \int dq \exp(iqr) \exp[q^2(N^{\frac{\alpha}{2}}\delta)^2] = \\ &= \sum_{N=0}^{\infty} \frac{\exp(-\Gamma_0 t)}{N!}(\Gamma_0 t)^N \frac{\pi}{N^{\frac{\alpha}{2}}\delta} exp(-\frac{r^2}{(N^{\frac{\alpha}{2}}\delta)^2}). \end{aligned} \tag{3.20}$$

Therefore, the mean squared displacement is

$$\begin{aligned} \langle \Delta R(t) \rangle^2 &= \int r^2 G(r,t) dr = \\ &= \sum_{N=0}^{\infty} \frac{\exp(-\Gamma_0 t)}{N!}(\Gamma_0 t)^N \frac{\pi}{N^{\frac{\alpha}{2}}} \int r^2 exp(-\frac{r^2}{(N^{\frac{\alpha}{2}})^2}) = \\ &= \sum_{N=0}^{\infty} \frac{\exp(-\Gamma_0 t)}{N!}(\Gamma_0 t)^N (N^{\frac{\alpha}{2}}\delta)^2. \end{aligned} \tag{3.21}$$

Considering that the diffusion of the particles is composed of many of these events we can consider that we are in the regime where $\Gamma_0 t \gg 1$. In this approximation $\langle \Delta R(t) \rangle^2 \propto \delta^2 t^\alpha$ is valid.

3.2 Small Angle Scattering

Small angle scattering is a technique extensively used to investigate the structure of liquid samples, as well as crystals, powders or gels on the length scale between $\mathring{A}$ and μm.

The source of radiation and the sample-detector distance distinguish different techniques that belong to the category of small angle scattering. For X-rays, the small angle scattering is often divided into two categories: SAXS for $q > 0.1\,\mathrm{nm}^{-1}$ and USAXS for $0.1\,\mathrm{nm}^{-1} < q < 1\ \mu\mathrm{m}^{-1}$. The equivalent is present also for neutron scattering, in this case they are called

SANS and Very Small Angle Neutron Scattering (VSANS). Using light as a source one can collect data withStatic Light Scattering (SLS). The different beams have different interactions with the atoms composing the sample. While photons interact with the electrons via electromagnetic interactions, neutrons interact with the nuclei of the atoms via the strong interaction. Thus, different types of beams can show different properties of matter. The combination of this and the difference in the production of the radiation itself provide each technique with specific advantages and disadvantages. For example, with X-rays a high time resolution can be achieved, but the measurement time is limited by radiation damage. Neutron scattering on the contrary has a much lower time resolution due to the lower achievable flux, but the sample is not subjected to any radiation damage. Light scattering is not affected by radiation damage and has a very good time resolution, but it cannot be employed for turbid samples because of the multiple scattering.

These techniques can be used in a complementary manner, for example taking advantage of the different scattering length densities for neutron and X-ray scattering [177], and having, therefore, different contrast for different parts of the molecules.

To understand the information that can be obtained by small angle scattering we have to start from Eq. 3.4. The intensity in this equation is describing one of the possible configuration of the system, and depends on the single position of each particles, but it is in principle not possible to know if this is representative for the system and not a very rare occurrence. To ensure that this is not true in the ideal case the intensity that is collected has to be:

$$I(\vec{q},t) = \frac{1}{V}\left\langle \sum_{j=1}^{N}\sum_{i=1}^{N} e^{-i\vec{q}\vec{r}_i(t)} e^{i\vec{q}\vec{r}_j(t)} f_i(\vec{q}) f_j^*(\vec{q}) \right\rangle, \tag{3.22}$$

where the brackets $\langle\cdot\rangle$ are an average over the possible configurations of the system. To obtain a similar average in the system there are different possible approaches: The first one is to have a very large number of particles, hence $N \to \infty$, because if the particles have a random configuration for an infinite number of particles all the possible configurations will be probed. The second possibility is to measure the system for a time that is much larger than the typical time of movement of the particles. In this way the particles are moving from one configuration to another many times, which provides an average over the different configurations.

A detailed description of the generic case is beyond the scope of this section, so we will limit the treatment under the assumption that the system is mono-dispersed, meaning that all the particles are of the same type, and for spherical particles then $f_1(\vec{q}) = f_2(\vec{q}) = ... = f_N(\vec{q}) = f(\vec{q})$.

The previous equation can be rewritten [165] as

$$I(\vec{q},t) = |f(\vec{q})|^2 \frac{1}{V} \Big\langle \sum_{j=1}^{N} \sum_{i=1}^{N} e^{-i\vec{q}\vec{r}_i(t)} e^{i\vec{q}\vec{r}_j(t)} \Big\rangle. \tag{3.23}$$

This equation can be rewritten by introducing the quantities of a) form factor

$$P(q) = \frac{1}{(\Delta\rho)^2} |f(\vec{q})|^2, \tag{3.24}$$

where $\Delta\rho$ is the difference of scattering length density of the particles and the solvent, and b) static structure factor

$$\bar{S}(q) = \frac{1}{N} \Big\langle \sum_{i=1}^{N} e^{-i\vec{q}(\vec{r}_i(t) - \vec{r}_j(t))} \Big\rangle. \tag{3.25}$$

The normalisation factors $\frac{1}{(\Delta\rho)^2}$ and $\frac{1}{N}$ are present to fulfill the requirement $\bar{S}(q \to \infty) = 1$ and $P(q \to 0) = 1$. The expression can be then rewritten [165] into

$$I(q) = \frac{N}{V} (\Delta\rho)^2 \bar{S}(q) P(q). \tag{3.26}$$

This equation can be generalised to a system of non-spherical particles by substituting $\bar{S}(q)$ with $\bar{S}_{eff}(q)$, which is a term that contains not only $\bar{S}(q)$ but also a factor that takes into account the non-isotropic shape of the particles. This is because, for non spherical particles, the average affects also $f(\vec{q})$, since this quantity is now dependent on the different orientation of the particles. In this case $P(q) = \frac{1}{(\Delta\rho)^2} \langle |f(\vec{q})|^2 \rangle$

The form factor $P(q)$ depends only on the shape of the particles and not on their position in the scattering volume V. The static structure factor $\bar{S}(q)$ is instead a quantity that describes the average arrangement of the particles in the solution. This quantity is strictly connected to the structure factor seen in Section 3.1.1, since $\bar{S}(q) = \int S(q,\omega) d\omega$.

3.3 Photon Correlation Spectroscopy

In this section, the basic principles of Photon Correlation Spectroscopy (PCS) are discussed for both, light and X-ray scattering. In the first part, the intensity auto-correlation functions are introduced, as well as how to obtain them from the experimental data. This knowledge is later used to understand the connection of this quantity with the van Hove function. The second part is dedicated to the two-time correlation function and its difference with the intensity

auto-correlation function. The following part focuses on partial coherence, a concept which is relevant for XPCS. The forth part addresses the issues that are present when measuring proteins and biological matter with XPCS, and possible techniques to avoid beam damage on the sample. The remaining parts cover the experimental setup of the experiments presented in the thesis. For the general background, the reader is referred to Refs. [129; 178; 179; 180].

3.3.1 Van Hove function via intensity auto-correlation function

The intensity auto-correlation function is the quantity that is obtain by measuring with PCS, whether the technique is XPCS or DLS.

With a single pixel detector this quantity is calculated with

$$g_2(\vec{q},t) = \frac{< I(\vec{q},0)I(\vec{q},t) >}{< I(\vec{q},0) >^2}. \tag{3.27}$$

To perform this average, the system has to be monitored in different configurations. For a system in equilibrium, the average can be substituted by a time average, and the functional form is

$$g_2(\vec{q},t) = \frac{\sum_{k=1}^{N-\frac{t}{\Delta t}} I(\vec{q},k\Delta t)I(\vec{q},t+k\Delta t)}{[\sum_{k=1}^{N} I(\vec{q},k\Delta t)]^2}, \tag{3.28}$$

where Δt is the time between two consecutive acquisitions, which is the sum of the exposure time of one exposure and the waiting time before the successive exposure . The total measurement time is then given by $N\Delta t$. The value of $\vec{q}$ depends on the position of the detector as indicated in Eq. 3.1. The intensity $I(\vec{q},t)$ ideally is the scattering intensity of only one configuration of the system (it depends on the value of Δt and the typical time of the system) and, as such, it is time dependent if the particles composing the sample are not immobile.

With a 2D detector more pixels can be monitored at the same time. If the system it is isotropic (both the structure and the diffusion properties), $g_2(\vec{q},t)$ can be rewritten as $g_2(q,t)$ and thus, it is possible to average $g_2(q,t)$ of different pixels which correspond to the same q

value. For this reason the autocorrelation function can be calculated to

$$g_2(q,t) = \frac{\langle\langle I(\vec{q},0)I(\vec{q},t)\rangle_t\rangle_q}{\langle\langle I(\vec{q},0)\rangle_t\rangle_q^2} = \frac{\sum\limits_{i\in\mathcal{A}_q}\sum\limits_{k=1}^{N-\frac{t}{\Delta t}} I(q_i,k\Delta t)I(q_i,t+k\Delta t)}{[\sum\limits_{i\in\mathcal{A}_q}\sum\limits_{k=1}^{N} I(q_i,k\Delta t)]^2}, \tag{3.29}$$

where $\mathcal{A}_q$ is the set of all pixels which correspond to a specific q value.

The intensity correlation function can be directly connected to the intermediate scattering function ISF or $g_1(q,t)$ via the Siegert relation, which states

$$g_2(q,t) = 1 + \beta|\mathrm{ISF}(q,t)|^2. \tag{3.30}$$

The function $g_1(q,t)$ is also called the electric field auto-correlation function because for coherent sources it can be written as

$$g_1(\vec{q},t) = \frac{< E(\vec{q},0)E(\vec{q},t) >}{< E(\vec{q},0)^2 >}. \tag{3.31}$$

The parameter β is given by the experimental setup and is related to the coherence of the source. Hence, it has a conceptual difference for DLS and XPCS, namely for the first one the light is always almost fully coherent, but in latter one the source is only partially coherent, which reduces the value of β considerably, so that setup parameter have to be carefully optimize to perform the experiment.

To proof the validity of the Siegert relation, one can insert the value of the intensity calculated in Eq. 3.23 in Eq. 3.27. The numerator is given by

$$\begin{aligned} < I(t)I(0) > &= |f(q)|^4 < \sum_{i,j,n,m=1}^{N} \exp(-i\vec{q}\cdot(\vec{r}_i(t) - \vec{r}_j(t) + \vec{r}_m(0) - \vec{r}_n(0))) > \\ &= |f(q)|^4 N^2 (1 + |g_1(t,q)|^2), \end{aligned} \tag{3.32}$$

while the denominator is simply given by $< I(t) >^2 = |f(q)|^4 N^2$.

3.3.2 Two-time correlation function

If the system that is measured is not in equilibrium, because, for example, it is undergoing phase separation, like for the system investigated in this thesis, or in general it is aging (meaning that the dynamics change with time), it is not possible to get a reliable $g_2(\vec{q},t)$ with the same approach used in Section 3.3.1, because it would result in an effective average over different $g_2(\vec{q},t)$ which correspond to different physical states.

This can be avoided by using the so called two-time correlation function (TTC). It is a 2D correlation map, which gives the correlation of the intensity measured at time t_1 and the intensity at time t_2. There are different definitions of this quantity [181], in the first one

$$g_2(\vec{q},t_1,t_2) = \frac{\langle I(t_1)I(t_2)\rangle_q}{\langle I(t_1)\rangle_q \langle I(t_2)\rangle_q}, \tag{3.33}$$

while for the second one

$$g_2(q,t_1,t_2) = \frac{\langle [I(t_1)-\bar{I}(t_1)][I(t_2)-\bar{I}(t_2)]\rangle}{\sqrt{[\bar{I^2}(t_1)-\bar{I}^2(t_1)][\bar{I^2}(t_2)-\bar{I}^2(t_2)]}}) \tag{3.34}$$

where $\bar{I}(t_1) = \langle I(t_1)\rangle_q$ is the average intensity at time t_1. This is obtained by averaging over all the N_a pixels on the detector in an area $\mathcal{A}_q$, so that $\langle I\rangle_q = \frac{1}{N_a}\sum_{i\in\mathcal{A}_q} I_i$. The area $\mathcal{A}_q$ has to contain a number of pixels that is large enough to ensure the correctness of the average, and cover a range of q values Δq in which the intensity is almost constant. The difference between the two quantities is that in Eq. 3.33 the correlation of the intensity is normalised by the average intensity, while in the Eq. 3.34 it is normalised with the standard deviation. In some cases, these two expressions are equivalent, but, for systems in which the intensity is changing, it is advisable to use Eq. 3.34 [181].

3.3.3 Partial coherence and contrast

The beam has to fulfill some coherence requirement to collect reliable a $g_1(t,q)$. This is evident looking at the definition:

$$g_1(q,t) = \frac{< E(\vec{q},0)E(\vec{q},t) >}{< E^2(\vec{q},0) >} \tag{3.35}$$

from Eq. 3.31. If the beam can be described as an incoherent plane wave $E(q,t) = E_0 e^{i(\vec{q}\cdot\vec{r}-\omega t+\psi)}$ with a random time dependent term $\psi(t)$, then $g_1(q,t) \propto g_1^{\text{sample}}(q,t)\langle e^{i\Delta\psi}\rangle$ with $g_1^{\text{sample}}(q,t)$ being the correlation function that would be obtained with fully coherent beam. Since $\Delta\psi$ is a difference between the two phases, hence a constant, we obtain $\langle e^{i\Delta\psi}\rangle = 0$. This means that $g_1(q,t)$ will always be 0.

It is not possible with the current synchrotron and X-ray free electron laser technology advancement to achieve fully coherent beams, but partial coherence is sufficient to obtain reliable correlation functions. Partial coherence means that the beam is not coherent over the whole scattering volume, but this volume can be subdivided in smaller volumes, called coherence volumes, in which the beam can be considered coherent.

The probability distribution $P(I)$ of the intensity for a fully coherent beam[178; 182; 183] is an exponential distribution

$$P(I) = \frac{1}{\langle I\rangle}\exp\left(-\frac{I}{\langle I\rangle}\right). \tag{3.36}$$

The mean intensity is $\langle I\rangle$ and the standard deviation σ of the intensity is equivalent, i.e. $\sigma = \sqrt{\langle I^2\rangle - \langle I\rangle^2} = \langle I\rangle$. The contrast β (the same constant as in Eq. 8.4) is defined as the ratio $\beta = \frac{\sigma^2}{\langle I\rangle^2} = 1$ [178; 182].

For a partially coherent source the probability distribution is different, and follows

$$P(I) = M^M \left(\frac{I}{\langle I\rangle}\right)^{M-1} \frac{\exp\left(-\frac{MI}{\langle I\rangle}\right)}{\Gamma(M)\langle I\rangle}, \tag{3.37}$$

where $\Gamma(x)$ is the gamma function, and M is the number of coherence volumes in the sample. The mean intensity is again $\langle I\rangle$, but the standard deviation changes, and is in this case $\sigma = \frac{\langle I\rangle}{\sqrt{M}}$. This has consequences on the value of $\beta = \frac{\sigma^2}{\langle I\rangle^2} = \frac{1}{M}$. Therefore, a partially coherent source inversely dependent on the number of coherence volumes. If the number of M is very large, β approaches the value 0, and the beam can be considered incoherent. A fraction α of the photons composing the beam participate in the coherence interference, which reduces the coherence to $\beta = \frac{\alpha^2}{M}$.

The size of the coherence volume is the space within which the photons are coherent. There are two terms that contribute to the coherence volume: the longitudinal coherence and the transverse coherence.

3.3.3.1 Longitudinal coherence

The loss of longitudinal coherence is due to the finite bandwidth of the beam, in fact $\Delta\lambda$ can vary depending on the monochromator used, for example for a Si(111) monochromator $\Delta\lambda/\lambda \simeq 1.4 \times 10^{-4}$, while for a Si(311) it is $\Delta\lambda/\lambda \simeq 3 \times 10^{-5}$ [155].

If we consider two plane waves with a shift $\Delta\lambda$ in the wavelength as represented in Fig. 3.2, they are completely out of phase after a length $\frac{\lambda^2}{\Delta\lambda}$. The longitudinal coherence ξ_l defined as half of this distance, hence $\xi_l = \frac{\lambda^2}{2\Delta\lambda}$

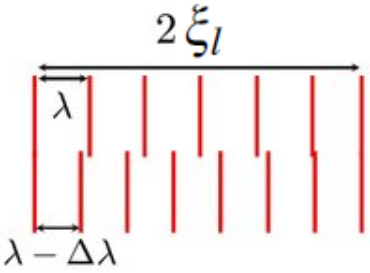

Figure 3.2: Sketch of two plane waves with a phase shift of $\Delta\lambda$, and the definition of ξ_l.

3.3.3.2 Transverse coherence

The loss of transverse coherence is due to the non-finite size of the source. If the size of the source is L_s, and the distance between the source and the sample is R as represented in Fig. 3.3, then two waves generated at maximum distance L_s on the source will be completely out of phase at a distance $\frac{R\lambda}{L_s}$. The transversal coherence is defined as half of this distance, hence $\xi_t = \frac{R\lambda}{2L_s}$. Since the sources are usually not equal in size in the vertical and horizontal direction, the vertical transverse coherence ξ_t^v and the horizontal transverse coherence ξ_t^h can be different. In a synchrotron, because of the way the X-rays are produced, the vertical coherence is much smaller than the horizontal one. For this reason only the latter is considered for the calculation of the contrast. For the beamline P10 the distance between source and sample is $R = 90\,\text{m}$, and the source size in the horizontal direction is $L_s = 36\,\mu\text{m}$, which results in an horizontal coherence length of $\xi_t^h = 50\,\mu\text{m}$ for a beam energy of 10 keV.

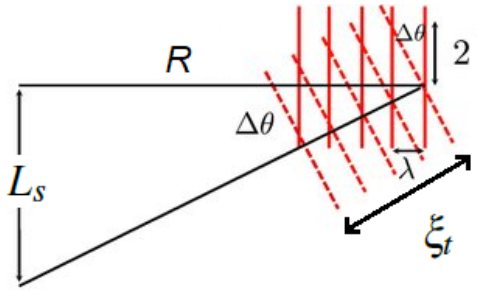

Figure 3.3: Sketch of two plane waves produced at two points on the source at distance R , and the definition of ξ_t.

3.3.4 Challenges of measuring proteins with XPCS and considerations on beam effects

The diffusion of proteins is often studied with scattering techniques, such as DLS, NSE and NBS, but until recently it was not possible to employ XPCS because of the limited coherence of the sources, the relative small difference between the scattering length density of water and the proteins, which imply a small scattering signal, and the sensitivity of biological material to radiation damage.

The development of new X-rays sources in the last decades increased the brilliance and achievable coherence (Fig. 3.4)[184]. With these improvements the beam intensity and coherence are large enough to perform the experiments, but can lead to beam damage due to the high flux of photons on the sample [185]. Nevertheless the experimental parameters can theoretically be optimized in order to be able to probe biological samples, such as protein solutions, and prevent beam damage [155; 156]. The signal to noise ratio (SNR) of the intensity correlation function can be estimated with [186]

$$\mathrm{SNR} = \beta I_{pix} \sqrt{N_{fr} N_{pix} N_{rep}}, \tag{3.38}$$

where I_{pix} the average intensity per pixel, N_{pix} the number of pixel, N_{fr} the number of images collected in a series, and N_{rep} is the number of times that a series was collected. These parameters are often connected with each other and cannot always be adjusted freely, except for N_{rep}, which in principle can be increased at will, but in practise will be determined by the amount of samples at disposal and the instrument time availability. While β and N_{pix} are determined by the experimental setup, the values of I_{pix}, which is directly proportional to the beam flux, and N_{fr} are mainly limited by radiation damage. To understand the conditions on

these parameters, the dose of radiation on the sample has to be estimated:

$$\mathcal{D} = \frac{FN_{fr}t_{exp}(1-T_{\text{sample}})}{ad\rho} \tag{3.39}$$

With F being the flux of the beam (photons/s), t_{exp} the exposure time, T_{sample} the sample transmission, a the beam area, d the thickness of the sample and ρ the density of the sample. If we assume a maximum dose $\mathcal{D}_c$ that the sample can be exposed to without any radiation damage, the maximum number of frames becomes $N_{fr} = \frac{\mathcal{D}_c ad\rho}{Ft_{exp}(1-T_{sample})}$. This implies that SNR $\propto \sqrt{F}$, so in principle the flux can be increased to have the maximum SNR, but of course there are limitation since the number of frames has to be larger than 1. Another factor that one has to take into account is the dependency on the detector. This is clear for N_{pix} and β, but also N_{fr} is affected by it, since the detector time resolution sets the minimum exposure time of a frame and the noise intensity threshold.

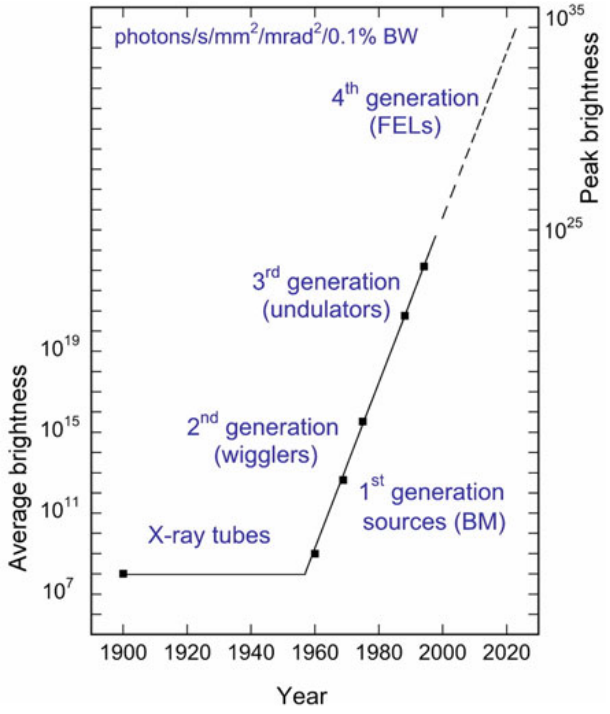

Figure 3.4: The evolution of the brightness of sources with years from the X-ray tubes to the brightest sources now present, which is the free electron lasers. Figure from Ref. [184].

The difference between XPCS performed in USAXS (0.001 nm^{-1} $< q <$0.05 nm^{-1}) and SAXS ranges (0.05 nm^{-1} $< q <$1 nm^{-1}) can seem subtle, but when considering the depen-

dence of the SNR on q it becomes clear that the experiment in SAXS range is much more challenging. This is because both, the contrast and the intensity per pixel, decreases fast with q (Fig. 3.5)). The intensity for systems that undergo phase separation is decreasing fast, since usually $I \propto q^{-4}$. The system investigated in this thesis has a difference in intensity in the order of 10^4 between USAXS and SAXS (Fig. 3.5a). To reduce this effect, the sample-detector distance $R_{\text{sample}-\text{detector}}$ can be reduced, since the scattered field can be considered in first approximation as a spherical wave $I(q) \propto 1/R^2_{\text{sample}-\text{detector}}$. However, if $R_{\text{sample}-\text{detector}}$ is reduced, the contrast is also reduced (Fig. 3.5b). To increase it, an usual choice is to reduced the beam size (Fig. 3.5c). This has the consequence that, if F is kept constant, the density of photons per second on the sample is much higher. Hence, in general the beam effects are much higher in SAXS range.

Different strategies have been used to decrease the effect of beam on the samples. For example, to increase the contrast between the solvent and the proteins (meaning increasing I_{pix} without changing the incoming flux), a label can be added to the proteins, following a sample preparation similar to the one performed for fluorescence spectroscopy, or some inorganic particle can be added to the sample [160]. Although this solves the initial problem since it increases the scattering intensity, it also introduces a new issue, namely how is the biological system influenced by the presence of the label? Another possibility to avoid radiation damage is to move the sample while measuring, hence exposing the sample for shorter time. This approach was successfully used to measure the diffusion of bovine alpha crystalline by translating the sample vertically and subsequently correcting for this movement in the data analysis [157]. With this approach, the dose on the sample was reduce to $\sim$0.9 kGy. Much lower values (0.045 kGy) have been achieved at lower q ranges [161] by performing low dose X-ray speckle visibility spectroscopy measurements, where single frames are collected instead of series of images [131].

3.3.5 Experimental setup for Dynamic Light Scattering

An ALV/CGS-3 (ALV-GmbH, 63225 Langen, Germany) was used to collect DLS datasets (Fig.3.6), with a HeNe-Laser as a source with wavelength $\lambda = 632.8$ nm. The light produced by the laser is attenuated and directed to the toluene bath, which contains the sample. The detector can move from an angle of 12° to and angle of 152°, so that the scattering intensity can be measured at different q vectors. Quartz cuvettes with a diameter of 5 mm were immerse in a temperature controlled toluene bath.

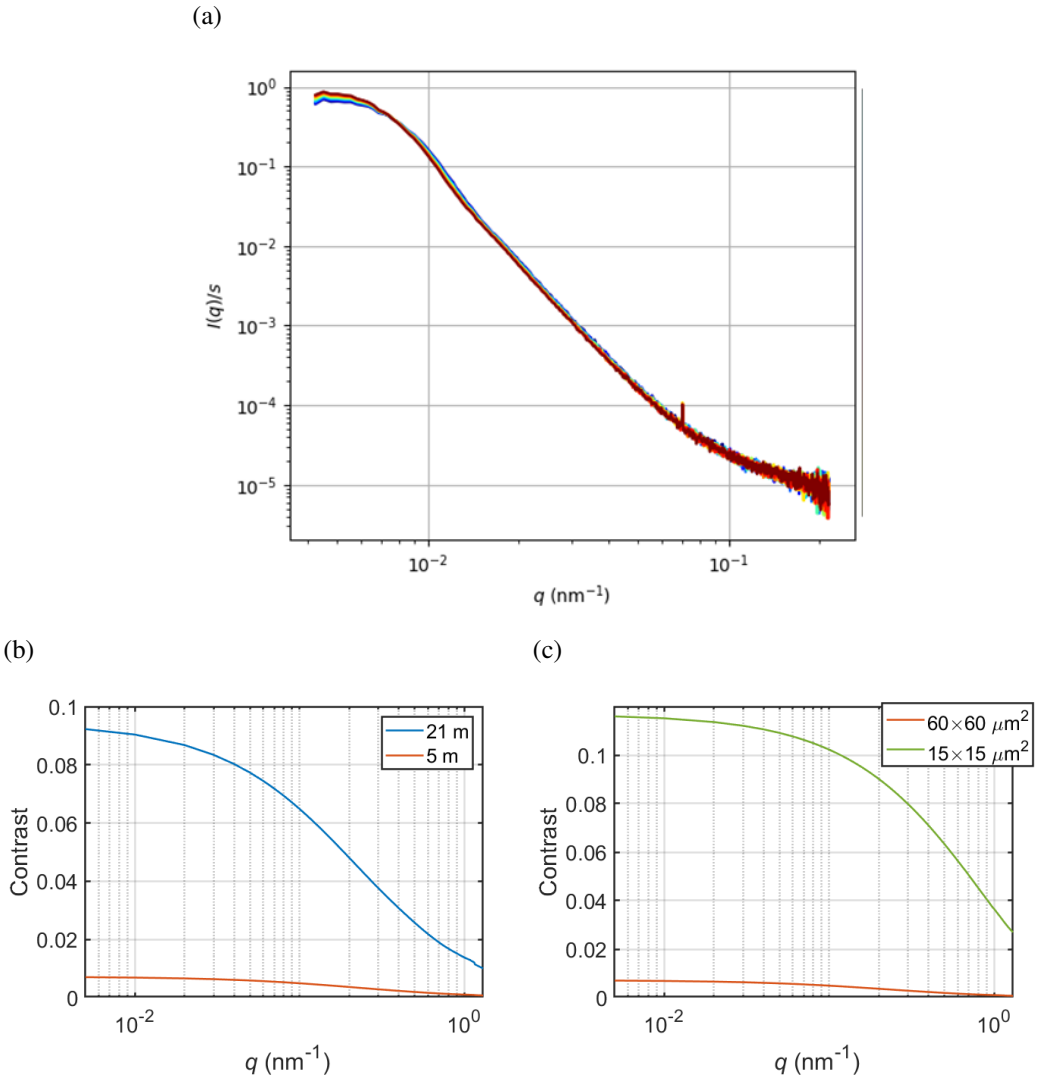

Figure 3.5: a) A typical intensity curve collected for an Ig PEG mixture after a quench to 16°C. b) Contrast calculated with parameters of the beamline P10, with a beam size of 60×60 µm^2 assuming a rectangular beam profile, for $R_{\text{sample-detector}}$ of 5 m and 21 m. c) Contrast calculated with parameters of the beamline P10, with a $R_{\text{sample-detector}}$ of 5 m assuming a rectangular beam profile, with a beam size of 60×60 µm^2 and 15×15 µm^2.

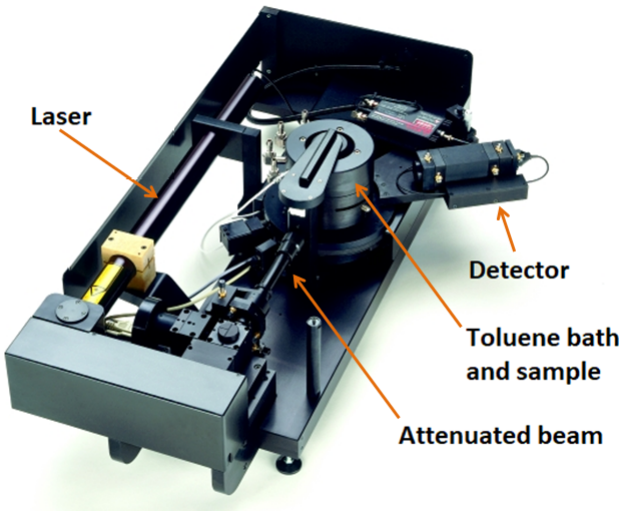

Figure 3.6: Photo of the instrument ALV/CGS-3 (image from www.alvgmbh.de). The most important components of the instrument are pointed out in the image. Those are: the laser, the detector, and the sample holder.

3.3.6 Experimental setup for X-ray Photon Correlation Spectroscopy

3.3.6.1 USAXS XPCS setup

XPCS experiments were conducted at the Coherence Applications beamline P10 at PETRA III, Deutsches Elektronen-Synchrotron (DESY), employing an X-ray beam of photon energy 8.54 keV, a beam size of 100×100 µm^2 and a maximum photon density of 10^7 photons/s/µm^2. The key for performing low dose XPCS experiments is to make use of large beams with a sufficient degree of coherence. Time series of coherent diffraction patterns were collected with an EIGER 4-megapixel detector covering a q range from 0.003 nm^{-1} to 0.05 nm^{-1}.

Silicon absorbers and an X-ray shutter were used to adjust the photon density and minimize the absorbed dose. Threshold values for maximum X-ray exposure times and photon densities were determined by observing X-ray induced changes to static SAXS patterns of both phase separated and homogeneous samples. We estimate the absorbed dose for each sample by the tabulated absorption properties of water with typical values of 5 kGy dose per time series.

3.3.6.2 SAXS XPCS setup

XPCS experiments were conducted at the Coherence Applications beamline P10 at PETRA III, DESY, employing a Silver or Silica absorber to tune the photon count. The detector (Eiger

4-megapixel) was at a distance of 5 m from the sample. The measurement parameters used to collect the dataset in this thesis are summarized in Table 3.1. The temperature controlled used is a Linkam stage. More information can be found at `https://photon-science.desy.de/facilities/petra_iii/beamlines/p10_coherence_applications/index_eng.html`.

	Frames	Exposure time (s)	Flux (ph/s)	T_q (°C)	Beam size (μm^2)	Energy (keV)
1	800	0.005	4×10^{10}	6	21× 13	13.01
2	1000	0.003	1.3×10^{11}	0	20.3×9.1	13.63
3	1000	0.003	1.3×10^{11}	6	20.3×9.1	13.63
4	1000	0.003	1.3×10^{11}	10	20.3×9.1	13.63
5	2000	0.0014	9.44×10^{9}	25	20.3×9.1	13.63

Table 3.1: Summary of the measurement parameters of the SAXS XPCS measurements reported in this study.

3.3.6.3 SAXS XPCS X-Ray Free Electron Laser (XFEL) setup

In this setup, a small angle scattering geometry with a pink beam, i.e., using self-amplified spontaneous emission (SASE) without a monochromator, and a photon energy of 9 keV was used. The detector used is the Adaptive Gain Integrating Pixel Detector (AGIPD)[187], which was placed at a distance of 7.46 m from the sample. The beam is not continuous, but divided in trains with frequency of 10 Hz, which are in turn composed of different pulses, with a delay between two consecutive pulses of 440 or 880 ns. For more detailed information we refer to Refs. [188; 189].

3.4 Neutron quasi-elastic scattering

In this section, the techniques based on neutron quasi-elastic scattering are presented.

In the previous section, the time dependent structure factor was obtained by measuring repeatedly the scattering intensity and monitoring its changes. Here, instead, another approach is used. The key property and difference that we have to take into account when talking about neutrons with respect to photons is their mass. In fact, with objects which have mass the kinetic energy is linked to their velocity via the classical equation $E = \frac{1}{2}mv^2$. The neutrons composing the beam interact with the nuclei of the atoms in the sample and can either have the same energy that they had before the collision (in this case we are talking about elastic scattering) or they will have a gain or loss of energy. This energy difference is linked with the velocity of the particles in the sample, and can therefore give information about the their diffusion properties.

Two quasi-elastic neutron scattering techniques were employed for the experiments in this thesis: Neutron Backscattering (NBS) and Neutron Spin-Echo (NSE). In the first technique the energy of the beam is controlled by means of two monochromators positioned before and after the sample, in order to control both the incoming and the scattered neutrons. In the second one, instead, the spin properties of the neutrons are employed. A Larmor procession of the neutrons is induced by a magnetic field. The Larmor procession angle is anti-proportional to the speed of the neutrons, hence by measuring the polarisation of the beam before and after the scattering events the energy/velocity difference can be obtained.

3.4.1 Neutron Backscattering

Neutron Backscattering (NBS) spectroscopy offers access to molecular dynamics on time and length scales corresponding to the movements of individual proteins and their domains and side chains. As the central quantity, the dynamic structure factor $S(q,\omega)$ is measured as function of the energy transferred $\hbar\omega$ and the scattering vector q to investigate the short time diffusion of the system, giving information on the type of the diffusion, and on parameters such as the diffusion coefficient or the mean squared displacement of a particle [99; 190]. To obtain $S(q,\omega)$, the incoming neutrons go through a velocity selector to define their energy. The analysers collect neutrons with a fixed energy. To be able to probe different energy transferred $\hbar\omega$ at the beamline IN16b the incoming beam goes through a doppler monochromator which is changing the incoming energy of the neutron as represented in Fig. 3.7.

Given the investigated q range, the scattering signal obtained with the NBS experiment is mainly dominated by incoherent scattering and thus focuses on the short time self diffusion. Importantly, the use of D_2O as solvent implies that the hydrogen atoms in the protein and in the PEG contribute more strongly to the neutron scattering signal under these conditions, and the observed dynamical signatures can thus be unambiguously assigned to the protein.

The experiments were performed at the instrument IN16B in its high flux mode at the Institut Laue-Langevin (ILL), Grenoble, France, which offers an excellent energy resolution of 0.8 μeV, allowing to study motions from roughly 100 ps to 10 ns by investigating an energy transfer range of $\Delta E_{\max} = 30$ μeV [191]. IN16B was used with Si(111) monochromator and analyzer crystals, corresponding to an elastic wavelength of 6.27 Å. A linear motor Doppler drive carrying the monochromator was used to define the energy transfer.

The samples were filled into double-walled cylindrical aluminum cans with a 0.15 mm gap and a 23 mm outer diameter, sealed with Indium wire, and mounted in a standard Orange cryofurnace for temperature control during the data acquisition. The typical duration of one full spectra measurement was 1 h and 20 min. The data were reduced using Mantid [192] and further analyzed using own python scripts. The data are available at [193] and [194].

3.4.2 Neutron Spin-Echo

The technique is based on the Larmor precession process. Neutrons have a spin, hence they can precess if they are immerse in a magnetic field. The speed of the precession is determined by the magnetic field, but also by the speed of the neutrons. If a neutron is processing for a

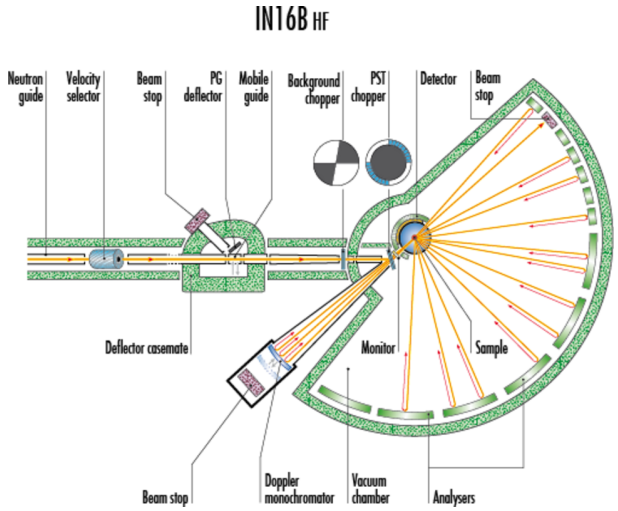

Figure 3.7: The setup of the beamline IN16b at ILL. The image is taken from `https://www.ill.eu/users/instruments/instruments-list/in16b/description/instrument-layout`.

distance L in a magnetic field $\vec{B}$ and right after for a the same distance L in a magnetic field $-\vec{B}$ the position of the spin should be exactly in the same position as the initial point. If a sample is introduced before the change of the magnetic field, and the interaction between the neutron and the sample changes the velocity of the neutron, the final direction of the spin will be different. Hence, by monitoring the initial number of neutrons and the number of neutron reaching the final position with a specific spin direction, it is possible to measure the loss of energy due to the beam-sample interaction. The advantage of this technique is that the energy of the incoming beam does not have to be very precise, since the important parameter is the relative change of energy and not the absolute value of the energy, therefore the flux can be relative high, even if it is necessary to polarise the incoming beam. The time scale and the length scale probed with this technique is very suitable to measure the short-time diffusion of proteins [195]. The measurements were performed at the instrument IN15 at Institut Laue-Langevin, in Grenoble, France. The incident wavelength of the neutron beam was 10 Å, resulting in a Fourier time range covered up to 200 ns. The resolution functions of the instruments were determined for each experimental setup using the elastic scattering of graphite. The resulting intermediate scattering functions were corrected for the background dynamics of the buffer solution with PEG at a concentration of 2.5 %, which is the estimated concentration of PEG in the dense phase [31]. Samples were filled into Hellma quartz cuvettes with a 2 mm gap, and sealed with parafilm to avoid evaporation. The data are available at [194].

Chapter 4

Simulations

4.1 Numerical solution of the Cahn-Hilliard equation

The simulations performed for this thesis are based on the Cahn-Hilliard Equation (CHE). The equation that was solved in two dimensions, derived in Section 1.1.2, is the following:

$$\frac{\partial \phi}{\partial t} = -\nabla \mu \nabla (\nabla^2 \phi + \varepsilon \phi - \phi^3) \tag{4.1}$$

where $\varepsilon = \frac{T_c - T_q}{T_c}$ denotes the quench depth with respect to the critical temperature (T_c) of the spinodal decomposition.

The function $\rho(r_x, r_y, t)$ is the protein density, which is related to the order parameter ϕ through $\rho(r_x, r_y, t) = \frac{\phi(r_x, r_y, t)+1}{2}$.

The differential equation Eq. 4.1 was solved numerically in a 512×512 discretized space using the Euler method [196] with Matlab. The Laplacian was approximated with the five-point formula [48], so that $\nabla^2 \phi(r_x, r_y) \simeq \frac{1}{h^2}(\phi(r_x+1, r_y) + \phi(r_x-1, r_y) + \phi(r_x, r_y+1) + \phi(r_x, r_y-1) - 4\phi(r_x, r_y))$.

Hence, given $\phi(r_x, r_y, t)$ it is possible to calculate $\phi(r_x, r_y, t+1)$ via:

$$\phi(r_x, r_y, t+1) = \phi(r_x, r_y, t) + t_s \mathfrak{F}(\phi(r_x, r_y, t)) \tag{4.2}$$

If we define

$$\begin{aligned}\psi(r_x,r_y,t) &= \nabla^2\phi(r_x,r_y,t)+\varepsilon\phi(r_x,r_y,t)-\phi^3(r_x,r_y,t)\\ &\simeq \frac{1}{h^2}[\phi(r_x+1,r_y)+\phi(r_x-1,r_y)+\phi(r_x,r_y+1)+\phi(r_x,r_y-1)]+\\ &\quad +[\varepsilon-\frac{4}{h^2}]\phi(r_x,r_y,t)-\phi^3(r_x,r_y,t),\end{aligned} \tag{4.3}$$

than the function $\mathfrak{F}$ can be written as

$$\begin{aligned}\mathfrak{F}(\phi(r_x,r_y,t)) &= \nabla\mu(\phi(r_x,r_y,t))\nabla\psi(r_x,r_y,t)\simeq\\ &\simeq \frac{1}{h^2}\{\mu(r_x+\frac{1}{2},r_y,t)[\psi(r_x+1,r,y,t)-\psi(r_x,r_y,t)]+\\ &\quad +\mu(r_x-\frac{1}{2},r_y,t)[\psi(r_x-1,r_y,t)-\psi(r_x,r_y,t)]+\\ &\quad +\mu(r_x,r_y-\frac{1}{2},t)[\psi(r_x,r_y-1,t)-\psi(r_x,r_y,t)]+\\ &\quad +\mu(r_x,r_y+-\frac{1}{2},t)[\psi(r_x,r_y+1,t)-\psi(r_x,r_y,t)]\},\end{aligned} \tag{4.4}$$

with $\mu(r_x+\frac{1}{2},r_y,t)=\frac{1}{2}\mu(r_x+1,r_y,t)+\frac{1}{2}\mu(r_x,r_y,t)$.

The time step used is $t_s=0.1$ and the space step $h=1.5$, the parameters were tuned to have a stable solution and the largest time step possible to reduce simulation time. Periodic boundary conditions were introduced to avoid the presence of interfaces in the simulations.

The kinetics of the system is expected to depend on the dimensionality of the system. In fact, the correlation length depends on time with the power law $\xi \propto t^{\frac{1}{d}}$, with d being the dimensionality of the system [197]. Thus, the main purpose of our simulations is to serve the interpretation of the trends, but it is not used for a quantitative analysis.

The initial concentration was set to $\phi = 0.4$ plus an independent fluctuation at each grid point which was modelled by a uniformly distributed noise with amplitude dependent on the quench temperature (set to 0.5 T_q). The deterministic modified Cahn-Hilliard Equation (CHE) was then solved. We note that the presence of noise was shown to be asymptotically irrelevant for large times. This is because fluctuations only affect the interfacial profile. However, the fixed length scale of the interface becomes irrelevant in comparison with the diverging domain scale [198].

4.2 Concentration dependent mobility

To introduce a dependency of $\mu(r,t)$ on the protein concentration the following expression was used

$$\mu(r_x, r_y, t) = \frac{1}{1 + exp\{M[\phi(r_x, r_y, t) - c_g)]\}} \tag{4.5}$$

following the approach of Ref. [48], with $M = 50$.

This function was chosen in order to have a fast-decaying continuous function. Examples of the dependency of μ on ϕ for different values of c_g is shown in Fig. 4.1.

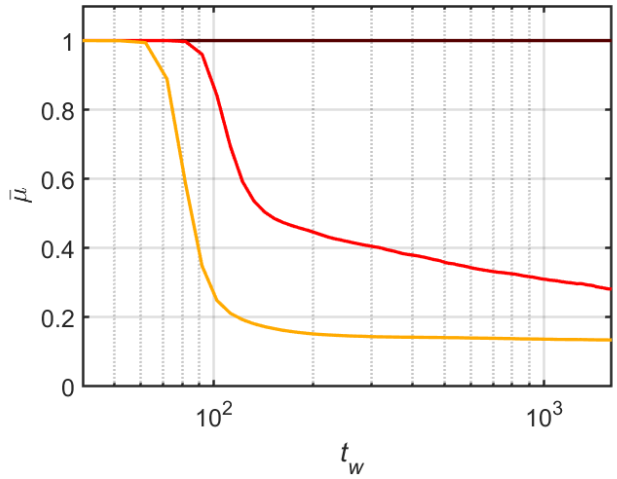

Figure 4.1: The mobility as a function of ϕ for the different values of c_g, which were used in the simulations.

Other approaches have been used in literature to have a more precise description of the gelation process [35], in which the CHE is coupled with a second differential equation which describes the gel transition in the system. However, since the mobility of Eq. 4.5 gives a more stable differential equation and the resulting simulation can describe the experimental results this approached was not followed.

4.3 From real to reciprocal space

The two dimensional fast Fourier transform (fft) of $\rho(r_x, r_y, t)$ was calculated to obtain an equivalent of the two dimensional experimental scattering intensity, so that

$$I(\vec{q},t) = |\text{fft}(\rho(r_x, r_y, t))|^2. \tag{4.6}$$

This intensity is equivalent to experimental data with a fully coherent beam.

The analysis to obtain 1D intensity curves and the correlation function was performed following the same procedure of the experimental data, hence performing an azimuthal integration. The two-time correlation functions were also obtained following the same procedure used for the experimental data (for more information see Section 3.3.2).

Chapter 5

Measurement protocol

5.1 Temperature quenches

The very fast temperature quenches pose an experimental challenge when using temperature sensitive samples in particular systems that depend on their thermal history, as the polymer protein mixture in solution investigated in this thesis. This solution is stable and in one phase with concentration c_i at high temperature $T_{high} > 21°C$, but once the solution is quenched to a temperature T below 21°C the phase separation occurs, resulting in the formation of domains with concentration $c_{\text{dilute}}(T)$ and $c_{\text{dense}}(T)$ which grow with time. If the temperature is changed once again to a temperature T', the system will proceed to separate again in two liquid phases with concentration $c_{\text{dilute}}(T')$ and $c_{\text{dense}}(T')$. If a quench from T_{high} to T' is compared to one from T to T', they will both result in domains with concentration $c_{\text{dilute}}(T')$ and $c_{\text{dense}}(T')$, but the kinetics of the phase separation can be vary different since the initial concentration in the first case is c_i and in the second case it is $c_{\text{dilute}}(T)$ or $c_{\text{dense}}(T)$. It is possible to "delete" the memory of the system by increasing the temperature to a value higher than 21°C and let it equilibrate. In this way the solution can return to the initial state, meaning that all the domains are dissolved and the solution is stable with the initial concentration c_i.

Before each temperature quench the system was stabilized at 37°C for 10 min, the quench was performed from 37°C to a temperature T_q.

Two different types of measurements were performed: one during the formation of the LLPS domains and one during the arrest or coarsening depending on the temperature. In the first one the aim was to follow the kinetics of early stage of the phase separation, for this reason the sample was monitor right after the temperature quench started.

In the second one, instead, the equilibrium properties of the phase separated solution where

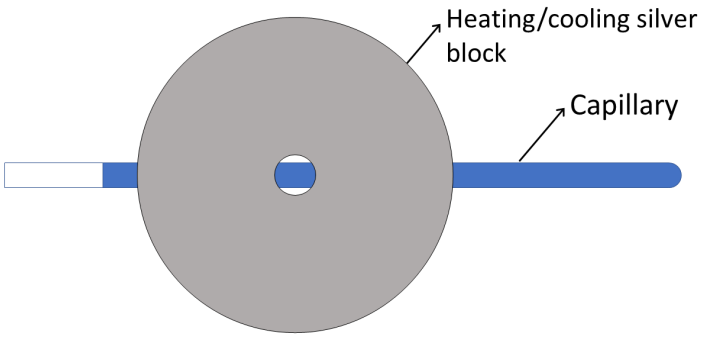

Figure 5.1: A sketch of the sample holder of the Linkam stage.

investigated. To be sure that this stage was reached, the sample was quenched to the desired temperature T_q and the measurements were performed after 10 min for the XPCS measurements and after 1 h for the quasi elastic neutron scattering measurement. It is worth mentioning that the neutron and x-ray experiment had different temperature controls, hence the quench rate was different. Since the diffusion was measured after equilibration the differences were considered negligible .

5.2 Measurements with Linkam stage

For the measurement during phase separation the quenches were performed with a Linkam stage, to make the temperature change more reproducible. The quench rate was set to 150 K/min.

The stage is composed of a silver block in which the capillary is inserted, and a 2 mm hole where the X-ray beam can interact with the sample without coming to contact with the block as represented in Fig. 5.1.

Interestingly, the sample shows an anisotropy of the scattering pattern during phase separation (Fig. 5.2). Similar anisotropic scattering was observed for samples during a spinodal decomposition under shear flow [32; 199; 200]. In presence of a flow, the effective diffusion coefficient in the direction of the flow is higher, hence the growth of the domains is favoured, as a result the domains become elongated aligned in the direction of the flow [201]. As we see from Fig. 5.2 in the middle of the capillary the scattering seems to be isotropic, suggesting that the possible shear flow does not affect the diffusion in this region.

The possibility of shear flow is supported by the two-time correlation functions as seen

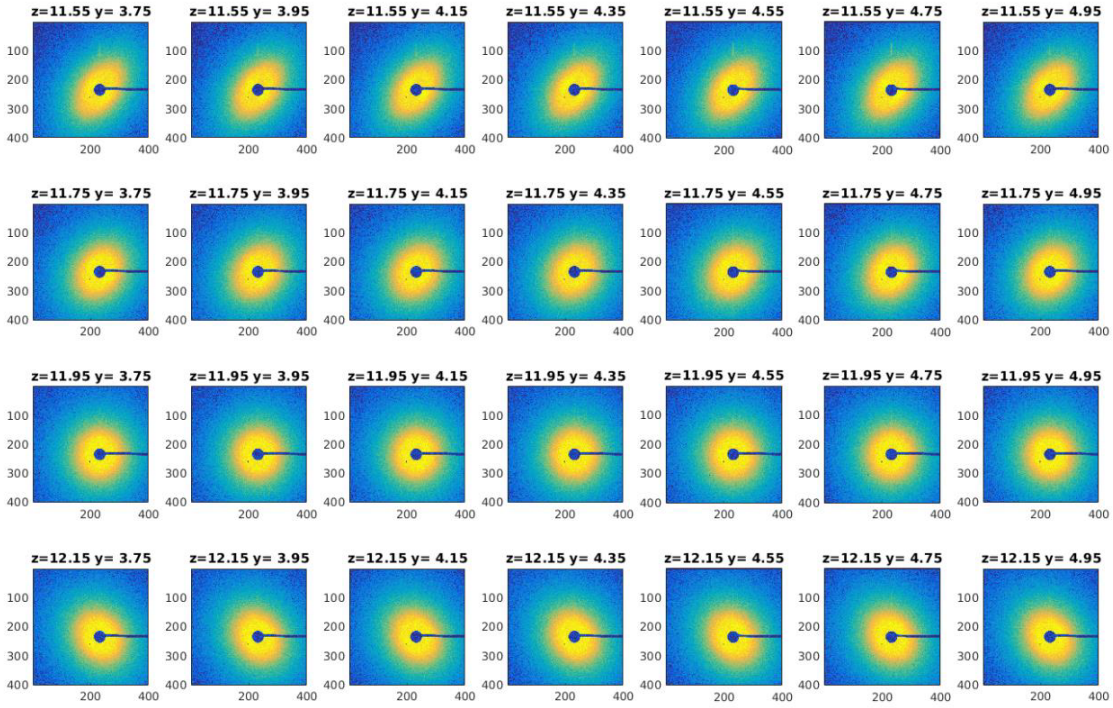

Figure 5.2: The 2D scattering pattern measured at different position on the y (horizontal direction along the capillary length) and z (vertical direction orthogonal to the capillary length) in millimeters.

in Fig. 5.3 the same measurement was repeated at different distances from the bottom of the capillary. From the correlation map, it is visible that in the bottom of the capillary the correlation function is decaying smoothly, while approaching the middle of the capillary the loss of correlation is very sudden, and it is reversible, meaning that the correlation repeatedly decreases and increases. This can be observed not only for this sample, but for many others such as egg white, egg yolk, colloidal nanoparticles and BSA with YCl_3 and exclusively when the Linkam stage is heating or cooling. Most probably there is a temperature gradient in the sample that is causing a flow inside of the sample. This problem is not present in the end of the capillary. A possible explanation is that the additional wall reduces the overall flow of material. A second possibility is the presence of only one temperature gradient, as opposed to the middle of the capillary as represented in Fig. 5.1 where both the top and the top of the capillary are outside the silver block.

To mimic the bulk conditions as close as possible, the measurements were performed only in the position where the scattering was not anisotropic and in the bottom of the capillary.

The volume of the solution changes due to thermal expansion (Fig. 5.4). The corresponding change of volume reaches a minimum of $\sim$-2.5 mm^3 (Fig. 5.5) which given a capillary of radius of 0.75 mm and that the capillary length was filled for 6 cm, it corresponds to circa 0.23% of the total volume, which was considered a negligible effect on the diffusion of the particle in the sample.

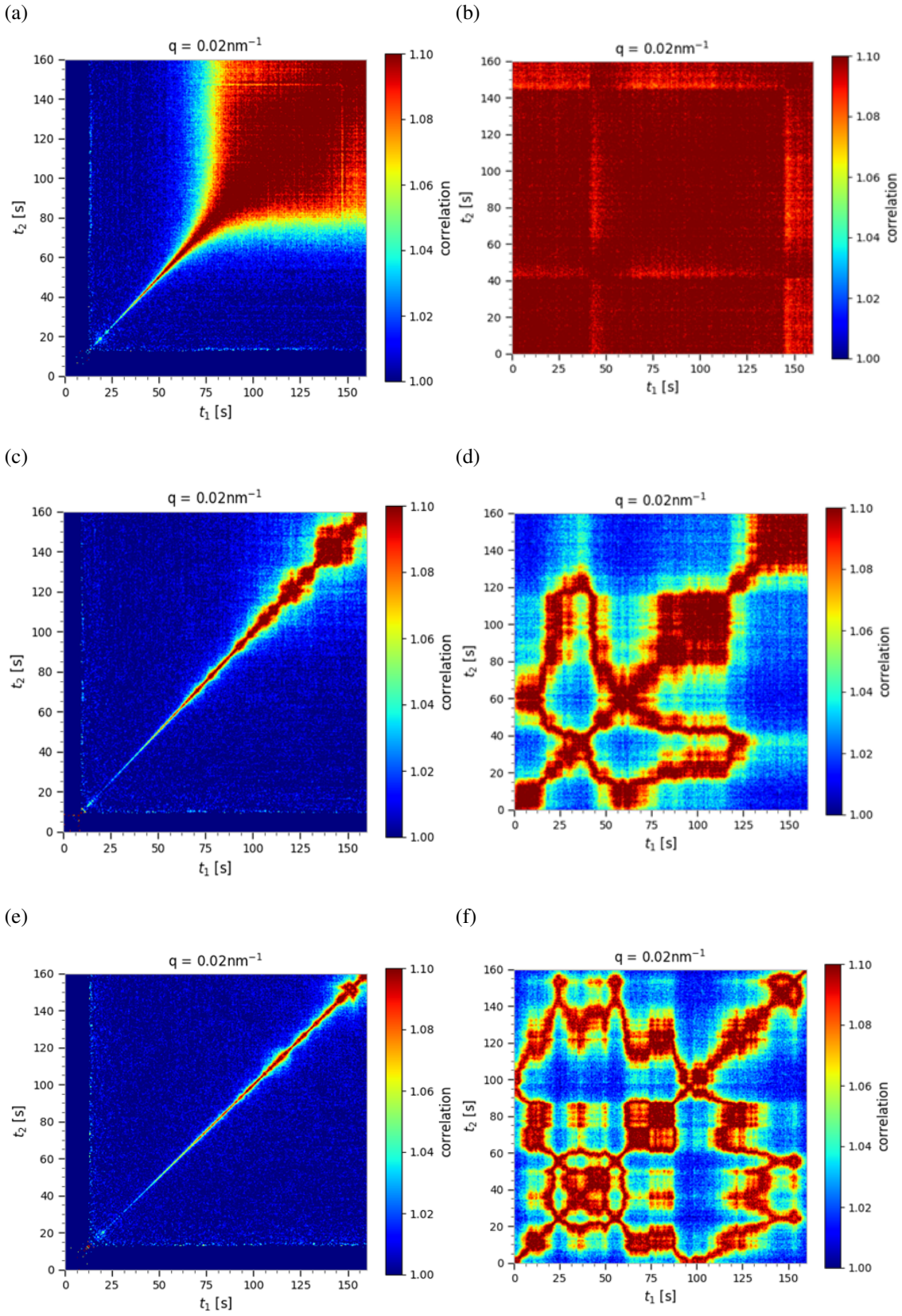

Figure 5.3: The two-time correlation functions of two consecutive measurement of Ig 200 mg/ml PEG 12% right after a quench from 37°C to 2°C at a distance 7 mm (a,b), 15 mm (c,d) and 19 mm (e,f) from the bottom of the capillary.

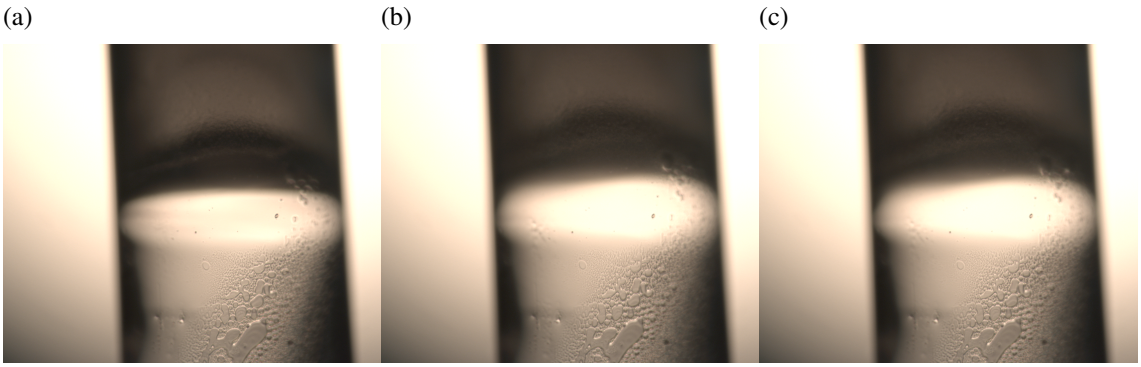

Figure 5.4: The effects of thermal expansion on an Ig-PEG sample visible via microscopy on a quench from 37°C to 2°C. The images show the sample right after the start of the temperature change (a), and after 5 min (b) and 10 min (c).

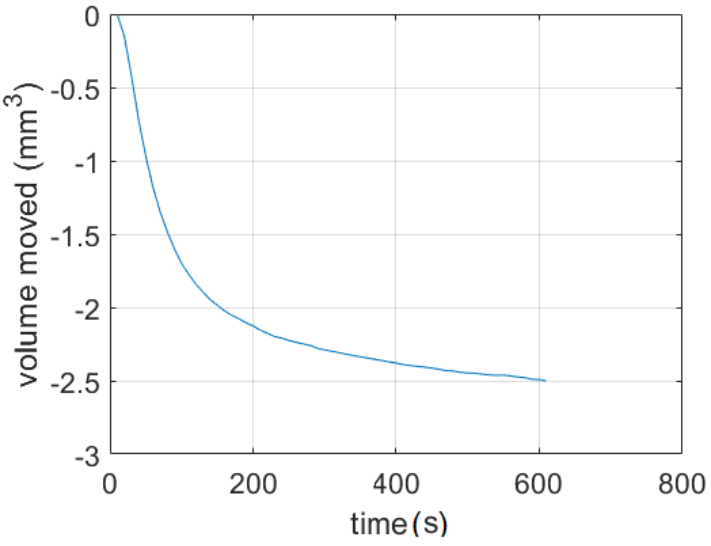

Figure 5.5: The volume change due to thermal expansion estimated by the microscopy images as a function of time, from time 0 s, i.e. when the quench starts, to 600 s later. The final temperature of 2°C was reached after circa 60 s.

Part III

Results

Chapter 6

Microscopic dynamics of liquid-liquid phase separation and domain coarsening

This section is based on Ref. [202].
While the interplay between liquid-liquid phase separation (LLPS) and glass formation in biological systems is highly relevant for their structure formation and thus function, the exact underlying mechanisms are not well known. The kinetic arrest originates from the slowdown at the molecular level, but how this propagates to the dynamics of microscopic phase domains is not clear. Since with diffusion, viscoelasticity and hydrodynamics distinctly different mechanism are at play, the dynamics needs to be monitored on the relevant time and length scales and compared to theories of phase separation. Using XPCS we determine the LLPS dynamics of a model protein solution upon low temperature quenches and find distinctly different dynamical regimes. We observe that the early stage LLPS is driven by the curvature of the free-energy and speeds up upon increasing quench depth. In contrast, the late stage dynamics slows down with increasing quench depth, fingerprinting a nearby glass transition. The dynamics observed shows a ballistic type of motion implying that viscoelasticity plays an important role during LLPS. We explore possible explanations based on Cahn-Hilliard theory incorporating non-trivial mobility parameters and find that this approach can only partially explain our experimental findings.

6.1 Introduction

Recent work suggests that structure formation in biology can take place, inter alia, through liquid-liquid phase separation (LLPS) [7; 203; 14]. Phase separation in crowded environments

thus represents a mechanism for intracellular organization via the formation of biomolecular condensates [204]. The biological functions of these condensates are currently intensely investigated, including steering biochemical reaction rates, sensing or signalling [14]. LLPS is also associated with a variety of diseases caused by a loss and/or change of function of the condensates [205; 206].

The state of the condensates depends on the dynamic processes during their formation, often involving non-equilibrium processes over a hierarchy of length and time scales [203; 42]. A case in point is the slowdown of the dynamics on molecular length scales caused by concentration and its influence on dynamical and structural properties of the condensate on mesoscopic length scales. Ultimately, such a microscopic slowdown can lead to the arrest of LLPS on larger length scales accompanied by the formation of bicontinuous gel network structures [107; 207; 45].

The kinetics of arrested phase separations in protein solutions have been studied successfully in the past demonstrating that the ensemble-averaged structure factor ceases to develop further in q-position and intensity upon low temperature quenches [208; 54; 53; 61; 31]. However, the dynamics of protein solutions en-route to an arrested LLPS is largely unknown mainly because of the requirement to monitor an exceptionally broad range of time and length scales simultaneously. This, in turn, prevented the experimental validation of models of the dynamics of critical phenomena during LLPS such as the Cahn-Hilliard equation and related models, especially in the vicinity of glass-gel transitions displaying large dynamical asymmetries between the species involved [203].

LLPS is a general phenomenon, which is relevant not only for protein systems, but also in many other fields of science [209]. LLPS domains were studied with different microscopy techniques [210; 57]. Its macroscopic properties such as turbidity and viscosity [211; 212; 60] as well as molecular properties [212; 16; 213; 214; 215; 216; 121] were monitored. Various scattering techniques were used to access the kinetics of phase separation [61; 31; 211; 60].

X-Ray Photon Correlation Spectroscopy (XPCS) employing coherent X-rays can resolve the collective dynamics on the required length scales, ranging simultaneously from nanometres to microns and time scales from microseconds to hours [136; 182; 217; 218; 133; 119; 219; 220]. Here, we demonstrate that a combination of scanning techniques, large beams, and long sample detector distances [155; 131; 158] allows us to reduce the required X-ray doses to values below the critical dose of many protein systems [221]. More details on the experimental parameters are provided in Section 3.3.4. With this approach, we are able to follow the dynamics during a LLPS of γ-globulin (Ig) in a concentrated aqueous PEG solution. The ex-

perimental results are compared with simulations based on the Cahn-Hilliard equation taking the gel transition into account (in the spirit of model C according to Ref. [203]) [203; 48; 35].

6.2 Results and discussion

6.2.1 Kinetics of phase separation

The sample investigated in this study was prepared as described in Chapter 2, the sample used is sample A from table 2.1. Fig. 6.1a displays the temporal evolution of the scattering intensity as a function of scattering vector q for a quench temperature of T_q =10°C (other quench temperatures in Fig. 6.2a and 6.2b), capturing the LLPS process during the first 60 s. The X-ray intensity increases rapidly during the early time of the phase separation and the position of the spinodal peak q_{max} shifts to smaller values indicating an increase in length scales of the concentration fluctuations. Appropriately normalizing the intensity and wavevectors by the respective peak intensities $I(q_{max})$ and positions q_{max}, we obtain a master plot as expected for spinodal decomposition [222] (inset Fig. 6.1a, 6.2c, and 6.2d). $I(q_{max})$ shows a rapid increase during the early stage with a rate determined by the quench depth, while at around 10 s the growth starts to slow down considerably (Fig. 6.1b). This slowdown is more pronounced when quenched to lower temperatures, while at higher temperatures, $I(q)$ continues to grow even beyond 40 s - albeit on a slower rate.

In figure 6.3, the intensity increases, or, in other words, the phase separation starts, before $t_w = 0$ s, because the sample phase separates right below 21°C, when it enters in the metastable region of the phase diagram. Fitting Eq. 6.1, this can be further quantified by the parameter t_s indicating the time necessary for the system to go from 21°C to the quench temperature T_q.

$$I(q,t) = \exp(R_{exp}(t - t_s)) \tag{6.1}$$

The change in intensity with t_w right after quench does follow an exponential increase as expected from a system that follows the Cahn-Hilliard equation [1] (for further details see Section 1.1.2).

The value of t_s naturally decreases with quench temperature T_q, since it takes more time for the sample to reach the quench temperature. The rate R_{exp} is, instead, constant within the error bars. This is also to be expected, because this early increase depends only on the temperature of the system when the exponential increase happens.

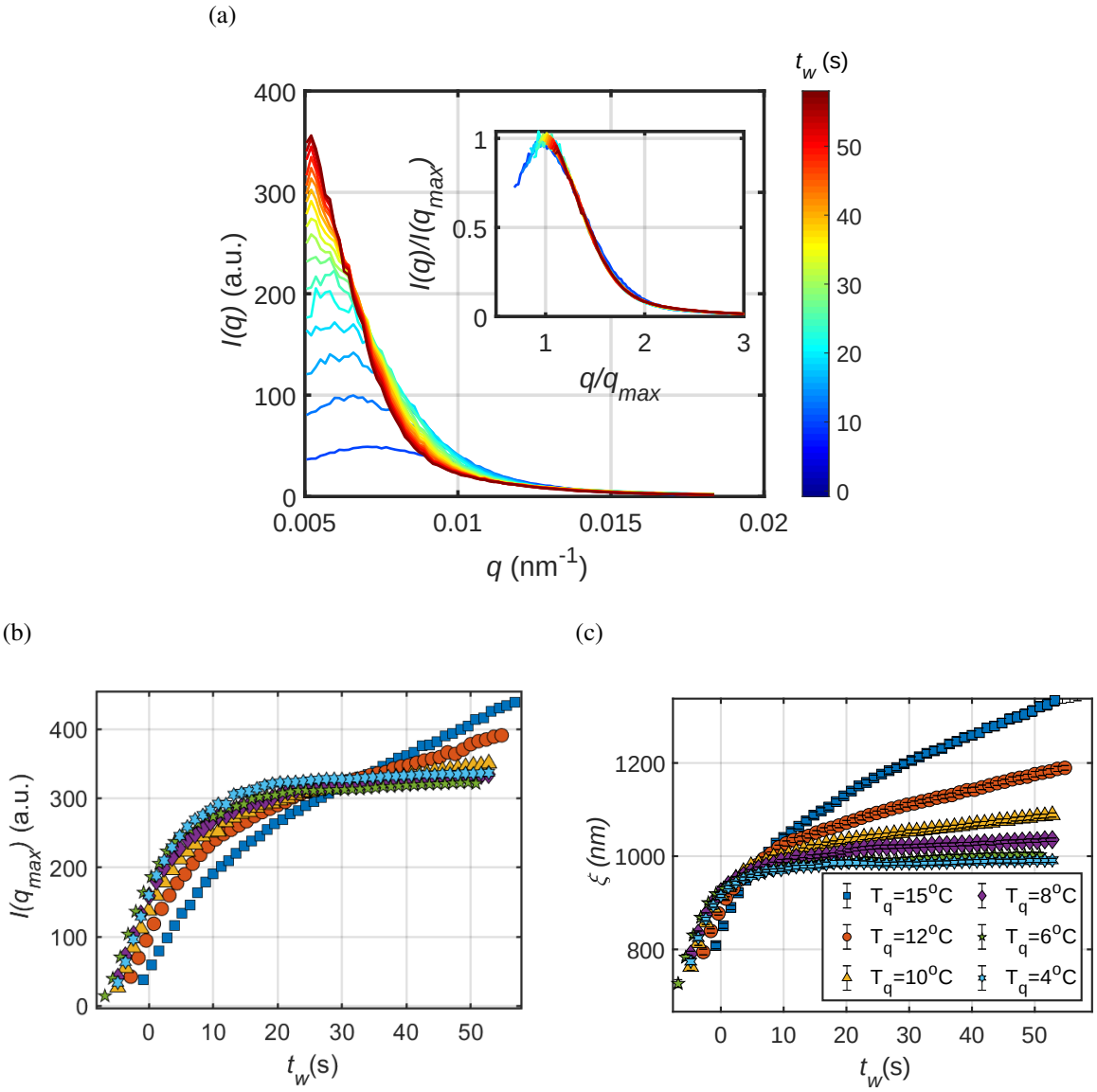

Figure 6.1: a) Intensity $I(q)$ as a function of scattering vector q for a quench temperature T_q= 10°C, in the inset the rescaled intensity. The different colours correspond to different waiting times t_w as indicated in the colour bar. The time t_w =0 s is the time at which the quench temperature T_q was reached. b) The intensity at the peak position as a function of time for different temperatures. c) The peak position as a function of time for different temperatures. The error bars are within the symbol size if they are not visible.

Fitting $R_{exp}(q) = Aq^4 + Bq^2$ (Fig. 6.1d), and comparing the theoretical value of $R(q)$, we can calculate the mobility for the system at the temperature right below 21°C. The fit was performed in a time range of 3 s, in which the temperature is changing. The term $B = -\mu_0(\varepsilon +$

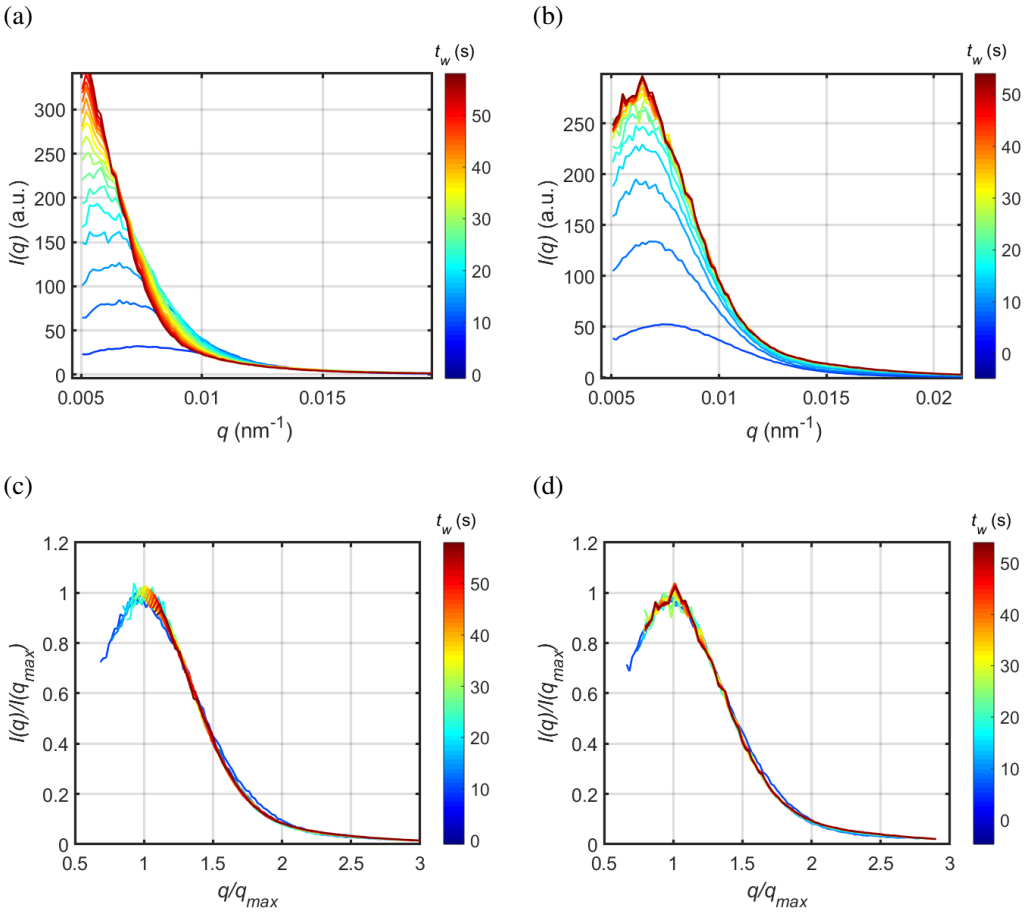

Figure 6.2: a) Intensity $I(q)$ as a function of wave vector q at different waiting times t_w measured after a quench to $T_q = 15°C$ and b) $T_q = 4°C$. c and d) The rescaled intensities as a function rescaled wavevectors corresponding to the profiles shown in (a) and (b).

$3\phi_0^2$) depends on the quench depth, so the estimated value will be an effective one, in which the quench depth is substituted by its average in the time/temperature range considered. The term $A = \mu_0$, instead, does not contain the quench depth, hence an estimation of the mobility can be extracted, giving $\mu_0 = (2.0 \pm 0.2) \times 10^{-4}$ µm^2/s.

6.2.2 Two time correlation functions

Insights into the dynamics during the LLPS are obtained by analysing time series of the coherent X-ray speckle patterns. For this, we calculate the two-time correlation functions (TTCs)

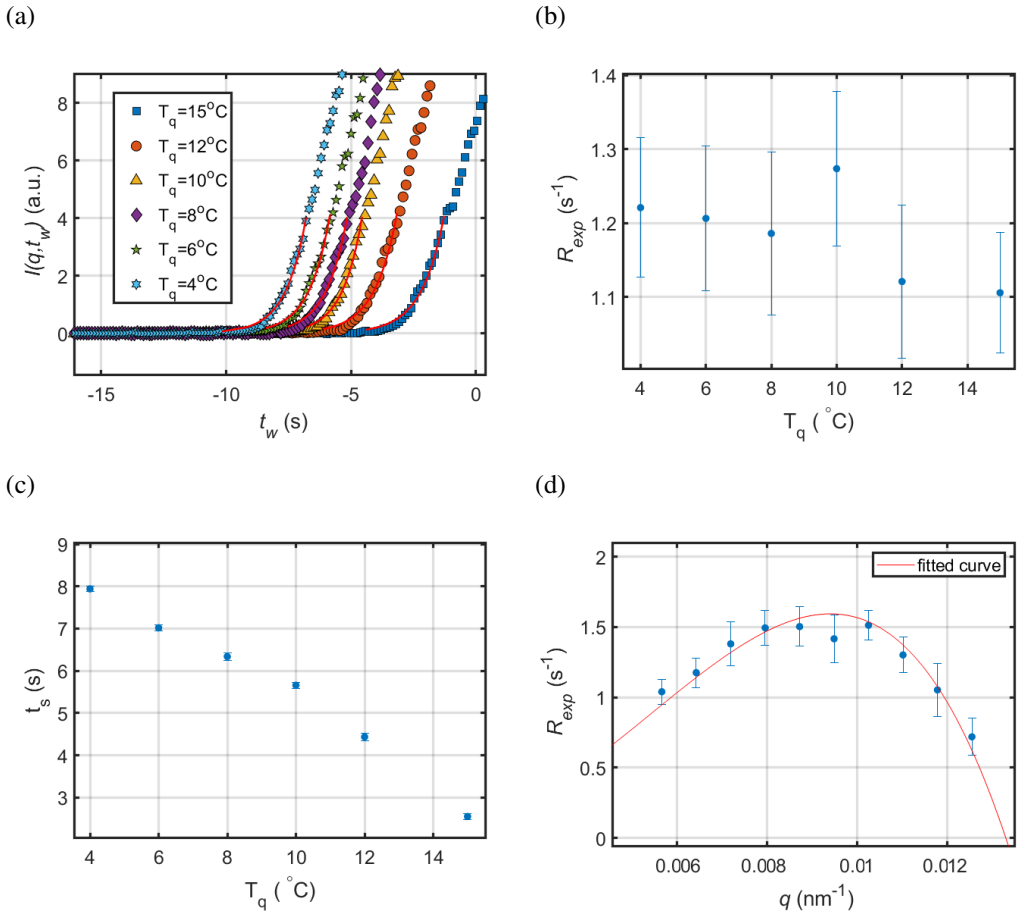

Figure 6.3: a) Intensity at q =0.008 nm^{-1} as a function of waiting time t_w, the experimental data (colours indicated in the legend) with the fit of an exponential function. b) The parameters R_{exp} and c) t_s as defined from Eq. 6.1 indicated as a function of quench temperature calculated at q =0.008 nm^{-1}. d) The parameters R_{exp} calculated at different q values, for the measurement in which the system was quench to T_q =4°C. To increase the stability of the fit the time t_s was fixed to a value of 8 s.

for specific scattering vectors q and different quench depths via:

$$C(t_1,t_2,q) = \frac{\langle [I(t_1)-\bar{I}(t_1)][I(t_2)-\bar{I}(t_2)]\rangle}{\sqrt{[\bar{I^2}(t_1)-\bar{I}^2(t_1)][\bar{I^2}(t_2)-\bar{I}^2(t_2)]}}) \tag{6.2}$$

with $< \cdot >$ being an average over detector pixels corresponding to a specific range $q \pm \delta q$ (calculated for q from 5 to 1.1 µm^{-1} and $\delta q = 0.3$ µm^{-1}) and $\bar{I}(t_1) =< I(t_1) >$. From this quantity the time dependent $g_2(t,t_w,q) = C(t+t_w,t_w,q)$ have been extracted by horizontal cuts

along t_1 starting at the diagonal of the respective TTC [181].

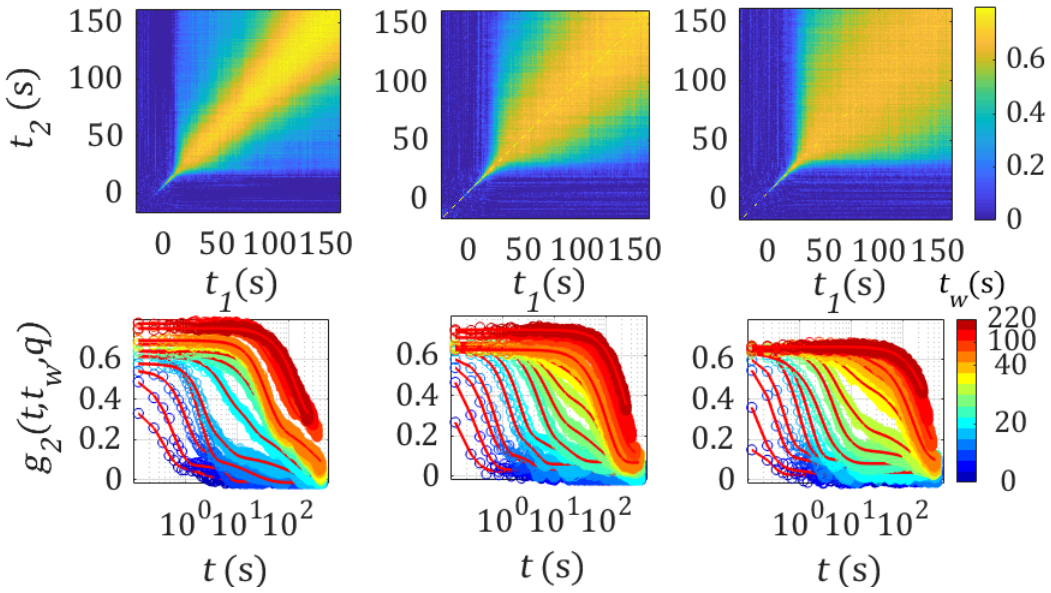

Figure 6.4: In the upper panels the two-time correlation function for T_q =15°, 8°C and 4°C (left to right) at q =0.005 nm^{-1} are displayed and the lower panels show the corresponding g_2 functions at different waiting times t_w.

Fig. 6.4 shows the TTCs in the upper panel and the correlation function $g_2(t,t_w,q)$ for quench temperatures of T_q =15°C, 8°C and 4°C (from left to right), respectively in the lower panels. We identify three stages of the dynamics during LLPS: the first stage appears directly after the quench in the first 20 s, and its very fast dynamics is visible only by a thin line in the TTC and by the final part of the decay in the correlation function. After this early stage, the TTC shows a pronounced slowing down of the dynamics accompanied by a rising background level visible by the appearance of a square-like feature. This corresponds to a second relaxation mode with a much slower relaxation time appearing in the g_2 functions. The contribution of this relaxation channel to the overall decay is increasing rapidly. After ca. 40 s the fast process in the LLPS is coming to an end as evidenced by the disappearance of the first decay. In the third stage, later also called late stage, the TTC evidences a second slowing down process with the relaxation time depending on the final quench temperature with slower dynamics visible for lower temperatures (from T_q =15°C to T_q =4°C, on the top row of Fig. 6.4). The $g_2(t,t_w,q)$ functions have been fitted by a sum of Kohlrausch–Williams–Watts

(KWW) functions [223] resulting in the following equation (Eq. 6.3):

$$g_2(t,t_w,q) = A_1 \exp\left[-\left(2\frac{t}{\tau_1}\right)^{\gamma_1}\right] + A_2 \exp\left[-\left(2\frac{t}{\tau_2}\right)^{\gamma_2}\right] \tag{6.3}$$

with decorrelation times τ_1 and τ_2, the relaxation amplitude A_1 and A_2, and KWW exponents γ_1 and γ_2, and the waiting time t_w, where $t_w = 0$s is the time at which the temperature is reached. We note that for some g_2 functions a third exponential decay with small amplitude and slow decay is needed to describe additional tails in g_2 at very long time scales. However, due to the low statistics of the third decay, we evaluate only the two leading decays here.

Fig. 6.5a displays the relaxation times as a function of waiting time t_w. We identify an exponential increase of the relaxation time in the early stage of the LLPS and faster dynamics with increasing quench depths (see inset of Fig. 6.5 a and c). To quantify this the decorrelation time of the fast mode has been fitted with an exponential function as shown in Eq. 6.4.

$$\tau_1 = \tau_0 \exp(r t_w) \tag{6.4}$$

The rate of growth increases with temperature (Fig. 6.7b) which is consistent with the fact that at this early phase of the spinodal decomposition the dynamics is driven by the curvature of the free energy $\frac{\partial^2 F}{\partial c^2}$, which increases in magnitude with deeper quenches (lower temperatures) and thus speeds up the dynamics.

This picture reverses when the slow relaxation sets in (τ_2 in Fig. 6.5c)). Now the relaxation times for the lower temperatures are considerably larger than the high temperature quenches. Its dependence on the waiting time is also changing, infact the growth of the values follows a power law (Fig. 6.8) shown in Eq. 6.5. Interestingly, the pre-factor $a(T_q)$ has a fast increase as the temperature decreases, in a fashion that reminds the Vogel–Fulcher–Tammann equation [224; 225; 226] suggesting the closeness to the glass line. We note that the exponent x is deviating from its predicated value of 2/3 for a classical spinodal decomposition [219] especially at lower temperatures.

$$\tau_2 = a(T_q) t_w^x \tag{6.5}$$

The transition from dynamics dominated by the fast decay to dynamics dominated by the slow decay is quantified by the non-ergodicity parameter [227], defined as $f = \frac{A_2}{A_1+A_2}$. A rather sharp increase of the non-ergodicity parameter around $t_w = 30$ s is observed (Fig. 6.5b). The time at which f rises time is larger and slower for lower temperatures, suggesting that

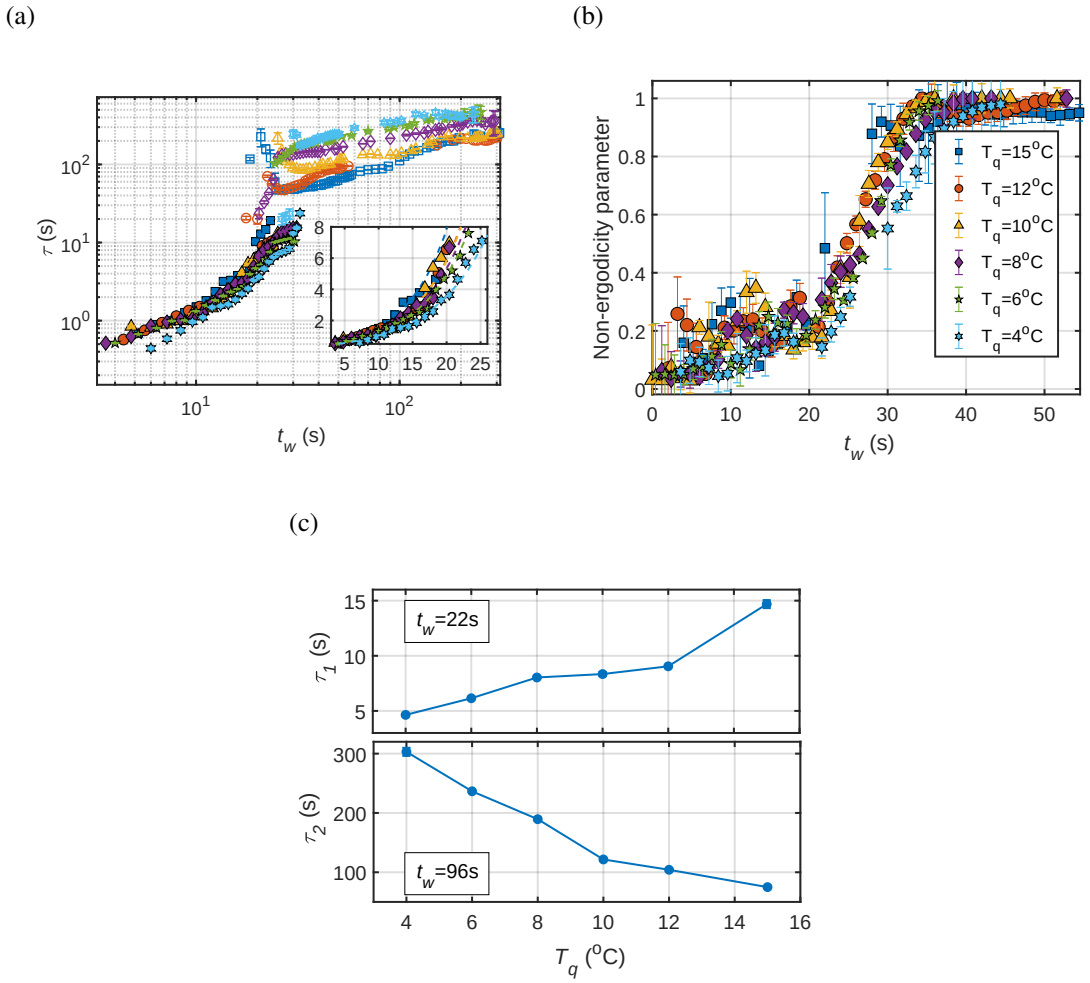

Figure 6.5: (a) Decorrelation time for q=0.005 nm^{-1} as a function of waiting time t_w. The open symbols correspond to the slow mode (τ_2) and the filled symbols to the fast one (τ_1). Inset: linear representation of τ_1. (b) Non-ergodicity parameter $f = \frac{A_2}{A_1+A_2}$ as a function of t_w. The legend also applies to (a). c) Decorrelation time of the fast and slow mode as a function of quench temperature T_q, respectively.

the transition to coarsening dynamics is already slowed down by the lower mobility at low temperatures.

These three stages in the dynamics can be linked to the evolution of the LLPS: The first corresponds to the early stage of a spinodal decomposition, displaying an enhancement of the concentration fluctuations and the formation of an interface between two different phases. The third one is the late stage in which the domains are growing. For our system this seems to be controlled by the mass transport mechanism and by the mobility of the involved components,

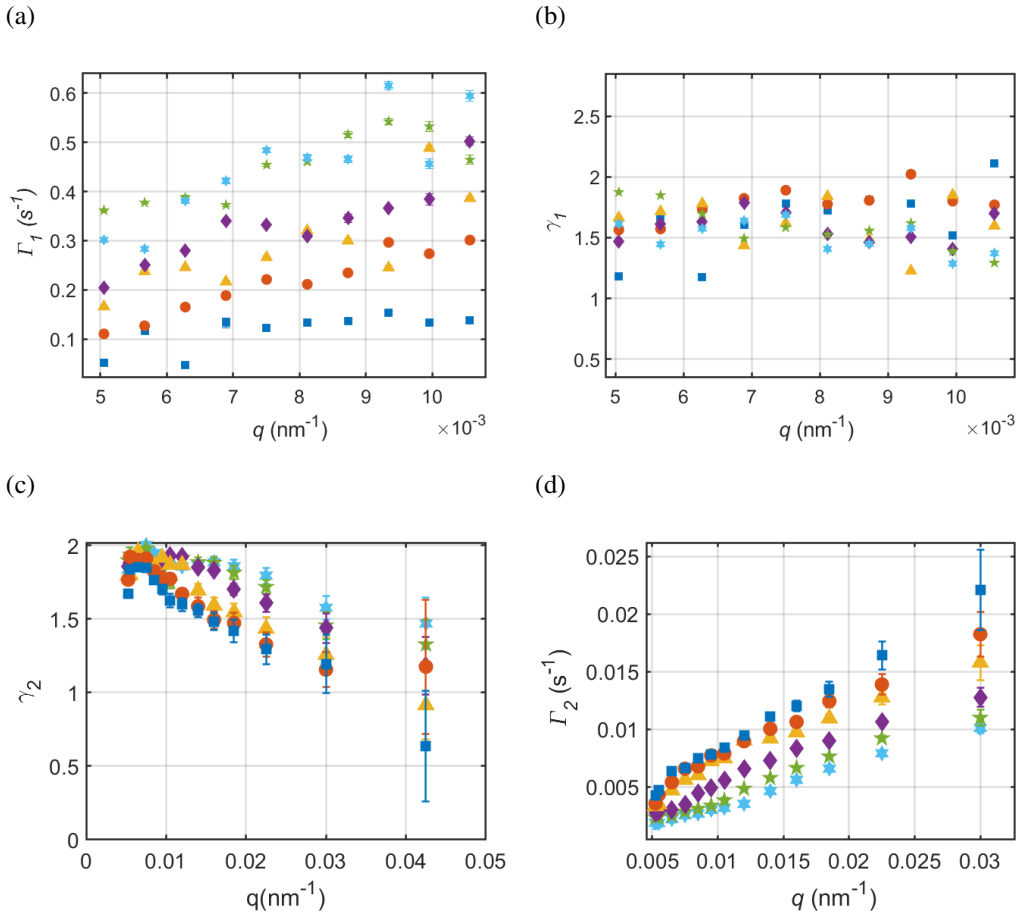

Figure 6.6: a)Decorrelation rate and b)KWW of the fast mode at time $t_w = 19$ s. c) The decorrelation time and d) KWW for the slow mode were obtained by averaging $g_2 - 1$ on a time window from t_w =220 s to 460 s. Different symbols correspond to different quench temperature. the legend is depicted in Fig. 6.1

whereas in other cases in condensed matter physics, different domain growth mechanisms have been identified [38]. The second stage is a transition between the early and late stage.

Important for the assessment of the form of dynamics and relevant for computing quantities such as diffusion and transport coefficients during the LLPS are the relaxation rate $\Gamma(q) = \frac{1}{\tau(q)}$ and the KWW exponents including their q-dependence [133]. We find in the early phase of the LLPS a linear relationship $\Gamma \propto q$ (Fig. 6.6a) and γ_1 around 1.4-1.7 (Fig. 6.6b) with no pronounced q dependence. In contrast, the dynamics during the late coarsening stage also displays a linear ($\Gamma \propto q$) behaviour (6.6c), however, now with a pronounced q-dependence of the KWW exponents, which are decreasing from values of $\gamma_2 = 2$ at small q-values to $\gamma_2 = 1$

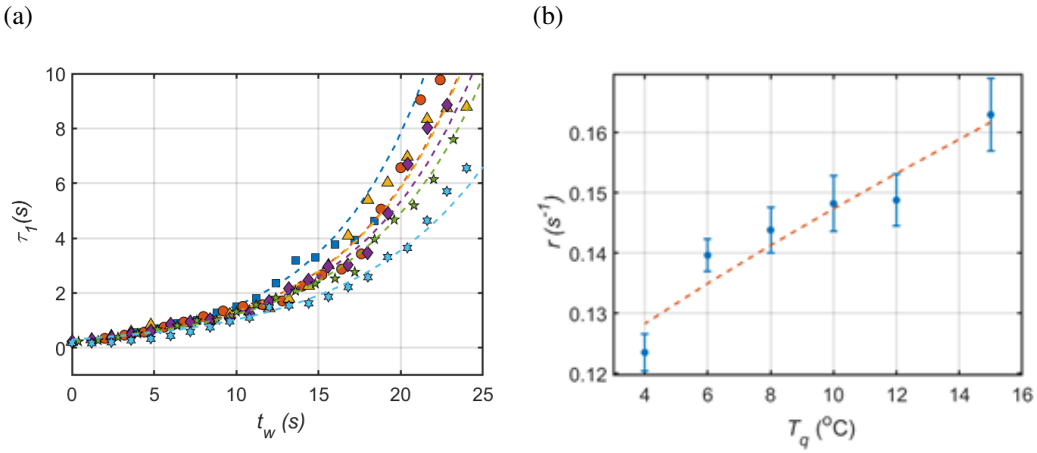

Figure 6.7: a) Decorrelation time of the fast decay at q = 0.005 nm^{-1} as a function of waiting time. Dashed lines are fits using Eq. 6.4, fixing the value of τ_0 to 0.3 and having the rate r as a free parameter. b) Rate r as a function of quench temperature T_q, the red dashed line is a guide for the eye. The symbols are defined in the legend of Fig. 6.1.

at large values of q (Fig. 6.6d). Our results clearly show that the coarsening dynamics of the protein droplets at this length scale are not governed by Brownian dynamics, instead by a ballistic and partially cooperative motion of the protein droplets driven by the spinodal decomposition. Similar super diffusive ballistic types of dynamics have been observed frequently in soft matter systems such as in the late stage of colloidal gelation processes [174; 228; 229], during spinodal decomposition of colloidal systems [121] and also in the framework of MD simulations of metallic glasses [230] with strongly interconnected clusters moving together. Phenomenological models of single micro-collapse events have been put forward as possible explanations [149] underlying such unusual dynamics and subsequently extended to series of such intermittent events to account for both q-dependence of the relaxation rate and the KWW exponents [122; 176]. The connection of these phenomenological models to the dynamics during a LLPS is not obvious, especially with regards to typical field theories, such as the Cahn-Hillard equation (CHE) used to model spinodal decomposition. A shared feature between colloidal gels and the LLPS investigated here, is the presence of elastic deformations. Those can arise in a LLPS from the viscoelastic properties which are caused by a dynamical coupling of diffusion and stresses, and could explain the similarities between these observations [122]. In fact, the dynamical asymmetry of the two phases present in the system can lead to viscoelastic phase separation [39].

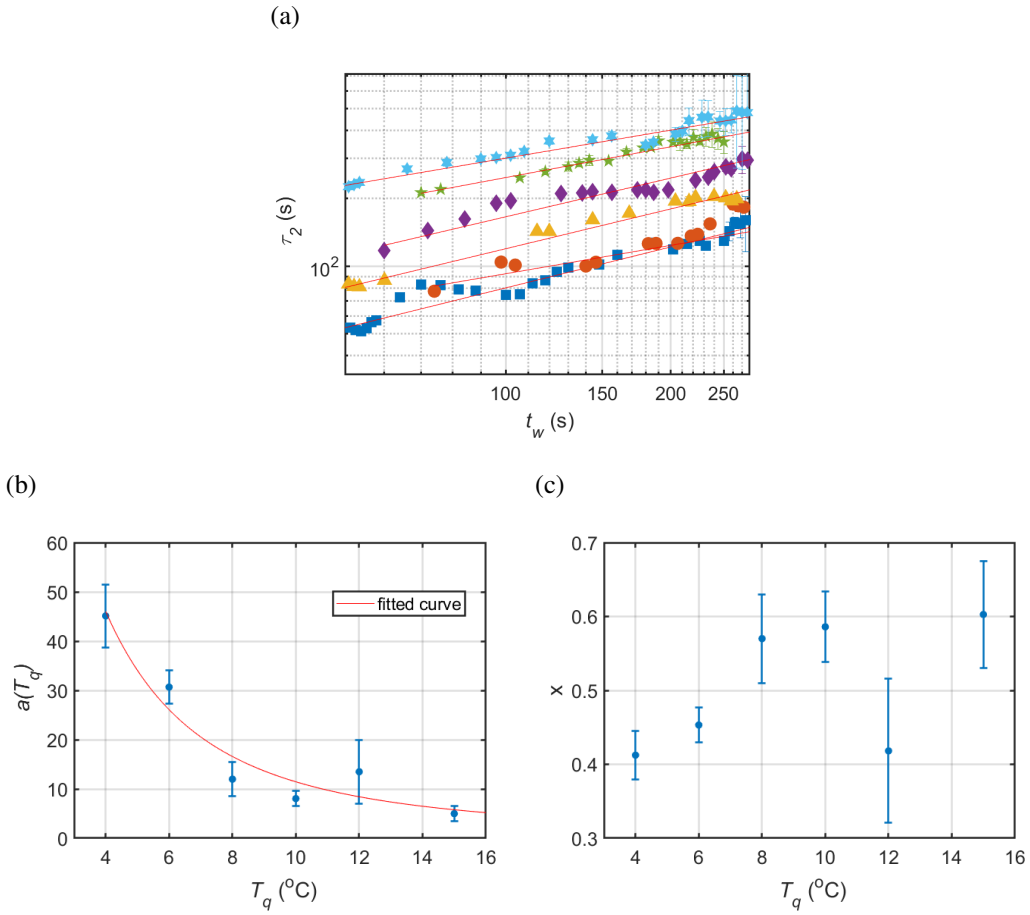

Figure 6.8: a) Decorrelation time of the slow mode as function of t_w for q =0.006 nm^{-1}, solid lines: power law fits according to Eq. 6.5. The symbols are defined in the legend of Fig. 6.1 . b) The prefactor $a(T_q)$, and c) the power law exponent x as a function of T_q. The red line is a guide to the eye

6.2.3 Diffusion in the single phase region

For temperatures above 21 °C the system is in the single phase region, and the solution appears homogeneous and transparent to the eye. In this condition it is possible to perform a dynamic light scattering experiment. Correlation functions $|\mathrm{ISF}(t,q)|^2$ of the solution were collected in a temperature range from 25 °C to 40 °C. As shown in Figure 6.9 the curves show two distinct decays, hence the curves were fitted with a sum of two KWW exponential functions as described by Eq. 6.6.

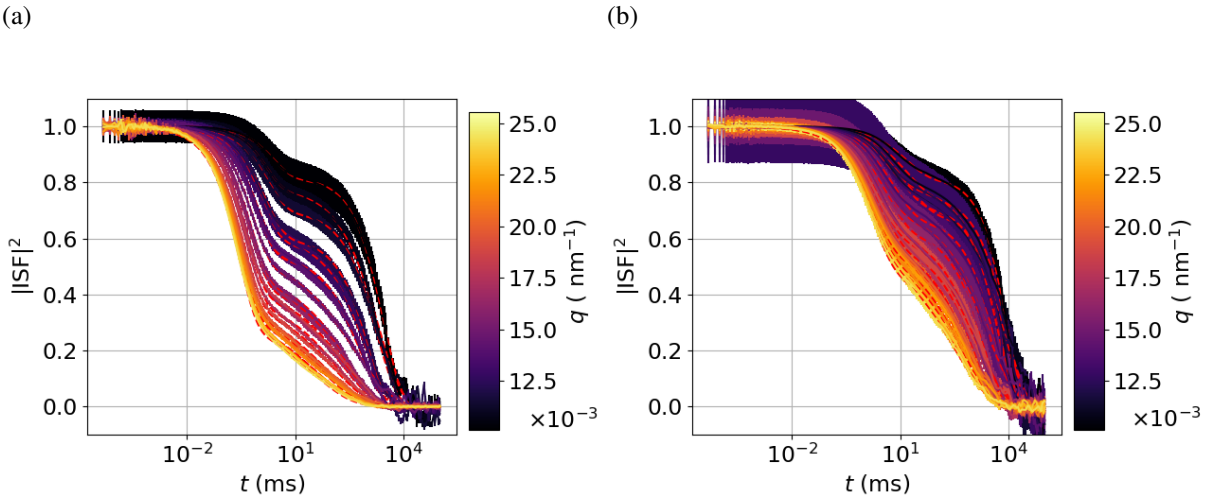

Figure 6.9: Intensity correlation functions $|\mathrm{ISF}|^2$ measured at 40 °C (a) and 25 °C (b) at different q values with the color code indicated by the color bar.

$$|\mathrm{ISF}(t,q)|^2 - 1 = (1-A)\exp\left[-\left(2\frac{t}{\tau_1^{\mathrm{DLS}}}\right)^{\gamma_1^{\mathrm{DLS}}}\right] + A\exp\left[-\left(2\frac{t}{\tau_2^{\mathrm{DLS}}}\right)^{\gamma_2^{\mathrm{DLS}}}\right] \tag{6.6}$$

Given that the solution is stable and no large aggregates are visible, we associate the fast decay to the collective diffusion of the monomers. The decay shows a typical sign of Brownian motion, with $\Gamma_1^{\mathrm{DLS}} \propto q^2$ (Fig. 6.10a). The associated diffusion coefficient D, obtained by fitting $\Gamma_1^{\mathrm{DLS}} = Dq^2$, has a temperature dependency that is not linear. This is to be expected, since from the Stoke-Einstein relation $D = \frac{k_B T}{6\pi\eta(T)R_h}$ and the viscosity $\eta(T)$ depends on the temperature T. The value of γ_1^{DLS} between 0.75 and 0.9, suggest the presence of not only monomers, but also small aggregates. This is not surprising given that part of the proteins (<80%) in the solutions are IgM and IgA, which are usually found in respectively a pentameric and dimeric state.

The slow decay is more difficult to interpret since the solution is far from the dilute limit. For glasses and gel, the correlation functions usually present two decays, where the fast one corresponds to the rattling of the particles in the cage formed by the neighboring particles, and the slow one to the diffusion of the particle outside the cage. In this context the parameter A, i.e. the height of the slow decay, is referred to as non-ergodicity parameter. This quantity is linked to the fraction of particles (A_0) whose motion is localized with an average root-mean-

squared displacement $\Delta R^2(t \to \infty) = r_{loc}^2$, and the localization length r_{loc} in a Debye-Waller-like form as described in Eq. 6.7 [145; 148].

$$A(q) = A_0 \exp\left(-\frac{q^2 r_{loc}^2}{6}\right) \tag{6.7}$$

In Fig. 6.10e $log(A)$ is plotted as a function q^2, so that the slope of a linear fit gives an estimation of the value of r_{loc}. The experimental points depend linearly on q^2 only for a limited q interval, but it is nevertheless possible to see that the absolute value of the slope, and hence r_{loc}, is larger at higher temperature. Thus, at high temperature the cage around the particles is larger. This is consistent with the fact that the system is a UCST, and therefore more attractive at higher temperature. The decorrelation rate of the slow decay dependency on q changes with temperature. It varies from $\Gamma_2^{\mathrm{DLS}} \propto q^3$ at 40°C to $\Gamma_2^{\mathrm{DLS}} \propto q^6$ at 25°C, hence the diffusion is non-Brownian. This is also supported by the value of γ_2^{DLS} which is lower than 1 and strongly q dependent.

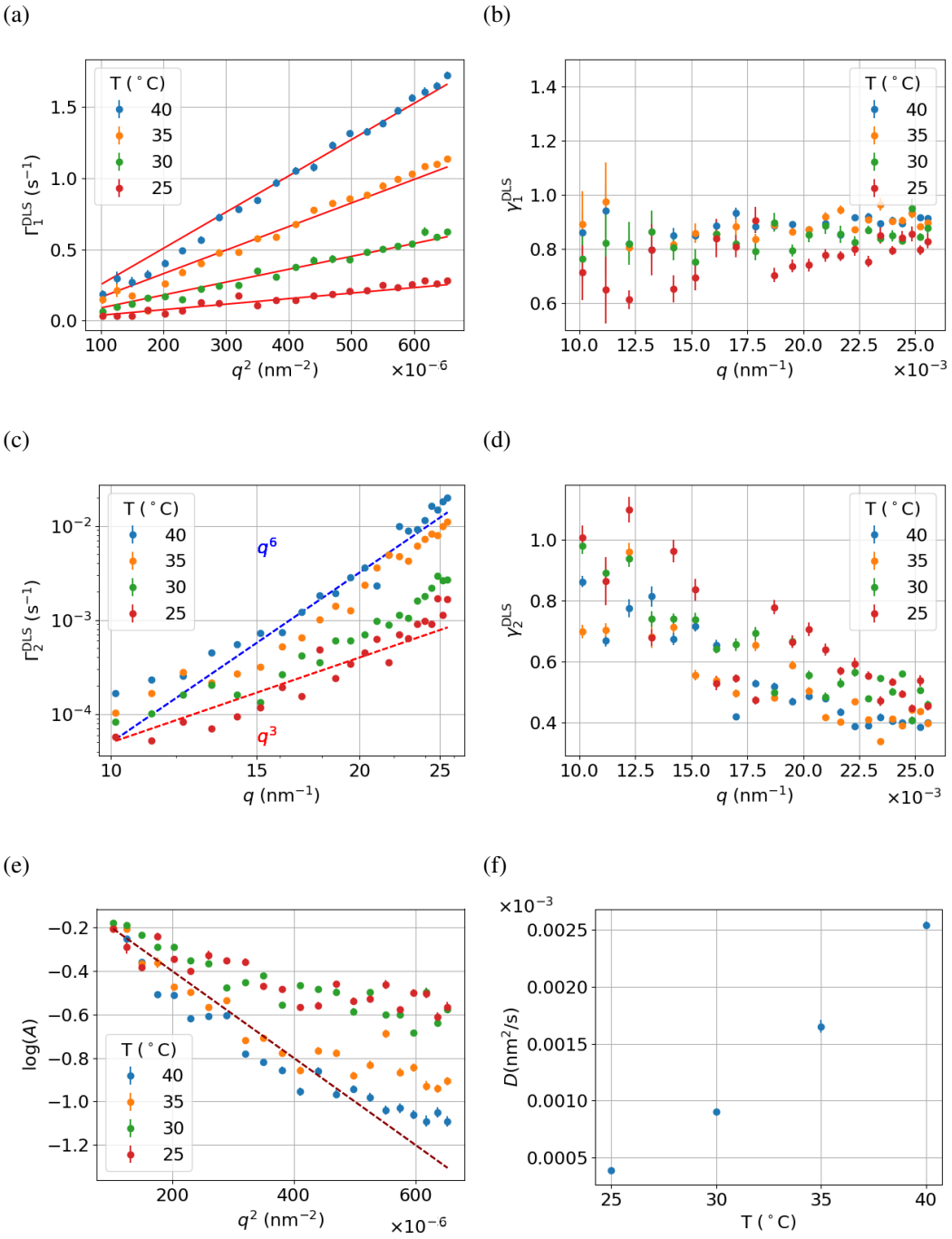

Figure 6.10: a) The fitting parameter Γ_1^{DLS} as a function of q^2, with linear fits represented by the solid red line. b) The exponent γ_1^{DLS} as a function of q. c) Γ_2^{DLS} as a function of q, the blue dashed line shows a proportionality $\Gamma_2^{\mathrm{DLS}} \propto q^6$ and the red one $\Gamma_2^{\mathrm{DLS}} \propto q^4$. d)The exponent γ_1^{DLS} as a function of q. e) The logarithm of height of the slow decay $\log(A)$ as a function of q^2. e) The diffusion coefficient obtained from the linear fit of the decorrelation rate showed in (a).

6.2.4 Simulations

To obtain more insight into the underlying dynamical mechanisms, we compare the experimental data to numerical simulations of the temporal evolution of the CHE [231; 4] (here in 2D). The dynamics of the ordinary CHE shows faster dynamics for quenches to lower temperatures. As this is not what we observe in the experimental data, we introduce a dependence of the mobility μ on protein density $\rho(r,t)$, representing the slowdown of the dynamics when the density of the dense phase is increasing and its mobility freezes out [48], in the spirit of model C according to Ref. [203]. The parameter c_g sets the concentration at which the mobility decreases (for details see Chapter 4). The simulations then yield a time dependent real space configuration $\rho(r,t)$ of the protein density (Fig. 4 (c)) which is converted into an X-ray speckle pattern by means of its Fourier components $|\rho(q,t)|^2$ and analyzed with the same time correlation methods as applied to the experimental data [48; 35].

Fig. 6.11a displays the temporal evolution of the spatially averaged mobility $\bar{\mu}(t_w)$ in the dense phase and Fig. 6.11b the spatially averaged density $\bar{\rho}(t_w)$ of both dense and dilute phases for different values of c_g. A point in the 2D image was considered part of the dense phase if its concentration was higher than the initial concentration. The mobility of the dense phase drops quickly during the LLPS upon lowering the c_g value. The density in both dense and dilute phase do not reach their equilibrium values anymore, which is considered an arrest of the LLPS [48; 35].

Typical real space configurations are shown in Fig. 6.11c with the LLPS visible via the formation of domains of the diluted phase (blue) in a host matrix of the dense phase (red). The corresponding density profiles (see Fig. 6.12 a and b) show the typical hallmarks of the spinodal decomposition with density fluctuations developing quickly and reaching rather smooth profiles at the end of the LLPS for a mobility that is independent of protein density and equal to 1. In contrast, for $c_g = 0.6$ we observe that the density fluctuations become immobile when reaching the threshold value, leading to smaller domains.

Comparing Fig. 6.12 c and d with Fig. 6.1 b and c one can appreciate that the kinetics of the phase separation obtained with simulation reproduces the results obtained with the experiments, except for right after the quench. In the experiment, in fact, the peak shifts in position from its appearance, which was already observed in visco-elastic phase transitions [31].

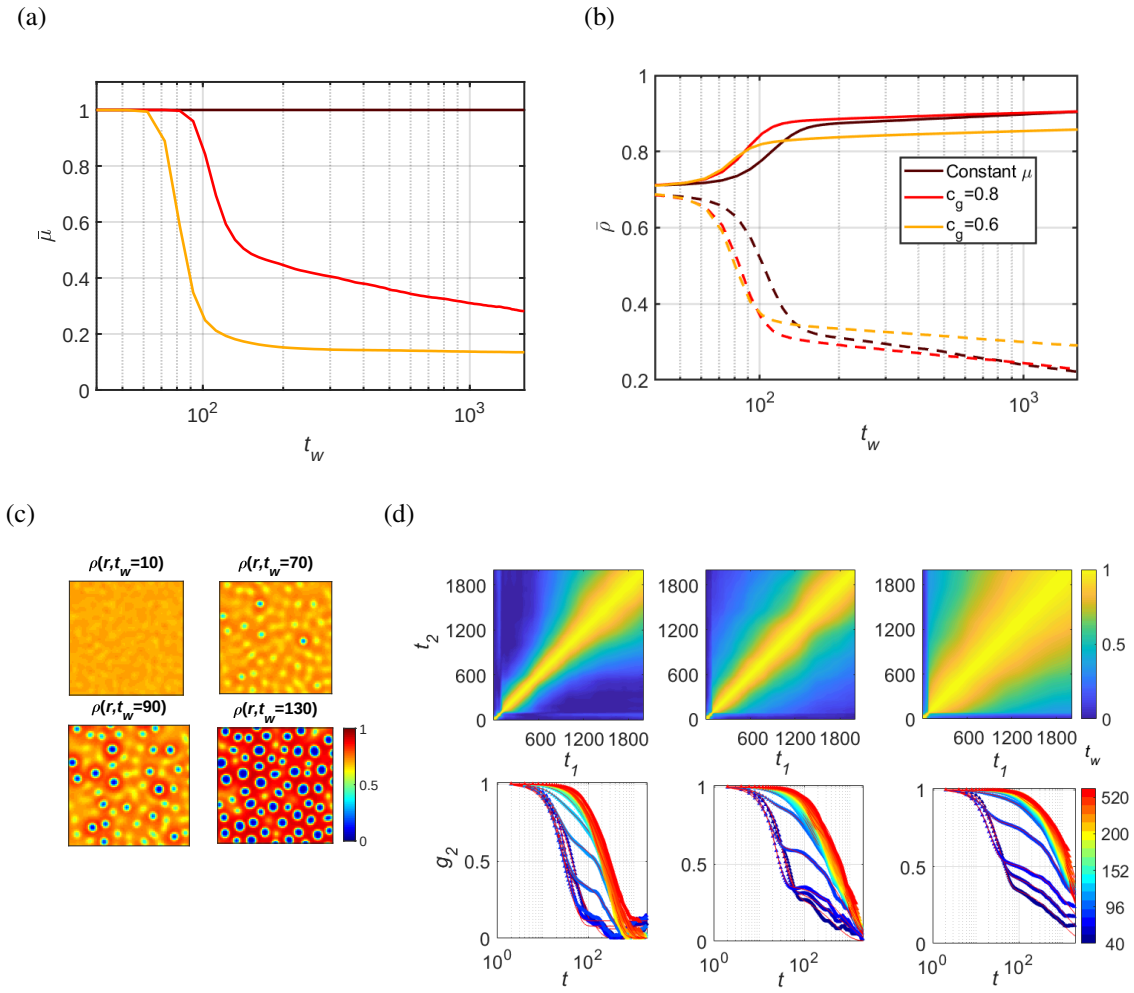

Figure 6.11: a) The simulated $\bar{\mu}$ and b)$\bar{\rho}(t_w)$ of the dense phase as a function of waiting time. In brown the case with constant mobility and the quench depth for this case was set to $T_q = 0.2T_c$, with T_c being the critical temperature [232; 8], in red $c_g = 0.8$ and $T_q = 0.12T_c$ and in yellow $c_g = 0.6$ and $T_q = 0.08T_c$. (c) Examples of real space configurations for T_q =0.14 T_c and mobility at different waiting times with the densities indicated by the colour bar. (d) Upper panels: two-time correlation function of the simulated data for q =1. From left to right the parameters T_q and c_g of the simulations are: T_q =0.2 and $c_g = \infty$, which correspond to a constant mobility set to 1,T_q =0.12 and c_g =0.8, and T_q =0.08 and c_g =0.6 . Lower panel: corresponding g_2 functions at different waiting times t_w.

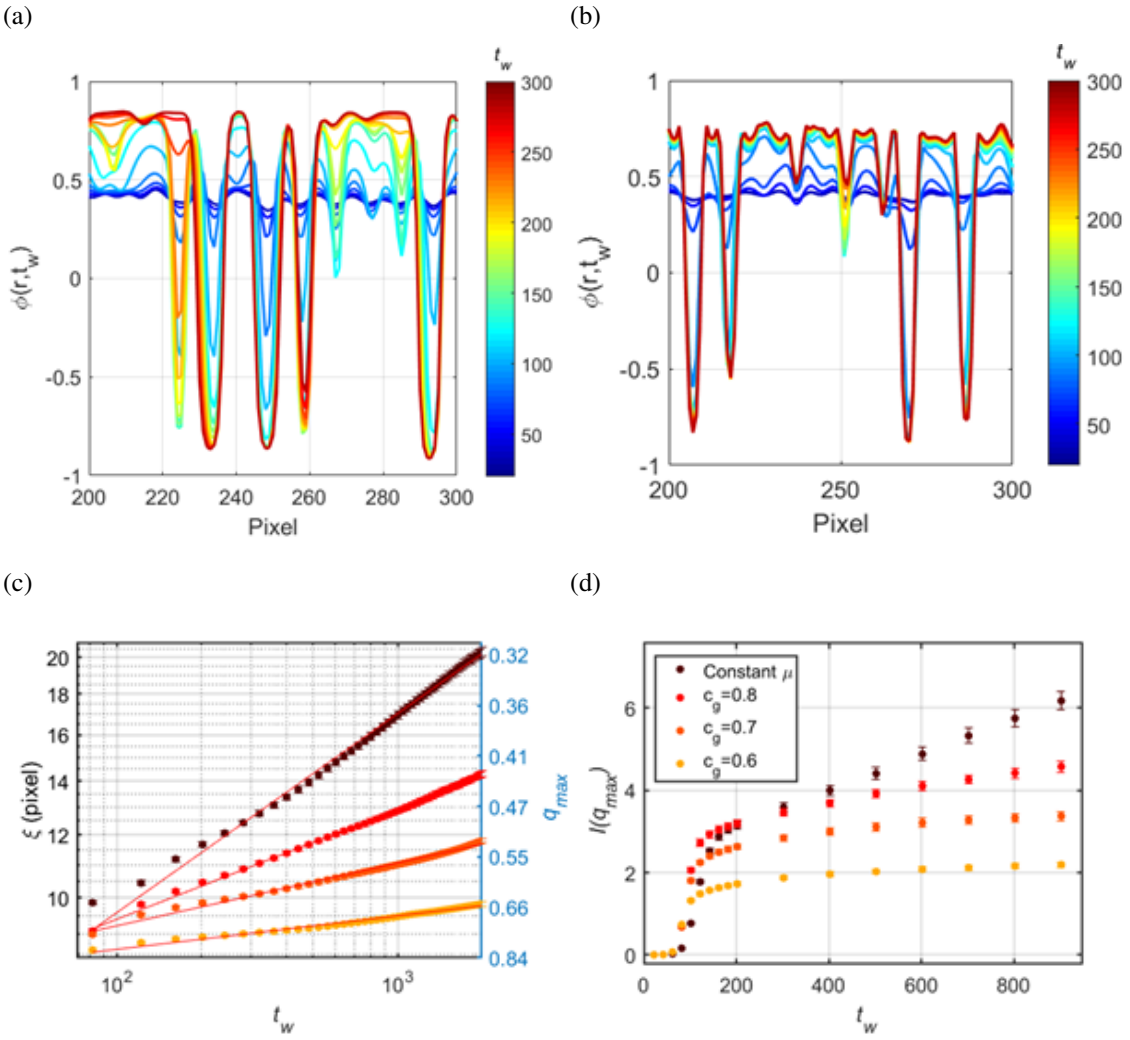

Figure 6.12: a) The concentration development in real space for different t_w for a spinodal decomposition with constant mobility and b) for a spinodal which was arrested because of a gel transition (c_g =0.6). c) The peak position as a function of waiting time with a power law fit (red lines) and d) the value of the intensity at the peak position.

TTC and g_2 functions were computed following the procedure of experimental data. Fig. 6.11d displays the TTC for the simulations and the corresponding g_2 functions. We identify a fast dynamic process during the early time of the LLPS, which represents the dynamics of spinodal interface formation between dense and dilute phase. The dynamics quickly slows down with a sudden appearance of a second much slower relaxation process when the dense phase has formed. The relaxation times during the first stage are determined by the quench depth (smaller for deeper quenches) because the curvature of the free energy is here the main driving force for the velocity of interface formation. The corresponding KWW values γ_1 and γ_2 (Fig. 6.13c and 6.13d) are between 1.5 and 2.5 in good agreement with our experimental values.

The dependency of the decorrelation rate with q is not trivial (Fig. 6.13). To understand the possible causes of this behavior an effective diffusion can be calculated from the linearized CHE since it is analytically solvable:

$$D_{eff}(q) = \frac{1}{2q^2}\frac{d(\log(S(q;t))}{dt} \tag{6.8}$$

This equation is correct in the limit of the approximation of the linearization; hence it is not directly applicable here but can nevertheless show how the q dependence is strongly connected to the structure factor and its time evolution. Upon closer inspection, we can see that the local minima in decorrelation rate are in the same q position corresponding to the maxima in the intensity (Fig. 6.13e and 6.13f), which can be explain by equation 6.8.

6.2.5 Comparison experimental and simulated results

Comparing the real space data and the parameters describing the dynamics it is possible to see that the rise of the non-ergodicity parameter starts during the onset of domain and coarsening dynamics. In this short transition time (see Fig. 6.5) domain coarsening is progressing in parallel with the final interface formation. After this transition the domain coarsening is taking place. The dynamics seems to be composed of three processes: coalescence of different domains, domain growth and the spatial movement which is guided by the surface tension and precedes the coalescence of two domains. Its decorrelation time is larger for deeper quenches because of the lower transition concentration of the mobility (Fig. 6.11d and 6.13), representing a situation in which the temperature-dependent glass line of the dense host phase intersects the spinodal phase region. For the lower value of c_g, the diluted phase is essentially trapped

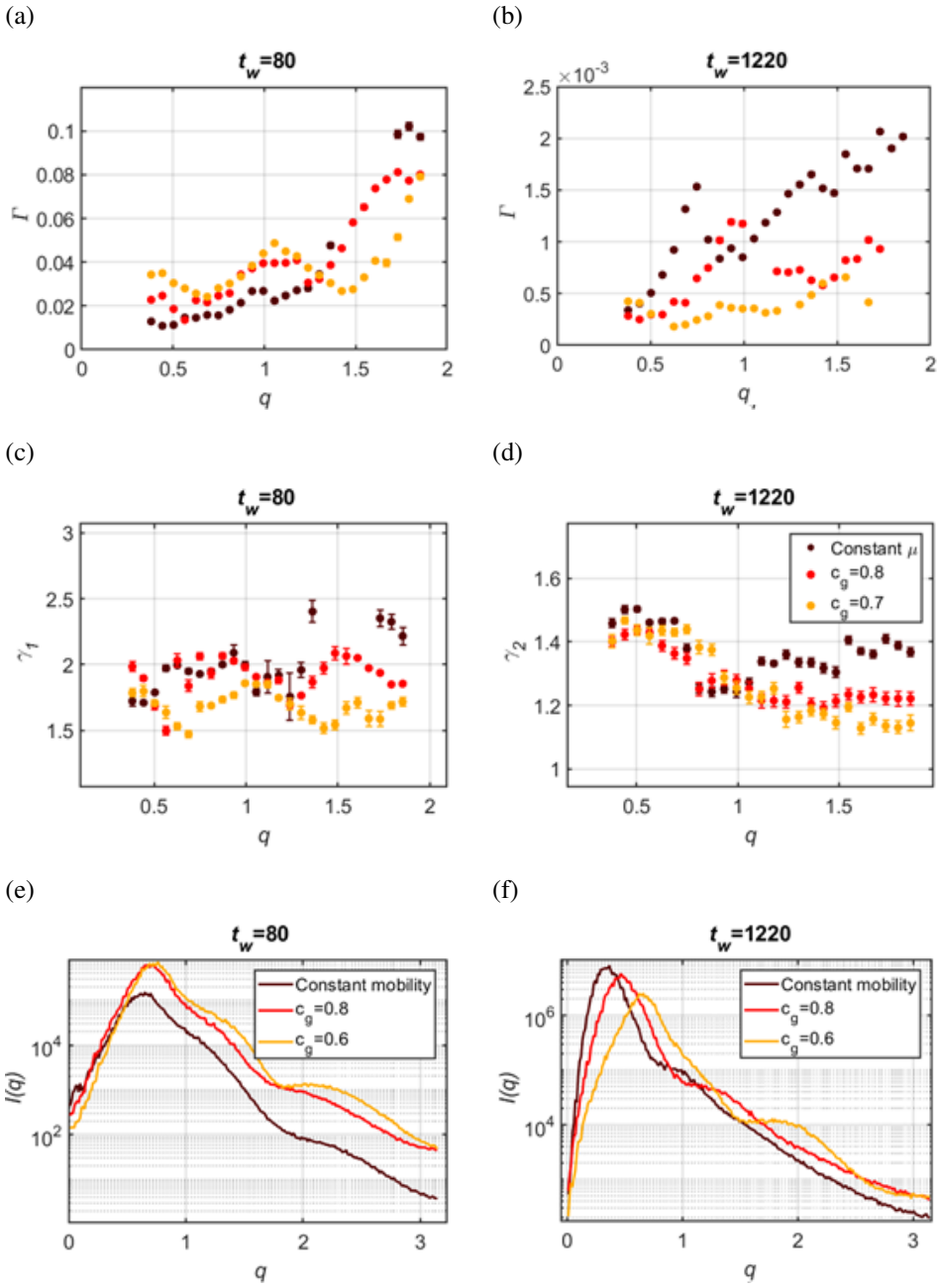

Figure 6.13: a) The decorrelation time of the fast mode at waiting time $t_w = 80$ and b) the slow mode at $t_w = 1220$ as a function of q. c) The value of the KWW exponents as a function of scattering vector for the fast and c) the slow mode. e) The simulated intensity is shown as a function of scattering vector at $t_w = 80$ and (f) at $t_w = 1220$.

inside the frozen host matrix (red in Fig. 6.11c).

Based on the simulation results, we can conclude that the kinetics of the systems is captured by model C as suggested before [203]. The dynamics, however, is only partially reproduced: the slowdown of the late stage dynamics with increasing quench depth is correctly described as well as the presence of two relaxation modes. Model C does not reproduce the $\Gamma \propto q$ behaviour observed in the experiment and the q-dependence of the KWW values of the slow dynamics (Fig. 6.13). We speculate that this is due to the negligence of the viscoelastic properties of the system in the CHE, which would lead to elastic deformation and motion inducing a linear dispersion relation.

6.3 Conclusions

We demonstrated the technique of low radiation dose XPCS and used it to study protein dynamics during a LLPS. The method delivers simultaneously information on both collective dynamics via XPCS and structural evolution via the ensemble averaged scattering $I(q)$. The two-time correlation maps provide a high level of detail of the dynamics during a spinodal decomposition of Ig in solution with PEG. We identify distinctly different dynamical regimes of the LLPS with different temperature behaviour. The early stage dynamics is reflecting concentration fluctuation and interface formation and is faster for lower temperatures reflecting stronger quench depths. In contrast, the later stage of coarsening is slower for lower temperatures caused by the reduced mobility of the slowed down proteins comprising the host matrix. With simulations we are able to identify a concentration and time dependence of the molecular-scale mobility which connects the dynamics of the condensates to molecular-scale quantities.

Chapter 7

Individual proteins and intra-protein short time diffusion

This section is based on Ref. [233].
Antibody therapies are typically based on high-concentration formulations that need to be administered subcutaneously. These conditions induce several challenges, inter-alia a viscosity suitable for injection, sufficient solution stability, and preservation of molecular function. To obtain systematic insight into the molecular factors, we study the dynamics on the molecular level under strongly varying solution conditions. In particular, we use solutions of antibodies with PEG, in which simple cooling from room temperature to freezer temperatures induces a transition from a well-dispersed solution into a phase-separated and macroscopically arrested system. Using quasi-elastic neutron scattering during *in situ* cooling ramps as well as in pre-thermalized measurements, we observe a strong decrease of antibody diffusion, while internal flexibility persists to a significant degree, thus ensuring the movement necessary for the preservation of molecular function. These results are relevant for a more dynamic understanding of antibodies in high-concentration formulations, which affects the formation of transient clusters governing the solution viscosity.

7.1 Introduction

In this study, we focused on probing the single protein and the intra-molecular diffusion was under focus. To do so, we employed two types of neutron spectrometers, probing quasi-elastic scattering on length scales from the protein size down to the protein side chain distances and on time scales from several tens of picoseconds to hundreds of nanoseconds. We probe the

effects of temperature quenches into the LLPS region on antibody diffusion as well as domain and internal dynamics of the antibodies.

Proteins perform a complex set of motions on nanoscopic time and length scales [68]. The entire protein molecule diffuses in the cage of the neighboring molecules on short time scales, both with translational and rotational displacements. For Y-shaped antibodies, the domain dynamics, i.e. the relative motions of the lobes, present a second significant motif. Finally, both the protein backbone and the side-chains exhibit locally confined dynamics.

Employing both NBS and NSE with their different characteristics, we aim to obtain information on these three hierarchical levels of dynamics. While a complete decoupling into individual contributions is impossible, we focus on trends with lowering temperature. In particular, NSE mainly measures collective dynamics, at q values corresponding to length scales of nearest neighbors. These scales thus focus on the diffusion of the entire molecule, i.e. translational and rotational diffusion, with potentially some contributions from domain dynamics. The larger q values probed by NBS allow to also address local motions, and monitors the translational and rotational self-diffusion of lobes as well as of the entire protein, depending on the conditions.

7.2 Results and Discussion

7.2.1 Structural properties and kinetics of phase separation

To understand the diffusion properties of the sample (Sample B of Table 2.1) it is important to evaluate also their structural arrangement, and particularly for this system in which state of the phase separation the sample is. For this reason the sample was measured with small angle neutron scattering and very small angle neutron scattering at the beamlines KWS 2 and KWS 3 at the Forschungs-Neutronenquelle Heinz Maier-Leibnitz (FRM II) in Garching, Germany. The system was measured at two ranges of the scattering vector ($q = \frac{4\pi}{\lambda}\sin(\theta)$ with 2θ the scattering angle), the first one corresponding to the protein size (Fig. 7.2 from 0.01 Å^{-1} to 50 Å^{-1}) and the second one corresponding to the domain size (Fig. 7.1 from 0.0002 Å^{-1} to 0.002 Å^{-1}).

In a q range corresponding to the size of the domains the sample was monitored right after the temperature quench by performing consecutive measurements of 1 min exposure each. At 18 °C the intensity changes for the whole measurement time (for a total of more than 30 min), while at 6 °C, instead, a peak forms in the first several minutes, grows until roughly 10

min, after which the growth is strongly reduced (Fig. 7.1). Importantly, at 18 °C the intensity does not show a clear spinodal peak due to the limited time resolution of 1 min, in which the intensity is changing giving as a result the very broad peak visible in Fig. 7.1b. Since at 6 °C the intensity change is much slower this effect is less pronounced, having as a result a much more defined peak.

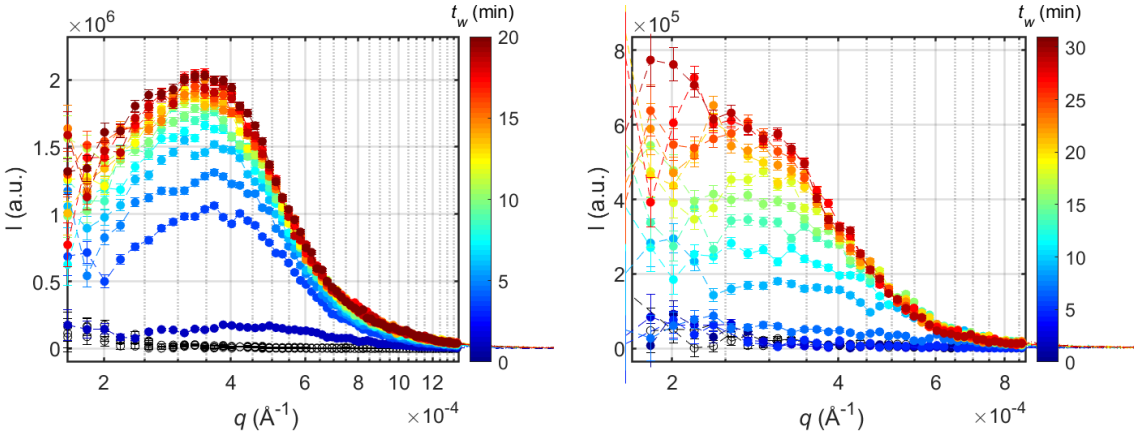

Figure 7.1: VSANS curves measured right after the temperature quench from 37 °C to 6 °C (a) and to 18 °C (b). The color corresponds to the waiting time t_w after quench and indicated by the color bar.

Fig. 7.2 shows SANS profiles at 37 °C, 18 °C and 6 °C. To understand when the structure factor plays a role, the intensity was normalised by the intensity at 37 °C. The structure factor in the single-phase is supposed to be very different from the one in the phase separation region, hence if the normalised intensity is constant at 1, this indicates that the q range considered is dominated by the form factor and the structure factor is constant at 1. This is the case for q values larger than 0.14 $Å^{-1}$.

7.2.2 Dynamic structure factor from NBS

The analysis performed follows the procedure established in literature [220]. The signal is a sum of different contributions, namely the diffusion of the water molecules, the PEG polymers and the antibodies. The latter is divided in two contributions: one corresponds to the apparent global diffusion of the protein, and the second one to the internal diffusion, as validated in a previous study on the pure antibody solution without PEG [99], where the global diffusion corresponds to the rotation and translation of a single antibody, while the internal diffusion

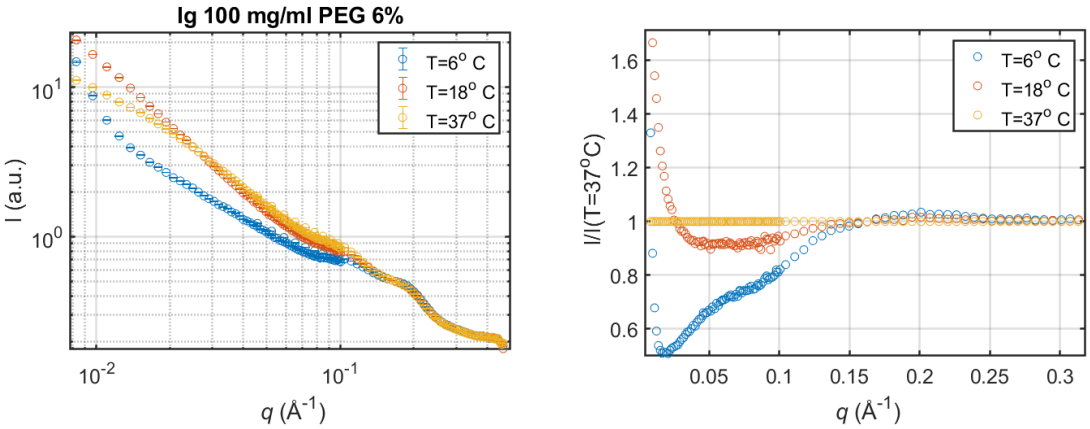

Figure 7.2: a) SANS curves measured after equilibration at the temperatures indicated in the legend. b) SANS intensity at 18 °C and 6 °C normalised by the intensity at 37 °C.

corresponds to the movement of the hydrogen atoms in the peptide chain. At temperatures below 21 °C the sample present two phases, but only the dense phase contributes significantly to the signal, hence it is not necessary to add further contributions. To quantify more quantitatively the contribution of the dense and dilute phases to the overall signal of the structure factor measured at IN16b, the single phases formed at 6°C were measured. The experimental procedure to obtain this single phases can be found below. The corresponding dynamics structure factor curves are shown in Figure 7.3a. Choosing appropriate weighting factors, the weighted sum of the two signals, $S_{sum} = 0.7S_{dense} + 0.3S_{dilute}$, overlaps with the signal of the sample investigated in this work at 6 °C, which gives us a rough estimate of the percentage of dense and dilute phase in the sample.

This implies that the estimated volume of the dense phase correspond to 70% of the overall volume. Given that the concentration estimation of 270 mg/ml in the dense phase and 30 mg/ml in the dilute phase [31], the molecules in the dilute phase constitute only roughly 5% of the molecules in solution. It is, hence justified to consider the dense phase the main contributor to the overall signal and not include further contributions.

Each contribution corresponds to a Lorentzian function $L_\Omega(\omega)$ with width Ω. Therefore, the dynamic structure factor is modelled by

(a) (b)

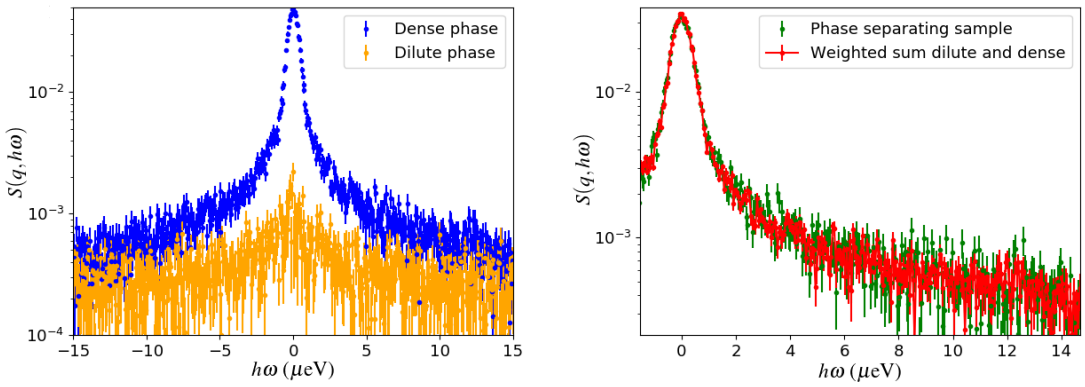

Figure 7.3: a) The structure factor from the dilute and dense phase at 6 °C at $q = 1.2\text{Å}^{-1}$. b) The weighted sum ($S_{sum} = 0.7S_{dense} + 0.3S_{dilute}$) of the two signals shown in (a), and their parent solution after a quench to 6 °C.

$$
\begin{aligned}
S(q,\omega) &= R(\omega) \otimes \{ \\
&\{\beta \left[A_0(q) L_{\Omega_{\text{global}}}(\omega) + (1 - A_0(q)) L_{\Omega_{\text{int}}+\Omega_{\text{global}}}(\omega) \right] \\
&+ B L_{\Omega_{\text{PEG}}}(\omega) + C(q) L_{\Omega_{\text{water}}}(\omega) \}
\end{aligned}
\tag{7.1}
$$

where Ω_{global}, Ω_{internal}, Ω_{PEG} and Ω_{water} provide information on relaxation rates of the corresponding component. The so-called Elastic Incoherent Structure Factor (EISF) $A_0(q)$ characterizes the confined geometry of local internal motions, and B and $C(q)$ denote amplitudes of PEG and water contributions (see for details below).

The term $R(\omega)$ represents the resolution function of the instrument, which can be described by a Gaussian function. The measured signal is the convolution ($\otimes$) of the sample signal and the resolution function. $R(\omega)$ was fitted from the signal of a measurement of Vanadium [234].

Fits of the curves $S(q,h\omega)$ at fixed q were performed showing Fickian diffusion for the apparent global diffusion and the diffusion of PEG, and jump diffusion for the internal dynamics of the protein. While it is possible to see that the trend of the points is following the said type of dynamics, the fit is unstable due to the high number of parameters, especially for small q values. For this reason a global fit was performed.

To increase the stability and robustness of the fit, and to include prior knowledge on the

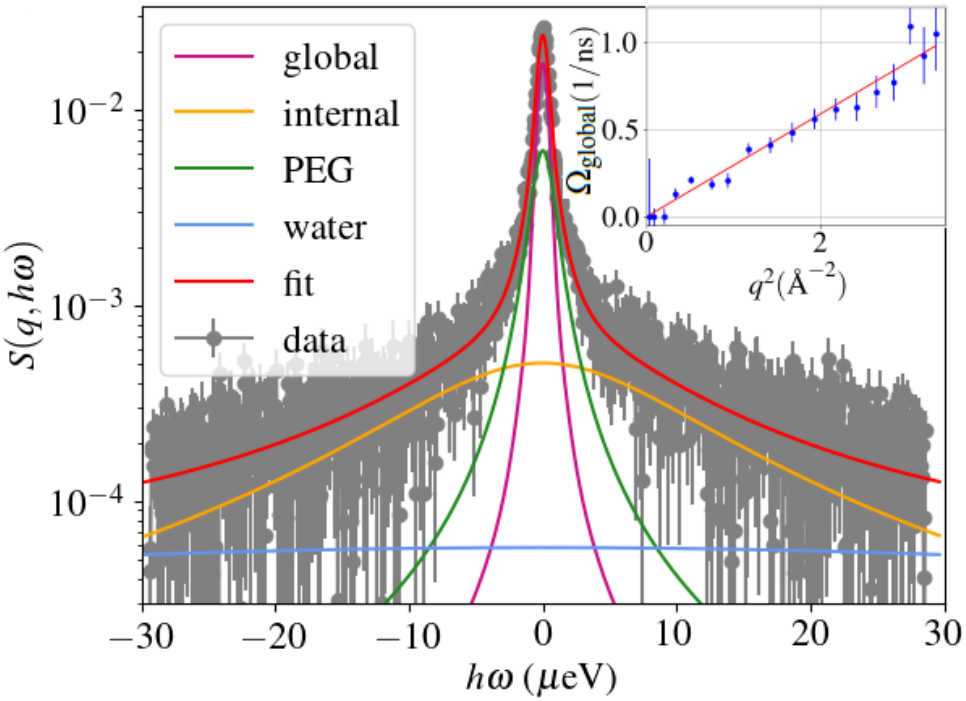

Figure 7.4: An example of the fitted backscattering data with the 4 contributions indicated in the legend. The inset shows the q^2 dependency of the width of the Lorentzian of the global diffusion.

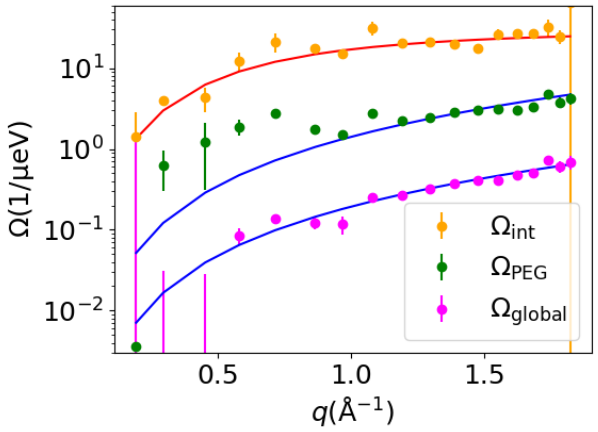

Figure 7.5: The decorrelation times extracted from the q-wise fit. The blue solid line correspond to a fit of a fickian diffusion, and the red one to a jump diffusion type of fit.

system, the q dependency of the Lorentzian functions was fixed. The global diffusion and the diffusion of PEG was set to Fickian diffusion (i.e. $\Omega_{\text{global}}(q) = D_{\text{global}}q^2$ and $\Omega_{\text{PEG}}(q) = D_{\text{PEG}}q^2$), and the internal diffusion was modelled with the jump diffusion signature $\Omega_{\text{int}}(q) = \frac{D_{\text{int}}q^2}{1+q^2D_{\text{int}}\tau}$ [220]. This assumption was validated by the trends obtained from q-wise fits (Fig. 7.4 and Fig. 7.5).

Because of the limited ω range measured, the values of the widths of the Lorentzian function of the water were not fitted, instead tabulated values were used [234]. A pure D_2O solution was measured to estimate the amplitude $C(q)$ of the Lorentzian function of water. $C(q)$ was calculated by taking into account the reduction of volume fraction of water (0.7) due to the presence of protein and polymer. B was fitted assuming no q-dependence to increase the stability of the fit. The value of $A_0(q)$ was fitted without any prior assumption on the q dependence.

The diffusion coefficient and the residence time of the internal dynamics, and the diffusion coefficient of PEG obtained from the fitting are shown in Fig. 7.6. The temperature dependence is not trivial and is deviating from a simple Stoke-Einstein dependence.

7.2.2.1 Elastic incoherent structure factor

$A_0(q)$ corresponds to the so-called Elastic Incoherent Structure Factor (EISF), and, assuming a localized movement in a radial harmonic potential, it can be described with a Gaussian profile in a basic model (Eq. 7.2) [235].

$$A_0(q) = f\exp(-q^2\Lambda^2) + p \tag{7.2}$$

where Λ denotes the length of the localized motion, p the fraction of immobile hydrogen atoms, and f is proportional to the fraction of hydrogen atoms which perform the confined motion.

7.2.2.2 Elastic fixed-window scans of neutron backscattering

The system was monitored during the temperature quench with a so-called elastic Fixed Window Scan (FWS) which fixes the energy transfer to $h\omega = 0$ μeV, and thus allow monitoring of the dynamical evolution with a higher sampling frequency. In this way the acquisition time was reduced to 10 s. From the intensity at zero energy transfer it is possible to obtain information about the apparent mean squared displacement $\langle u^2 \rangle$ via the quadratic function

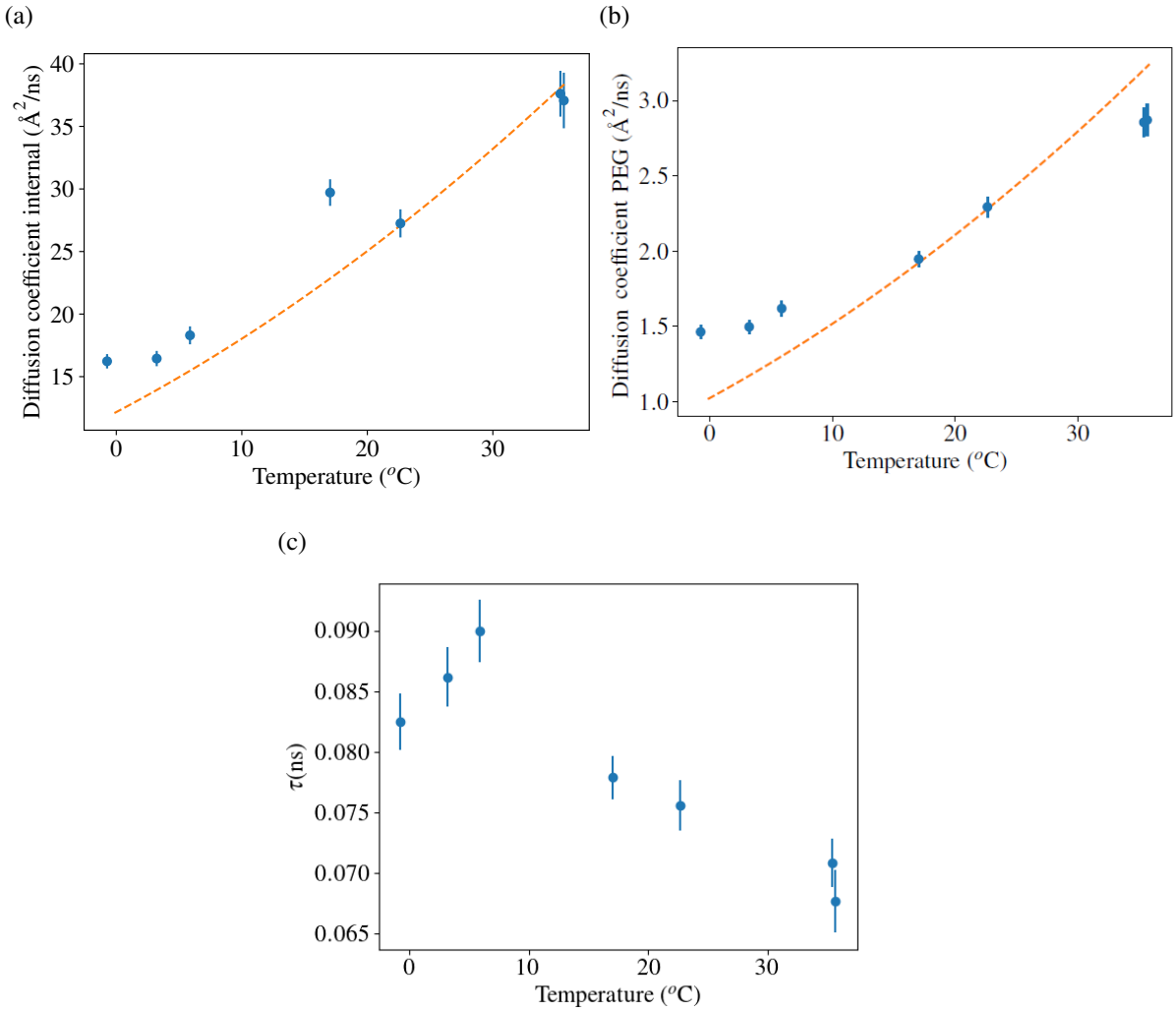

Figure 7.6: Diffusion coefficients of the internal dynamics of the protein (a) and the diffusion coefficient of the polymer (b) as a function of temperature. The dashed line shows the temperature dependence that is expected from the Stokes-Einstein equation, i.e. $D \propto \frac{T}{\eta(T)}$. c) The residence time τ of the jump diffusion as a function of temperature.

$$\log(S(q,\omega=0)) = I_0 - \frac{1}{3}q^2\langle u^2\rangle + bq^4, \tag{7.3}$$

where b is an additional scalar fit parameter [236]. Typical curves with quadratic fits collected during a quench from 37°C to 1°C are shown in Fig. 7.7.

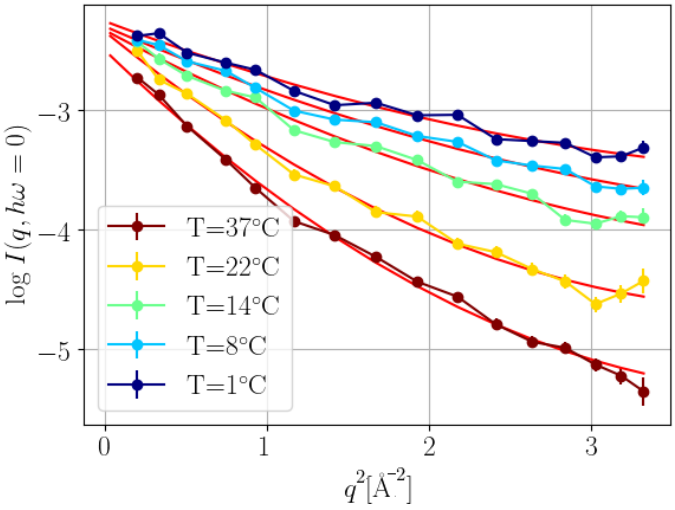

Figure 7.7: The intensity of the fixed window scan as a function of scattering vector. The respective fits (Eq. 7.3) are plotted in red.

7.2.3 Intermediate scattering function from NSE

From the intermediate scattering function (ISF) $I(q,t)$ as the measurement observable, a diffusion coefficient can be determined to evaluate the mobility of the particles in the system. The ISF cannot be fitted by a single exponential decay, as was already seen for the pure antibody solution [101; 100]. The complex composition of the solution and the limited time resolution of the measurement do not allow for a robust fit and a meaningful analysis of all possible decays. Thus, to extract robust characteristics of the dynamics, we used a stretched exponential decay, also called Kohlrausch–Williams–Watts (KWW) function [223]

$$I(q,t) = \exp(-(t/\tau)^{\gamma}). \tag{7.4}$$

To avoid any coupling between the decorrelation time τ and the exponent γ, γ was fixed to a value of 0.5, which was in the range of preliminary free fits.

The physical interpretation of a stretched exponential involves a distribution of decay processes, with the average decorrelation time $\langle\tau\rangle = \frac{\tau}{\gamma}\Gamma(\frac{1}{\gamma})$ [237], with $\Gamma(x)$ the gamma function. The diffusion coefficient was calculated as $D_{\mathrm{NSE}} = \frac{1}{\langle\tau\rangle q^2}$.

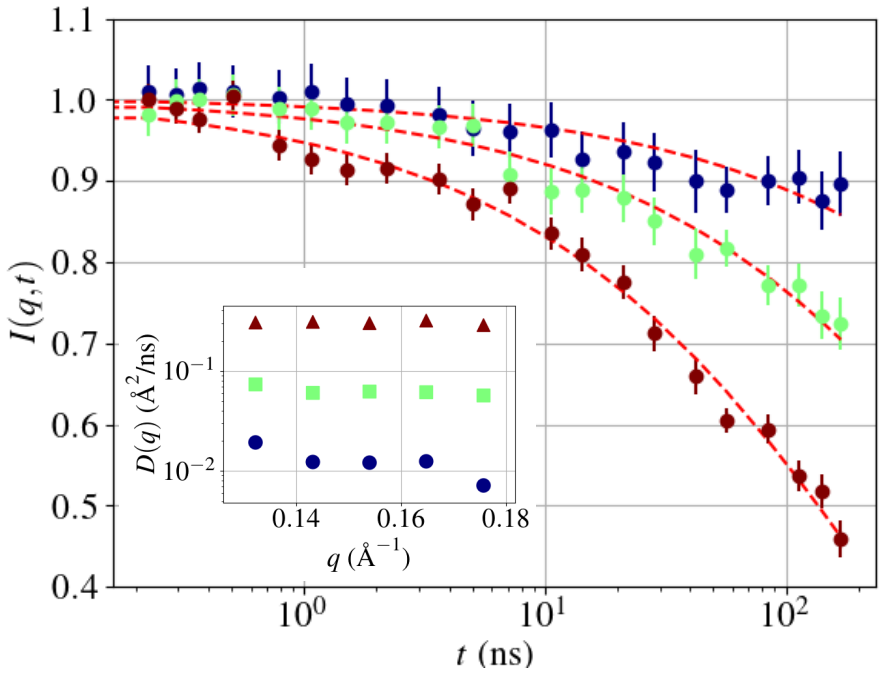

Figure 7.8: Intermediate scattering function at q=0.154 Å^{-1} measured at 6 °C (blue), 18 °C (green) and 37 °C (red). In the inset, the diffusion coefficient calculated with $D_{\mathrm{NSE}} = \frac{1}{\langle\tau\rangle q^2}$ as a function of scattering vector is shown. We remark that 1 Å^2/ns corresponds to 10^{-7} cm^2/s.

7.2.4 Significant reduction of diffusive motions upon cooling into the phase-separated regime

From the NSE data, an effective diffusion coefficient was calculated for the different measured temperatures and q values, see inset of Fig. 7.8. Given the almost flat signature as a function of q, we averaged the diffusion coefficients at each temperature. The average value of D changes drastically in the temperature range measured, with a decrease factor of about 30 (blue circles in Fig. 7.9b). Thus, the relative movements of proteins on the nearest-neighbor scale are strongly reduced, which can be intuitively understood by the proximity of other Y-shaped protein molecules.

To understand when the proximity of other proteins plays a role, we calculated the protein overlap concentration c_{overlap} at which the protein lobes start to reach into another protein. To do so, we have to understand at which concentration the average distance between two proteins is equal to their outer radius, for all the concentrations above this value the lobes of

two proteins can closely interact. We used $R_{outer} = 7.7$ nm as value of outer radius, which is the distance between the center of the protein and the most distant point on a lobe of the antibody, averaged over the three lobes that constitute an antibody. We based our calculation on the Protein Data Bank (PDB) structure 1HZH, which was used in the past to describe γ-globulin [31]. If we assume a random close packing of the particles, hence a volume fraction of ϕ_{cp}=0.64, the number density of the proteins is given by $n = \frac{\phi_{cp}}{V_p}$, with $V_p = \frac{4}{3}\pi R^3_{\text{outer}}$. The protein overlap concentration is then given by:

$$c_{\text{overlap}} = \frac{n}{N_a M_w} = \frac{\phi_{cp}}{\frac{4}{3}\pi R^3_{outer} N_a M_w} \approx 90\,\text{mg/ml} \tag{7.5}$$

Considering that the protein concentration of the parent solution is 100 mg/ml, the concentration of the investigated sample is well above c_{overlap} even in the one-phase region, hence the proteins' outer radius is overlapping at higher concentrations, as represented in the sketch in the right hand-side inset of Fig. 7.9a.

For low temperatures, where the system consists of two phases, the concentration of the dense phase is much higher than c_{overlap}, and at this point the proximity of other Y-shaped molecules might extensively slow down the motion of the entire antibody, even if the movement of the lobes could be still present. This observation is consistent with the kinetic slowdown of the phase transition observed on macroscopic length scales, where the growth of domain size decreases until almost ceasing (Fig. 2 of the supplementary material) [45; 53; 110; 202], for which a strong difference in the mobility of dense and dilute phase is expected.

For the same temperature range and sample conditions, the self-diffusion coefficient obtained from the NBS data shows a less severe decrease by a factor of around 5 (red squares in Fig. 7.9a). In the one-phase region (green shaded area), the diffusion coefficient is proportional to the temperature divided by the viscosity of D_2O, as expected from the Stokes-Einstein equation. Once the phase separation region is reached, a stronger decrease of the diffusion coefficient becomes visible.

The same decrease is observed for the apparent Mean-Squared Displacement (MSD) $\langle u^2 \rangle$ from the Fixed Window Scan (FWS) analysis as a measure of atomic displacements on the time scales of few nanoseconds (Fig. 7.9a). Importantly, as these results are recorded during the cooling ramp, we obtain a more continuous profile, which clearly changes from the higher-temperature trend once phase separation sets in. It is interesting to note that the Mean-Squared Displacement (MSD) and the equilibrium global diffusion coefficient show a similar behavior as function of temperature, indicating that the system is not aging strongly, as it would be

expected in gel and glass phases.

Combining the three data sets from NSE, pre-thermalized NBS, and FWS-NBS during cooling, we observe significant changes of the diffusive dynamics upon entering in the phase-separated regime. Intuitively, this effect can be understood due to the crowded environment in the dense phase after LLPS. In fact, the signal measured is dominated by the signal of the dense phase, hence effectively, measuring the sample below the phase transition temperature is equivalent to measure a sample with higher concentration of proteins.

(a)

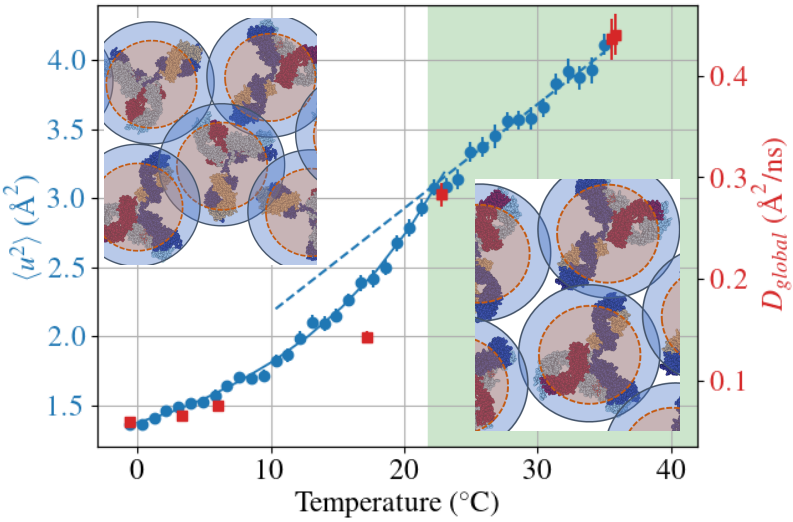

(b)

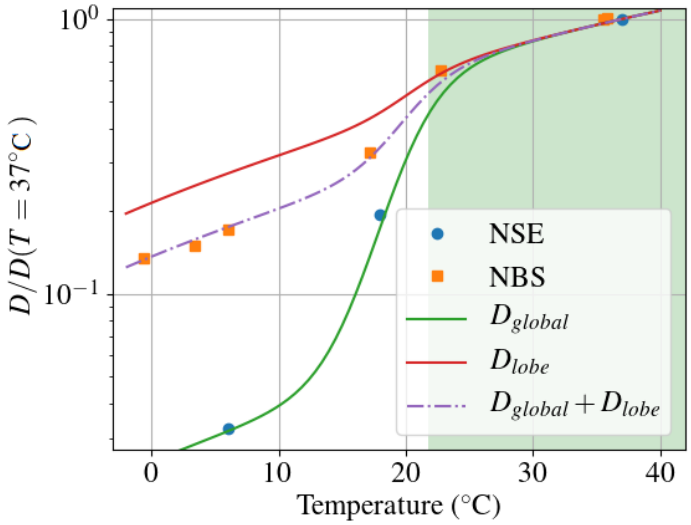

Figure 7.9: a) In blue, the apparent mean squared displacement $\langle u^2 \rangle$ defined by Eq. 7.3, as a function of quench temperature. The values were obtained by binning in a temperature range of 0.9 °C. In red, we show the global diffusion coefficient obtained with NBS on a q-range of 5.8 nm^{-1} to 18.2 nm^{-1}. The green shaded area indicates the temperature range in which the solution is stable as a single phase, the dashed line is a linear fit of the points in the one-phase region and the solid line is a guide to the eye. b) The diffusion coefficient calculated with the two different techniques. The diffusion coefficient for NSE was calculated averaging the diffusion coefficient at high q (in the range 1.3 nm^{-1} $< q <$ 1.75 nm^{-1}). We note that the same trend was seen for another sample for which the parent solution had a concentration of 8% PEG. The solid or dashed lines correspond to the fits according to Eqs. 7.7 and 7.8.

7.2.5 Intra-molecular dynamics

The significant additional decrease of the diffusion coefficient from NSE compared to NBS by a factor of more than 5 requires further discussion. First, while the NBS signal is determined by the incoherent neutron scattering, the NSE signal is dominated by coherent scattering, meaning that structural features, i.e. spatial correlations, could modify the observed NSE relaxation rate. This effect, the so-called de-Gennes-narrowing [108], implies that $D(q)$ follows the inverse of the structure factor $S(q)$. However, no strong q dependence can be observed in the relaxation rate in Fig. 7.8, and de-Gennes-narrowing can thus not explain the additional decrease. This is also supported by the SANS profiles of Fig. 7.2 which do not show a strong correlation peak, and in particular no significant increase when changing from the homogeneous into the phase-separated and arrested state (for details, see Section 7.2.1). Second, the different q-ranges probed by NSE and NBS imply that different motions are probed. In particular, NBS is more sensitive to smaller real-space length scales and thus to intramolecular dynamics of the antibodies, such as lobe motions and local internal motions.

A potential explanation could thus be the different relative contributions of lobe diffusion and self-diffusion of the entire antibody at low and high temperatures, both of which contribute to the experimentally probed displacement in NBS , for a more quantitative estimation see the end of this paragraph. At higher temperature the displacement is dominated by the diffusion of the entire molecule, as indicated by consistent modeling for PEG-free γ-globulin solutions [99]. When lowering the temperature to reach the phase-separated regime, the global diffusion is significantly reduced, as observed by NSE. In this situation, the contribution from the lobe diffusion might become more relevant. This can be explained by the fact that the lobes have more motional freedom left, since given their smaller size the effect of the confinement due to the neighbor cage is reduced.

To verify this interpretation, we model the measured short-time diffusion D_{exp} as the sum of two contributions, one from the diffusion of the lobes and the second one from the diffusion of the entire antibody:

$$D_{\mathrm{exp}} = D_{\mathrm{global}}(T) + D_{\mathrm{lobe}}(T) \tag{7.6}$$

$$D_{\mathrm{global}}(T) = \frac{K_0 T}{\eta(T)} \left(a_g \Theta(T - T_p) + 1 - a_g\right) \tag{7.7}$$

$$D_{\mathrm{lobe}}(T) = \frac{K_0 T}{\sqrt[3]{3}\eta(T)} \left(a_l \Theta(T - T_p) + 1 - a_l\right) \tag{7.8}$$

Here, we use the approximation that the movement of the lobe is not confined on the time scales of nanoseconds probed by NBS. Each of the diffusion coefficient contains a temperature dependence which includes temperature and viscosity as in the Stokes-Einstein equation, but also a step function $\Theta(T - T_p)$, which models the decrease of the mobility and the possible change in the hydrodynamic radius due to the change in concentration (in the phase separated region the signal from the dense phase is predominant) as indicated in Eqs. (7.7) and (7.8). T_p indicates the temperature at which the phase separation starts, which was set to 20.5 °C. The additional factor $\frac{1}{\sqrt[3]{3}}$ in equation 7.8 accounts for the difference in the effective radius of an individual lobe with respect to the overall protein. The scalar values a_g and a_l express the degree of reduction of the diffusion coefficient. The best agreement of the model with the experimental data can be found for $a_l = 0.3$ and $a_g = 0.92$ (Fig. 7.9b). These values indicate that D_{lobe} decreases of 30% due to the phase separation, and D_{global} of 92%, which supports the interpretation that the lobe diffusion is less affected by the crowding of the solution. The values of the diffusion coefficient without the normalization evidence the consequence of the different behavior of the global and the lobe diffusion coefficient (Fig. 7.10): While at high temperature they both contribute to the diffusion, at low temperatures the global diffusion coefficient becomes negligible. As suggested in the beginning of the section the movement of the whole molecule might be hindered by other molecules, while the small size of the lobe can allow more possibility of movement in local voids, having as a result a decrease of only 30%. In conclusion, the model provides a conclusive picture consistent with the experimental data (Fig. 7.9b).

7.2.6 Geometrical confinement of local dynamics of protein residues

As a measure of the local dynamics and flexibility, we analyzed the EISF $A_0(q)$, which provides an estimation of the dynamical confinement of the faster local dynamics (Fig. 7.11a). The movements associated with the internal dynamics are very fast on time scales of a few to hundreds of picoseconds, and do not correspond to the motion of the lobes, but rather to the movements of the residues. Following a previous work [99], the value of Λ was fixed to $0.99\sqrt{3}$ Å $\sim$1.715 Å, i.e. the average distance of the hydrogen atoms in methyl groups (-CH_3). In this interpretation, the atoms are jumping between 3 sites at an angular distance of 120°.

The value of the fraction p of fixed hydrogen atoms decreases from $\sim$0.4 to $\sim$0.1 with increasing temperature (Fig. 7.11b). This trend is expected considering that the thermal energy decreases at low temperature and that the crowding increases in the phase separation region.

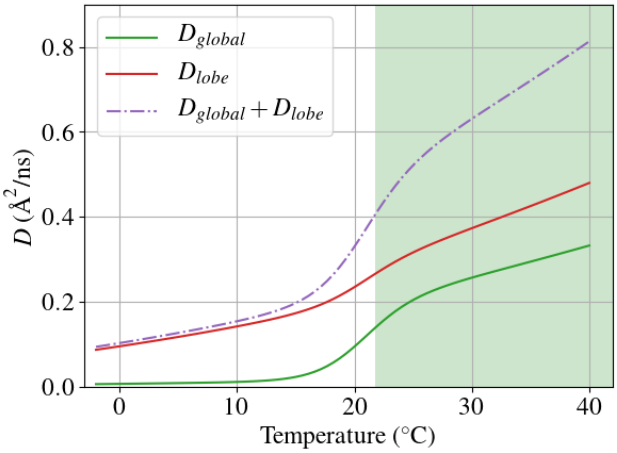

Figure 7.10: Diffusion coefficients from Eqs. 7.7 and 7.8. The green shaded area corresponds to the one-phase region.

The prefactor value of f, instead, is almost constant (Fig. 7.11c), which is consistent with the assumption that hydrogen atoms within the methyl groups are not strongly affected by the crowding. The local motions becomes more flexible with increasing temperature are thus associated with larger motions of the side-chains and the backbone.

7.3 Conclusions

The macroscopically observable phase separation has a strong impact on diffusion on scales of individual antibodies and below, as reflected inter-alia by the diffusive mean squared displacement. By studying the dynamics of antibodies in the dense phase we mimic the high-density liquid formulations. We interpret the results as an interesting interplay of localized internal motions, diffusion of lobes and diffusion of the entire molecule. The apparent diffusion coefficients obtained with neutron spin echo and neutron backscattering spectroscopy show a different temperature dependence, with the first one having a very sharp decrease, and the latter a more shallow one. This difference is explained with a simple model, which takes into account for diffusion of lobes and the entire antibody. With this model we show that while at high temperatures the diffusion seems to be controlled by both global and lobe diffusion, at low temperatures the global diffusion is negligible, and the lobe diffusion dominates the signal. The implication for high-concentration liquid formulations is relevant, since our findings

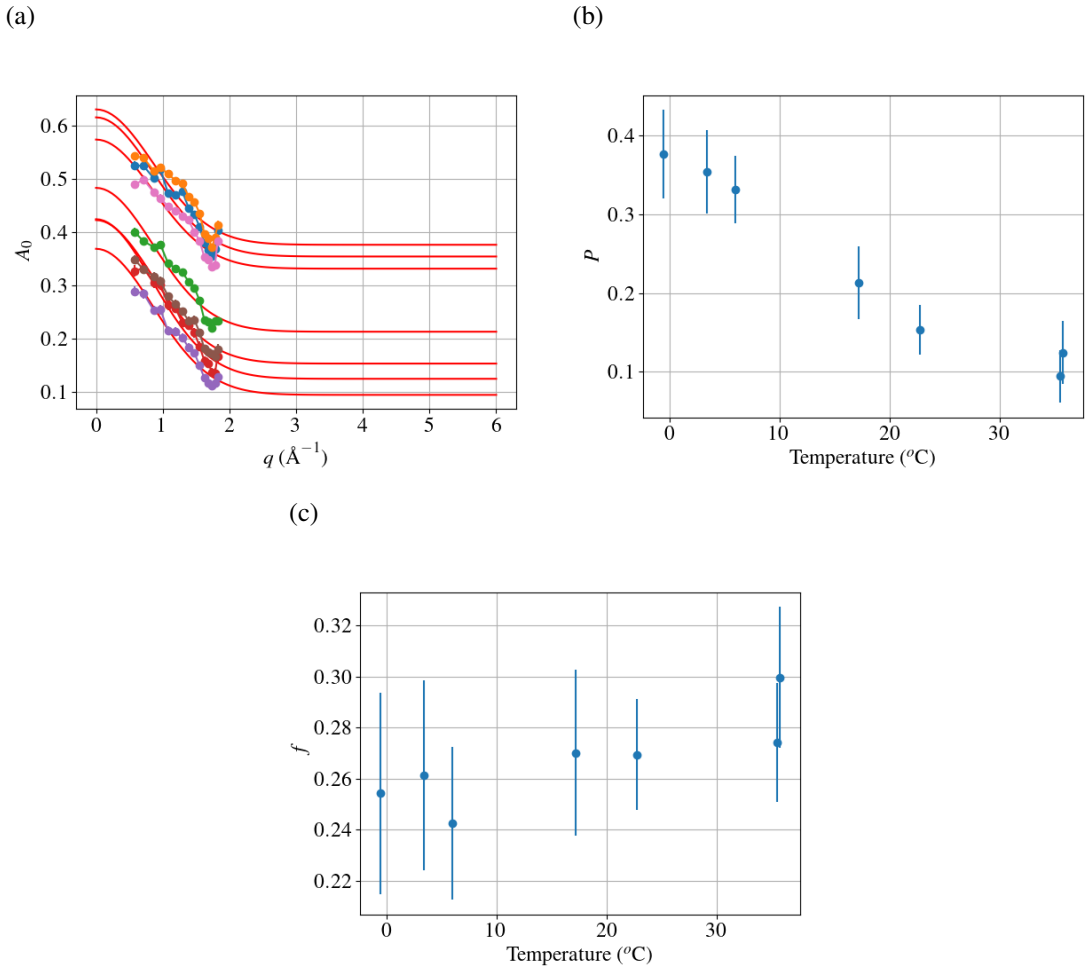

Figure 7.11: a) The parameter $A_0(q)$ obtained from the global fit of the NBS full spectra measured at different temperatures as a function of q, fitted according with equation 7.2. b) The fraction p of fixed hydrogens atoms as a function of temperature. c) The prefactor f from Eq. 7.2 as a function of the temperature.

imply that the dynamics, which is a precondition of the biological function of the protein, is preserved even under highly crowded conditions.

Chapter 8

Towards molecular length scale diffusion with XPCS

The results obtained with XFEL are based on Ref. [238].

8.1 Introduction

The molecular diffusion of protein solution can be used to understand many macroscopic properties, such as viscosity, transport, aggregation and stability, and protein interactions. Unfortunately, until now the time scales that can be measured are limited up to hundreds of nanoseconds, which is not sufficient if the proteins are in naturally crowded environment, as the cytoplasm can be, or if their concentration is very high. An example of this is the protein α-crystal, which is present in eye-lenses [239]. When the concentration of the protein is elevated there is the possibility that the solution undergo through a glass or gel transition, which cause a further decrease of the diffusion coefficient. This is also the case for antibodies solutions, where the viscosity increases very fast as the concentration increases [85]. Another example of system where this type of transitions have been seen is the condensates formed via liquid-liquid phase separation [203]. In this study we use a protein-polymer model system to probe the diffusion of the particles in highly crowded environment and during arrested phase separation. XPCS has holds the promise to access the long time diffusion of the solution, because, unlike neutron backscattering, the probed time is in principle limited only by the experimental time available with the instrument and the stability of the protein under the X-ray beam.

Proteins are expected to present a transient sub-diffusion interval for times in the range of

the interaction time τ_i [240; 68; 173], defined as the time that a particle requires to move a distance equal to its radius, hence $\tau_i = \frac{Rp^2}{D_0}$ with R_p being the radius of the protein and D_0 the short-time diffusion coefficient. Using as parameters $R_p = 55$ Å and the diffusion coefficient in the one phase region from Chapter 7 $D_0 = 0.3$ Å^2/ns, this results in $\tau_i \sim 9$ µs. In the phase separated region, in particular in the arrested phase separation where the short-time diffusion coefficient has a value of $D_0 = 0.01$ Å^2/ns the interaction times has a value of circa $\tau_i \sim 300$ µs. To have a complete picture of the diffusion of the proteins it is necessary to monitor both, short and long time diffusion, which corresponds to respectively times much smaller and much larger than τ_i. To be able to access the dynamics in the range of µm or less, the synchrotron radiation brightness is not sufficient, and the use of a XFEL is necessary. However, the lower brightness of synchrotron radiation is not limiting when the long time diffusion is probed, since the exposure time can be increased.

While a diffusion without any beam effects could not be measured, the beam effect on the structure and the diffusion are characterized with both synchrotron and XFEL radiation. The microsecond diffusion was compared with the diffusion coefficient obtained with DLS yielding to values that are in the same order of magnitude. From the correlation functions on the seconds scale aging can be seen only at small values of q. Correlation function at different temperatures were measured, showing a clear temperature dependence. Suggesting that while the system is influenced by the beam some characteristics are still present.

8.2 Results and discussion

8.2.1 Consideration on beam effects

To characterise the beam effects on the sample we divide them in two categories: structural changes and diffusion changes. The firsts are given by the changes in the intensity with doses, the latters, instead, are the changes in the diffusion due to the beam, and can be quantified by the changes in the correlation functions. Their origin can be different, and different dose amounts and different dose rates can cause different types of damage [157] (for more information see Section 1.2.4). Hence, it is in principle possible to have two different effects of the beam when using XFEL or synchrotron radiation.

Component	Chemical formula	Volume	Transmission
Water	H_2O	70%	77%
Protein	$C_{3288}H_{5085}N_{897}O_{1015}S_{21}$	30%	91%

Table 8.1: Tramission of an X-ray beam with energy 9 keV calculated via `https://11bm.xray.aps.anl.gov/absorb/absorb.php` with the chemical formula and the volume fraction shown in the table.

8.2.1.1 Beam effects with synchrotron radiation on the structure

To characterize the structural effects on the sample the intensity was monitored for different exposure times, i.e. different dose accumulated on the sample. The intensity profile is changing with dose, in particular for $q < 0.1\text{nm}^{-1}$ the intensity decreases with dose, and for $q > 0.1\text{nm}^{-1}$ an increase is observed (Fig. 8.1a). To understand what this change correspond to, it is necessary to know the form factor of the protein [83]. Since the form factor is constant at $q < 0.1\text{nm}^{-1}$ [83], the dose dependent change in intensity at $q < 0.1\text{nm}^{-1}$ cannot be attributed to a change of shape of the protein, but only to changes in the structure factor or an increase of size of the proteins, meaning aggregation. However, aggregation cannot be the cause of this decrease, since this would result in an increase of the intensity. Hence, the change is due to a structure factor change. In this regime $S(q \to 0) \propto \frac{1}{1+B_2\rho}$, where ρ is the density of the proteins and B_2 is the second virial coefficient, a parameter that is a measure of the interaction strength, which is negative if the particles are attractive and positive if they are repulsive. A decrease of $S(q)$ corresponds then to a increase of B_2, i.e. to overall less attractive particles. The reason behind the changes in the pair potential of the proteins are related to the process of interaction of the beam with the sample. If we compare the transmission of the beam due to the single components of the sample (Table 8.1) we can see that the transmission after the interaction with the proteins is much higher than with water. Possibly the changes in the structure factor are due to radical produced in the solvent [159], which can change also the surface charge of the proteins since the radicals that interact with the proteins via ionization [241].

At $q < 0.1\text{nm}^{-1}$ the intensity change can be seen at much lower dose compare to $q > 0.1\text{nm}^{-1}$. The intensity changes at $q > 0.1\text{nm}^{-1}$ can have contributions from both the form factor which are not easily distinguishable and it is not possible to see exactly when the form factor changes are visible. Nevertheless they are appearing later than the changes in the structure factor.

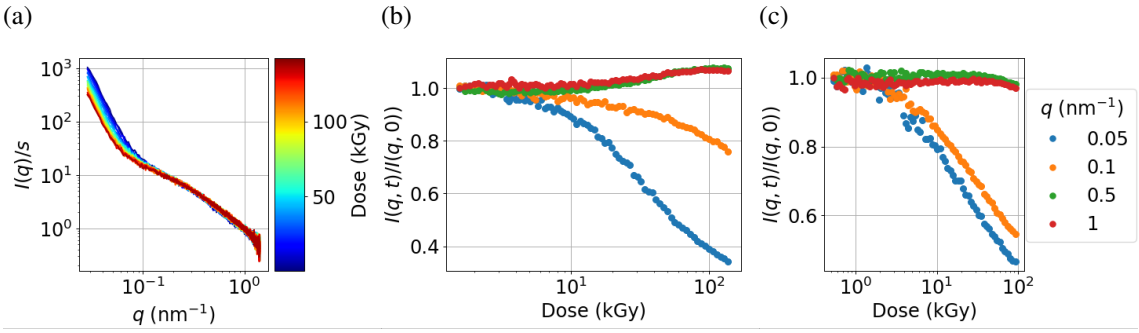

Figure 8.1: a) Scattering intensity at different exposure times after a quench to 6°C. b) The normalised intensity for different q values as a function of dose. The measurement parameters used are reported in Table 3.1 as measurement 1. c)The normalised intensity at 25°C for different q values as a function of dose. The measurement parameters used are reported in Table 3.1 as measurement 5.

To have a better understanding on the damage process different temperatures (0°C, 6°C, 10°C and 25°C) were measured and compared. The intensity curves are temperature dependent (Fig. 8.2b), because they reflect the temperature dependency of pair potential of the proteins and the presence of the phase separation domains at temperatures below 21°C. After irradiating the sample the difference between the curves becomes much less pronounced. This can be due to the decrease of the attraction between proteins, which cause the dissolution of the phase separation domains. This hypothesis is supported by the change in intensity with dose at 25°C (Fig. 8.1c): at $q > 0.1$ nm^{-1} the intensity does not increase as previously seen at 6°C (Fig. 8.1), or the other temperatures in the phase separation region, but it decreases instead.

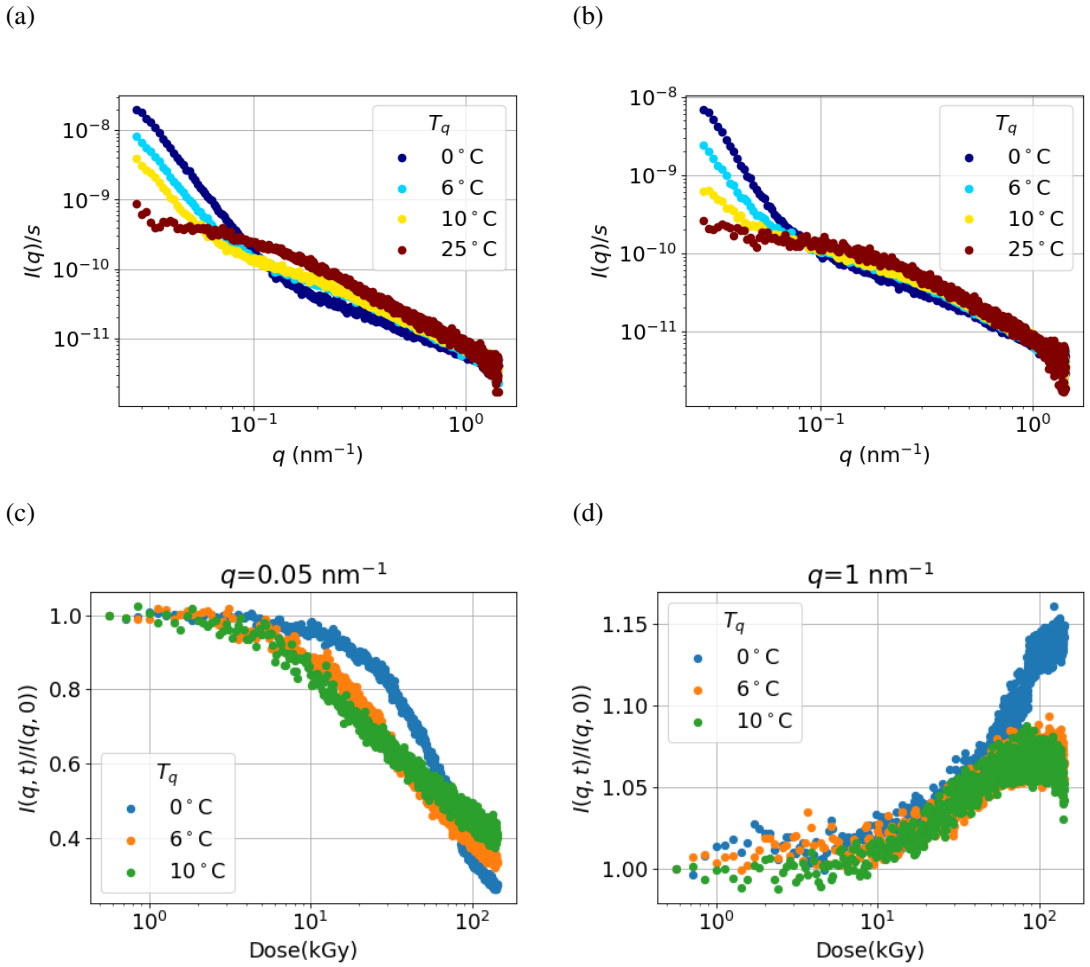

Figure 8.2: a) The intensity curves at temperatures T_q=0, 6, 10 and 25°C, before the beam affects the intensity curves and b) after the beam influence. c) The normalised intensity as a function of exposure time at the q values of 0.1 nm^{-1} and 1 nm^{-1} for the temperatures T_q=0, 6 and 10°C. The measurement parameters used are reported in Table 3.1 as measurement 2,3 and 4 respectively.

8.2.1.2 Beam effects with synchrotron radiation on the diffusion

To access the diffusion changes due to the beam the TTCs were calculated. The TTCs calculated averaging over 300 measurements are shown in Fig. 8.3. Aging can be seen in the TTCs, and in the one dimensional cuts $C(t_w, t_w + t)$ at different t_w. This aging is beam induced, in fact if the data are partition in smaller subgroups the TTC show the same aging. Interestingly, at 6°C the beam induces aging which is clearly visible at low q is almost not visible at high q. This could reflect the structural changes seen in the previous section, which are also more

pronounced at low q.

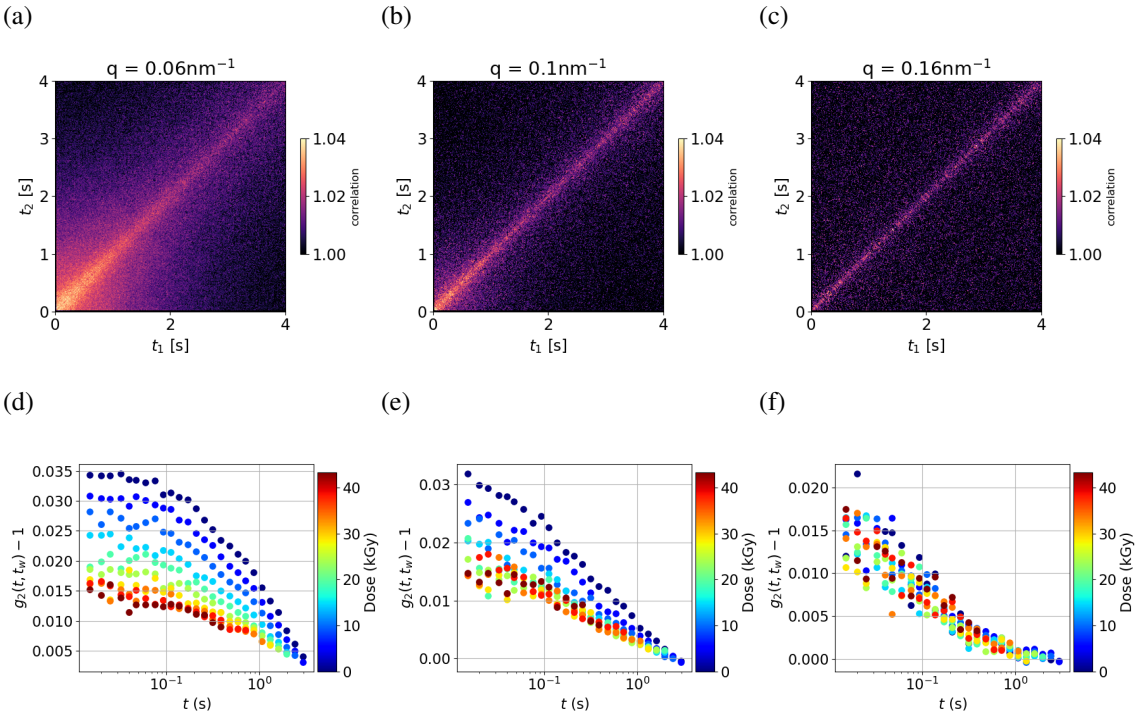

Figure 8.3: Upper panels: TTCs calculated at different q vectors at 6°C. Lower panels: the corresponding $C(t_{exp}, t + t_{exp}, q)$ function obtained with at different exposure time t_{exp}, hence different dose.

However, at different temperatures aging is visible also at higher q. Comparing the TTCs at $q = 0.2$ nm^{-1} at different temperatures (Fig. 8.4), we see that at 0°C the TTC is not constant and the diffusion of the system is getting faster, while at 10°C an opposite behavior can be observed. This suggest that the radiation effect on the diffusion is different for different temperatures.

To better understand the type of influence that the beam has on the sample it is interesting to understand which kind of motion the X-rays are inducing on the proteins. To do so, the correlation functions were calculated for the q values at which no beam induced aging was visible. The function $g_2(t, q)$ can be obtained via Eq. 8.1, where $\langle \cdot \rangle_q$ in an average of pixel with the same q value and $\langle \cdot \rangle_\tau$ is an average over the value of τ. To be able to have a large enough signal to noise ratio 1159 measurements were merged, for a total of 927200 total images.

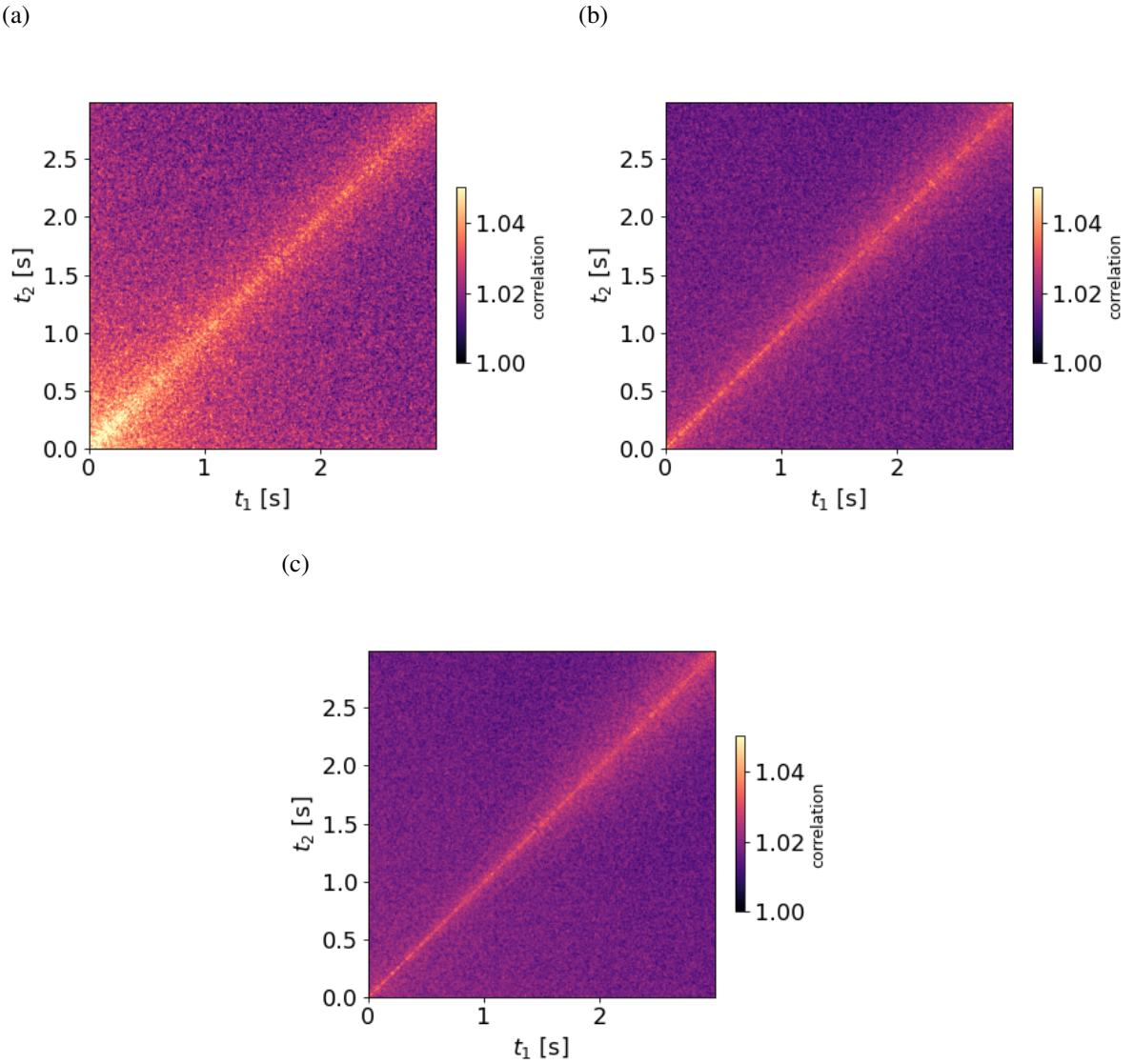

Figure 8.4: TTCs calculated at q =0.2 nm^{-1} at temperature of a) 0°C b) 6°C c) 10°C. The images are obtain averaging over 80 measurements.

$$g_2(q,t) = \frac{\langle\langle I(\vec{q},\tau)I(\vec{q},\tau+t)\rangle_\tau\rangle_q}{\langle\langle I(\vec{q},\tau)\rangle_\tau\rangle_q^2} \tag{8.1}$$

The curves obtained were than fitted with Eq. 8.2. To improve the stability of the fit a global fit was performed, a q dependence of the parameters $\beta(q) = \exp(-nq^\alpha)$ and $\gamma(q) = m_1 q + m2$

was introduced. The fit and the resulting parameters are reported in Fig. 8.5.

$$g_2 - 1 = \beta(q)\exp(-2(t/\tau(q))^{\gamma(q)}) \tag{8.2}$$

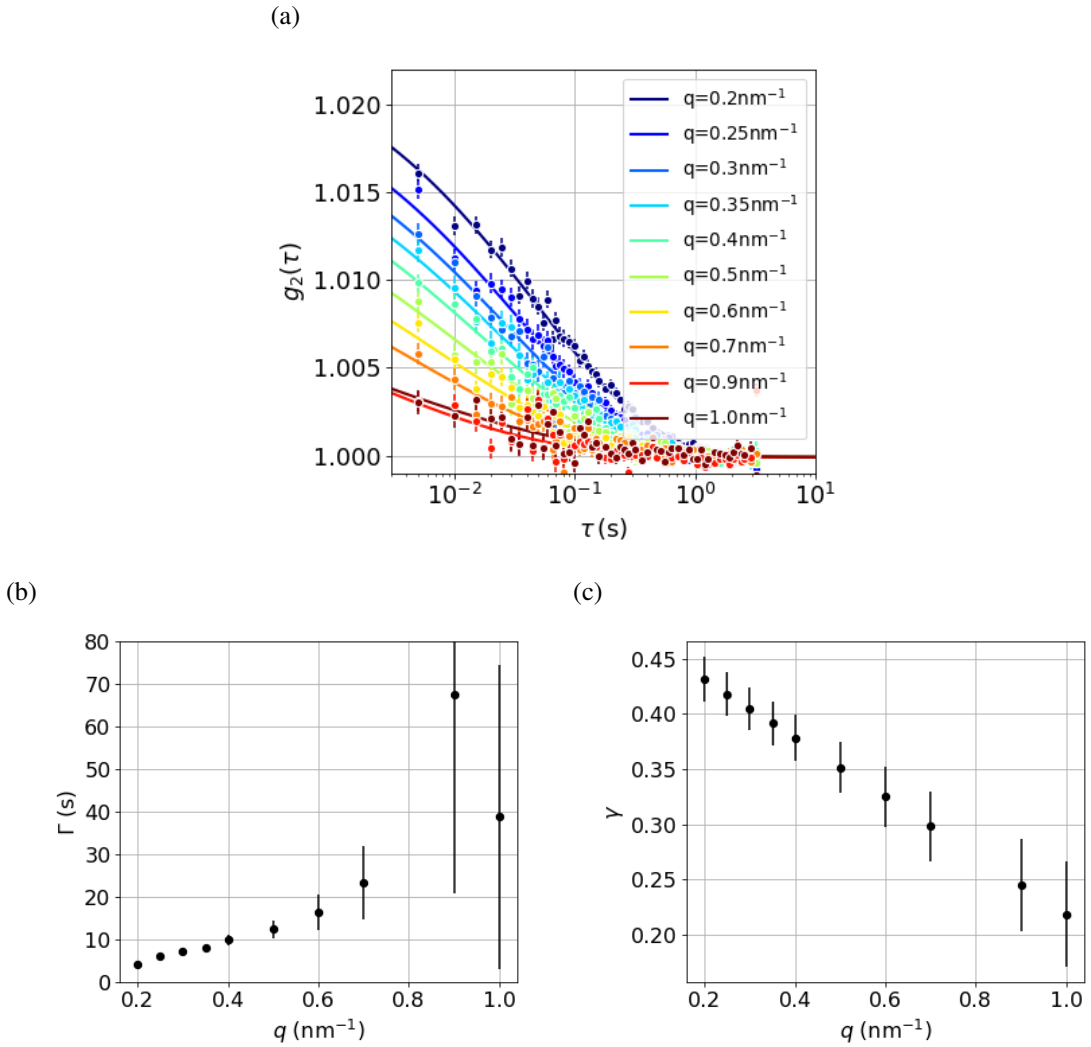

Figure 8.5: a) g_2 functions for different q values and the fitted curve. b) The decorrelation rate from the fit of equation 8.2 as a function of q. c) The KWW exponent as a function of q. The measurement parameters used are reported in Table 3.1 as measurement 1.

Interestingly, the decorrelation rate $\Gamma(q) = \frac{1}{\tau(q)}$ is linear in q, which suggest a ballistic or driven type of diffusion, but $\gamma(q)$ has a value lower than 1, which suggest instead some type of subdiffusive motion. A similar behavior is rare, but was already seen for colloidal particles diffusing in ice [141] and in a colloid stabilized cream [242], however no clear interpretation

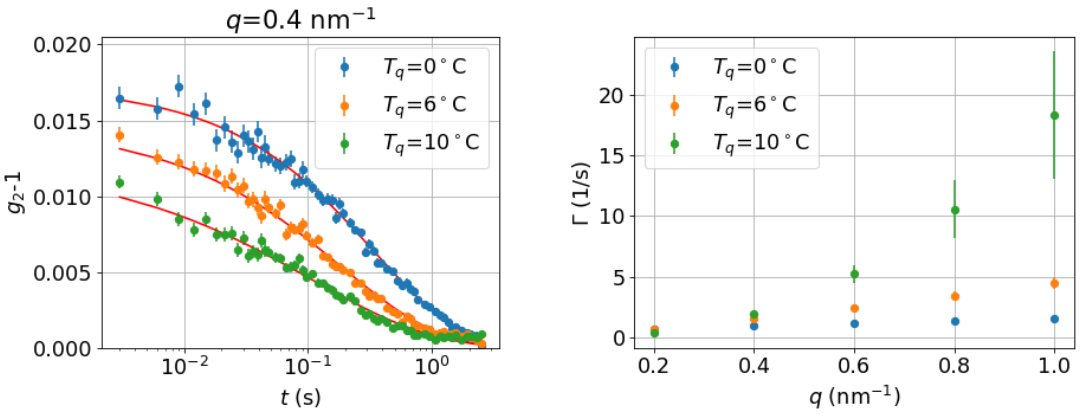

Figure 8.6: a)g_2 functions calculated at q =0.4 nm^{-1} for different temperatures with in red the fitted curves following Eq. 8.2. b) The decorrelation rate as a function of q for different temperatures.

has been proposed so far.

To have quantification of the effect of the beam on the diffusion at different temperatures the $g_2(t,q)$ function where calculated at at different q values. Since the TTCs show aging both at 0°C and at 10°C the results cannot be used to get a precise estimation of value but simply an overall trend.

The correlation functions are more stretched and the decorrelation time is smaller at higher temperatures. This could be in principle be due to the different radiation effects on the sample at different temperatures, but from the beam induced aging it seems that the proteins at low temperature tend to move faster if the dose is increased, while for high temperature the radiation slows down the proteins. Hence, if the diffusion would be purely beam induced than a faster dynamics should be visible at low temperature and not vice-versa. This does not imply that the diffusion here is not influenced by the beam, but that some characteristics of the system could be still present. In fact, it is expected that the diffusion decreases fast with temperature in the vicinity of the gel transition as demonstrated in Section 6.

Another reason for thinking that the decay measured is not all beam induced is that the two time correlation functions show aging. To probe it multiple measurement were performed, on different position in the capillary, so that the dose would not be accumulated. Fig. 8.7a show the time dependence of the correlation functions. This demonstrates that the system is aging, in fact the decorrelation time increases with waiting time t_w. This increase is more pronounced at low q than at high q on the contrary of what was seen with simulations for colloidal systems [47; 243], where even at high q aging was present. This result is, however, consistent with the

results obtained in the second study reported in this thesis. In fact, with both NSE and NBS no aging was visible.

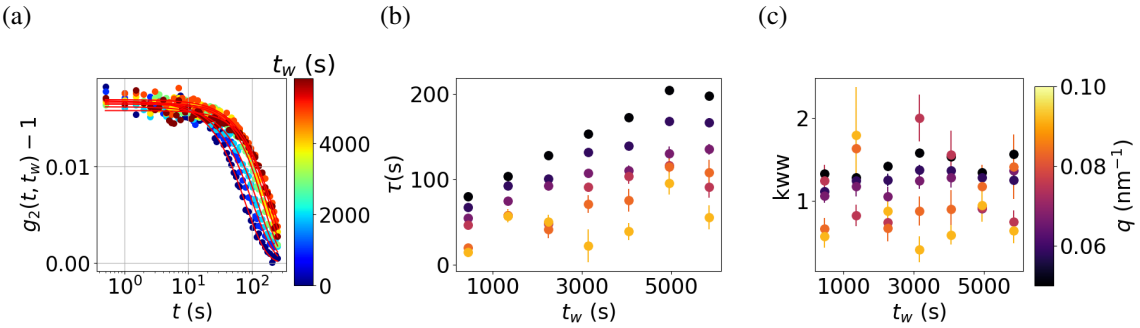

Figure 8.7: a) Correlation function collected at -5°C for different waiting time t_w for $q = 0.05$ µm^{-1}. The red solid lines are the fits of a KWW exponential function. b) The value of the decorrelation time τ as a function of t_w at different value of q as indicated in the legend. c) The value of the KWW exponent as a function of t_w at different value of q as indicated in the legend.

8.2.1.3 Beam effect with XFEL radiation

To monitor the changes in intensity the Porod invariant $Q_p(t)$ was calculated and monitored as a function of dose (Fig. 8.8a). This quantity is defined in Eq. 8.3. In the definition of the Porod invariant the limits of the integration interval a and b are 0 and ∞, but given the limited q range measured they where set to a =0.1 nm^{-1} and b =0.6 nm^{-1}.

$$Q_p(t) = \int_a^b I(q,t)q^2 dq \tag{8.3}$$

The diffusion changes due to the beam were characterised via monitoring the diffusion coefficient as a function of dose (Fig. 8.8b). The value of the diffusion coefficients were obtained by fitting the g_2 for more information see Ref. [238]. There are two stage in the effect of beam: in the first stage there is no structural change, the diffusion coefficient is not changing with dose, but measurement with higher dose rates results in faster diffusion. In a second stage there are structural damage and the diffusion coefficient decreases with dose. A possible interpretation of this behavior is that the beam giving energy to the system speeds up the diffusion of the particles. When this energy reaches the threshold of beam damage the protein start to aggregate and as a consequence the diffusion decreases.

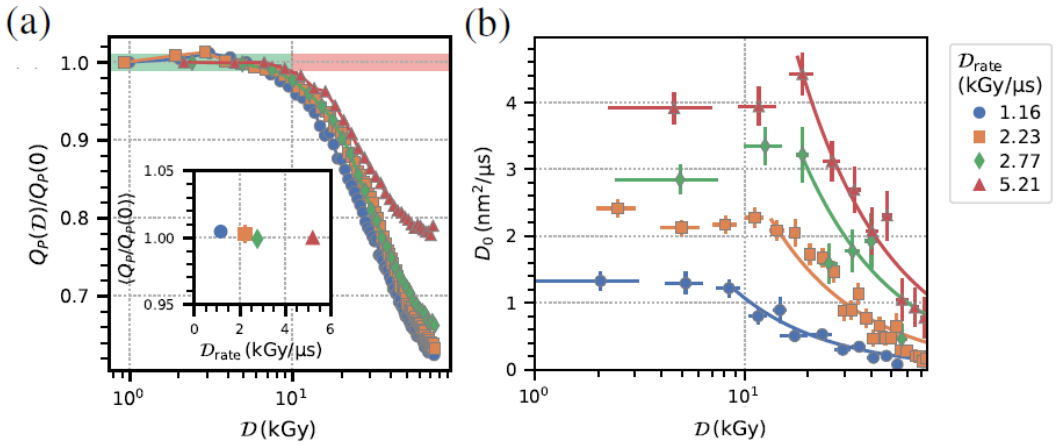

Figure 8.8: a) The normalized Porod invariant $Q_p(t)/Q_p(0)$ calculated in the range 0.1 nm^{-1} < q <0.6 nm^{-1} as a function of dose. b) The diffusion coefficient as a function of dose. These figures are from Ref. [238].

The effect of the beam on the proteins are not the only one that have to be considered. In fact, it was shown that the beam can also induce heat [244]. This influences the proteins in two ways: In first place the heating can increase the temperature of the solution to an extent that

the temperature denaturation threshold can be reached. Even if the temperature increase ΔT is kept below the denaturation temperature, there is another important effect to be considered, namely that the diffusion coefficient depends directly on the temperature, and also indirectly since the viscosity is also a function of temperature. For this reason when comparing the diffusion coefficient obtained with DLS and XPCS in figure 8.9 this temperature increased was considered. The diffusion coefficient obtained with XPCS is for some measurements larger than the equivalent obtained with DLS, while for others the two values match. This is strongly indicating that a beam effect free diffusion can be obtain with XFEL radiation. Nevertheless it is important to notice that the two values could be different, due to the length scales at which the DLS and XPCS were probed.

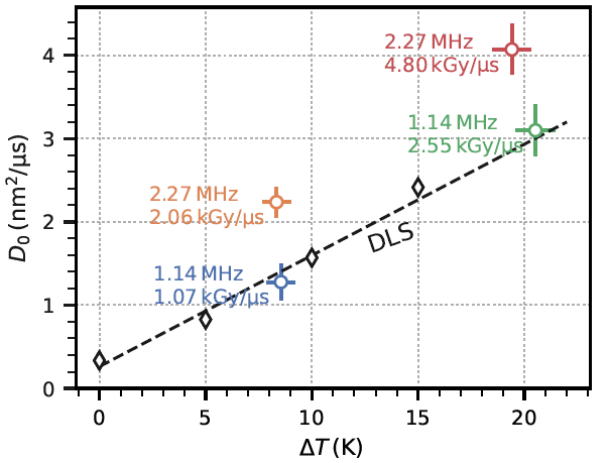

Figure 8.9: Diffusion coefficient estimated with DLS measurements at different temperatures and the one obtained with XPCS using XFEL radiation as a function of the estimated increase in the diffusion coefficient. This figure is from Ref. [238].

8.2.2 Short-time diffusion via NSE

We measured sample B in the single-phase state (37°C), during phase separation (18°), and in the kinetically arrested phase separation (6°C). Looking at the Intermediate scattering function (ISF) obtained by NSE (Fig. 8.10) it is possible to infer that the signal in the phase separated regions is dominated by the dense phase. In fact, comparing the curves at 37°C and at 6°C, we see that at 6°C there is only one decay (not two as expected in case we would see two species) and its relaxation time is larger than the relaxation time at 37°C. This difference is larger than

the expected temperature dependence of the Stokes-Einstein equation, to understand this difference one has to take into consideration the phase separation in the system. The dense phase at 6°C has a concentration higher than the concentration of the one-phase solution, which can explain the increase of the relaxation time. The dilute phase instead, having a concentration much lower than the one-phase solution, is expected to have a faster relaxation time. However the curves do not show a faster relaxation, which is suggesting that this contribution is not visible. This hypothesis is corroborated by the fact that the dilute phase has a much lower concentration and the volume (the sample in the one-phase is close to the high density branch of the binodal line), hence the number of proteins in the dilute phase is limited.

In Fig. 8.10 the ISF in logarithmic scale at 37°C at large q as a function of time presents a non linear dependence, hence the exponential decay is stretched as reported in Chapter 7 . This was already observed in monoclonal antibodies and explained by the presence of internal motion of the protein ([100]). In this case it could be that non Brownian contributions are present due to the high concentration of the protein and the addition of the polymer, but given the limited range of the ISF it is not possible to confirm or confute this statement. At lower q most of the decay of the correlation function is not visible, but in the visible range the data are consistent with a simple exponential, which is evident by the linear dependence of the data points in Fig. 8.10.

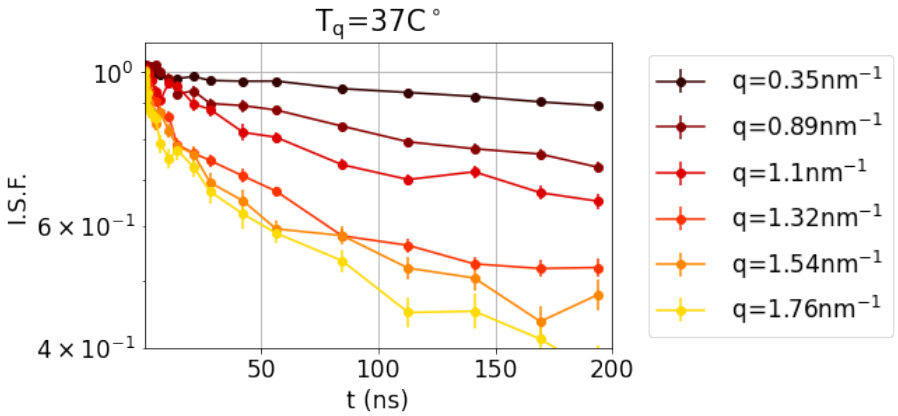

Figure 8.10: The ISF of sample B collected at 37°C with NSE.

8.2.3 Potential of accessing molecular length scale with XPCS and the combination with NSE

The diffusion of the proteins in the arrested state covers many order of magnitude, to be able to measure the spectra different techniques have to be used and combined. To compare the results from XPCS and NSE, it is necessary to compare the same quantities. From the g_2 function it is possible to obtain the ISF via Eq. 8.4 (for more detail see Section 3.3.1). The value of the contrast β, is a quantity dependent on the setup. There are various methods for estimating it: in case it is known that all the decays of the correlation function are visible in the measured interval, the contrast can be estimate by the fitting. In case only one decay is present Eq. 8.2, can be fitted and the contrast corresponds to the value of $\beta(q)$.

$$g_2(q,t) = 1 + \beta|\mathrm{ISF}(q,t)|^2 \tag{8.4}$$

This approach was used for the data collected in a range of $\sim$µs at 37°C, resulting in the correlation functions shown in 8.11a. The system is diffusive as expected, and the combination of the two techniques is a confirmation of the validity of the data collected with XFEL-XPCS. For the data measured in the range of $\sim$100 ms at 6°C (and in general at temperatures in which the solution undergoes phase separation) multiple decays are expected [46; 47; 50]. For this reason the value of the contrast was estimated experimentally, by measuring a static sample (silica powder). The ISF obtained from the g_2 curve shown in Fig. 8.5 are shown in Fig. 8.11b. It is clear that the correlation functions do not show only one decay. From the current experimental curves it seems that there are two decays as predicted from the simulations of colloid polymer mixtures [47]. However, the lack of the points at intermediate value of t does not permit to state with certainty that there are no further decays. Furthermore, it is important to remember that the data obtained with XPCS at the synchrotron are influenced by the beam induced effects.

8.3 Conclusions

We measured the system in the one phase region with XFEL radiation and we found two stages: during the first one there are no structural changes and the diffusion coefficient is larger for higher dose rates. In the second stage structural changes are visible via the scattering intensity changes and the diffusion coefficient decreases with the dose accumulated on the

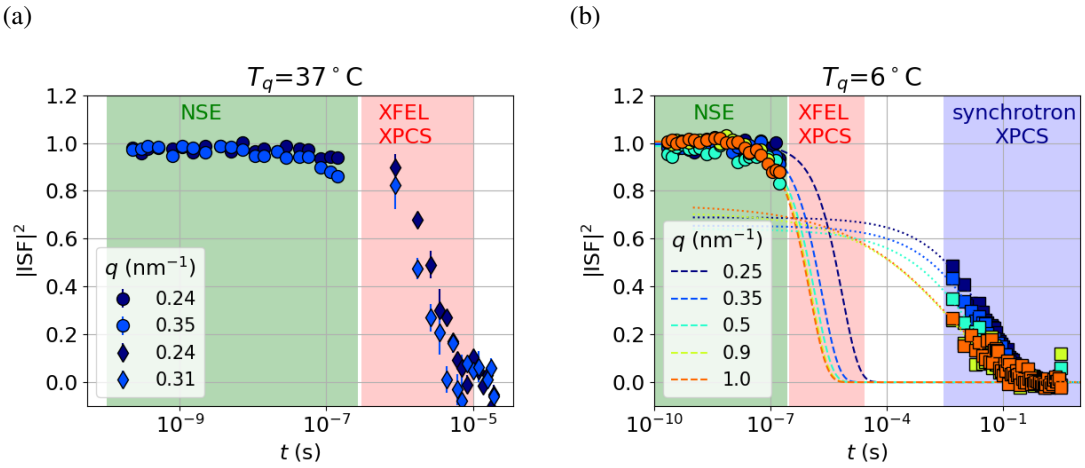

Figure 8.11: a) The ISF in the single phase region measured at 37°C for NSE (sample A of Table 2.1 and at 37°C=25°C+ΔT=12.5°C, where the ΔT is the temperature increase with a dose rate of 2.77 kGy/µs sample C of Table 2.1. b) The ISF measured at 6°C with NSE (Sample B) and synchrotron-XPCS (Sample C). The dashed line are a simple exponential fit of the NSE. In the two figures the green shaded area show time scales covered by NSE, the red one the XFEL-XPCS and the blue one the synchrotron-XPCS time range.

sample. Comparing the data with the DLS data we see that for lowest does rate the results are matching, proving that it is in principle possible to measure the sample.

With synchrotron radiation the system was measured at different temperatures, and the influence of the beam was probed at different temperatures. While a beam influence free diffusion was not measured, the temperature trend of the decorrelation time is consistent with what is expected from the system. Furthermore, the aging of the system is visible at low q despite the beam influence. This suggest that the correlation curves are not showing only beam effects. Hence, by finely tuning the measurement parameter, for example by decreasing the flux of photons on the sample and increasing the repetition of the measurement, it is could be possible to measure the diffusion of the proteins. The beam influenced diffusion was characterised, showing a very peculiar type of dynamics, with stretched exponentials and linear dependence of the decorrelation rate from q. This type of diffusion was seen for colloidal particles diffusing in ice [141] and for a colloid stabilized cream [242]. We show that it is possible to combine the neutron and X-ray scattering, and that it is necessary to employ both NSE and XPCS to cover the whole dynamical range of the sample during phase separation.

Chapter 9

Conclusion and perspectives

In this section, a summary of the main conclusions is reported as well as open questions and an outlook on possible future work.

9.1 Conclusion

The focus of this thesis is the diffusion of γ-globulin in water solution with PEG with scattering techniques. As this system presents an arrested phase separation, it is not trivial to access the dynamics. First, the system is out of equilibrium, meaning that the diffusion properties are changing with time. We addressed this challenge by using XPCS which allows for time dependent measurements with high temporal resolution. Second, the system consists of different parts that have to be monitored. We achieve a complete description of the system by monitoring not only the diffusion of the proteins, but also the diffusion and growth of the phase separation domains. Finally, to understand the influence of the phase separation also the single phase behavior has to be understood. For this reason the solution was probed in two different parts of the phase diagram: in the phase separation region as well as the single phase region.

Single phase region The system was studied in the single phase region with different techniques (Fig. 9.1), monitoring the diffusion on macroscopic length scale (DLS) and the short-time diffusion at molecular length scales (NSE, NBS and XPCS). The short-time diffusion is Brownian at all length scales as expected for a simple liquid and the temperature dependence of the diffusion coefficient can be described by the Stokes-Einstein equation. Correlation functions obtained with NSE shows more than one simple decay at $q > 1\text{nm}^{-1}$ due

the non-spherical shape of the protein as seen previously in literature. The combination of NSE and XFEL-XPCS allows to access the diffusion on the microseconds time scale at $0.1\text{nm}^{-1} < q < 0.5\text{nm}^{-1}$ showing also Browinian diffusion, and a single decay. On micrometer length scale, the correlation functions show two distinct decays. The faster one, which we associate with the short time diffusion, has Brownian motion features. Furthermore, for the slow decay the q dependence of the decorrelation rate is not quadratic, which comparing with previous results might be due to the closeness to the glass transition.

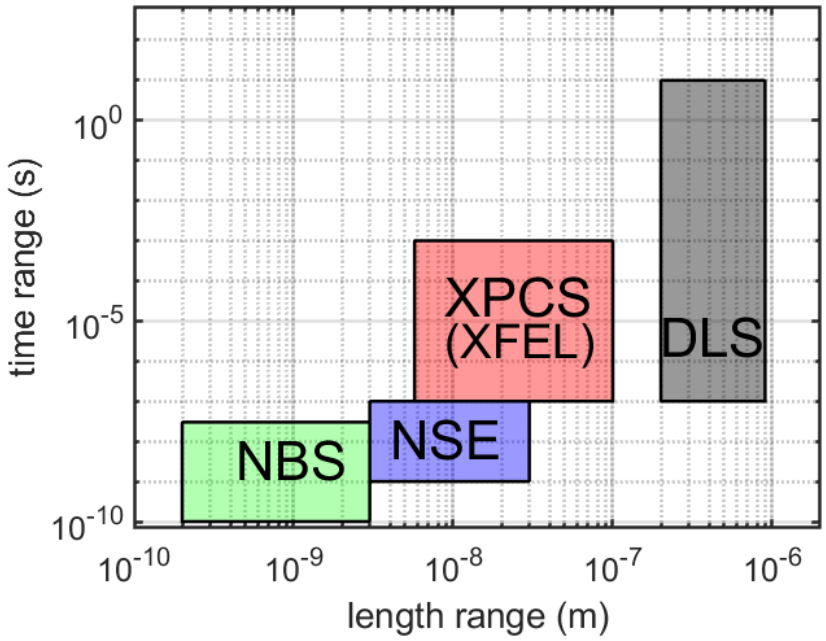

Figure 9.1: Summary of the measurements performed on the system in the single phase region, indicating the time and length scales covered.

Phase separation region The diffusion of the proteins was also studied while the system undergoes LLPS and at very low temperatures ($T_q \leq 6°C$) when the phase separation is slowed down to an extent that the domain growth is almost completely arrested (Fig. 9.2). At molecular length, the diffusion is clearly affected by the macroscopic phase separation. The temperature dependence of the diffusion coefficient obtained via NSE and NBS at temperatures below the phase separation temperature shows a deviation from the Stokes-Einstein relation, probably due to the different crowding conditions in the dense phase. There is a discrepancy between the temperature dependence of the diffusion coefficient obtained with NSE and NBS. This can be explained by taking into account that the diffusion probed with NBS has two different components: one due to the movement of the whole protein and the second one due to the motion of the lobes of the protein. In this case, while the movement of the whole protein is strongly reduced by the crowding, the lobes are still free to move due to their smaller size. This gives rise to the discrepancy with the NSE diffusion coefficient, which is not sensitive to this movement since it probes in a smaller q range. The fact that the diffusion coefficient in the dense phase has such a low value is consistent with the literature, which states that the arrest of the spinodal decomposition is originated from the molecular slowdown and the large difference in diffusivity between dense phase and dilute phase [51; 39]. The long time diffusion at molecular length scale without beam influence could not be accessed so far, nevertheless it was possible to characterise how the beam influences the diffusion and structure of the sample. A dependency of the beam damage threshold on not only dose, but also dose rate is evident, as shown also by other studies [157]. The sample was measured at different temperatures, resulting in a diffusion coefficient that is temperature dependent even above the beam damage threshold. This means that the decay visible in the correlation function is not only due to the damage, but part of the characteristics of the system are conserved, suggesting that it can be measured with this method after refining the tuning of the experimental parameters. The beam influence on the diffusion was characterised, showing a very peculiar type of dynamics, with stretched exponentials and linear dependence of the decorrelation rate from q. This type of diffusion was observed for colloidal particles diffusing in ice [141] and for a colloid stabilized cream [242]. We show that it is possible to combine neutron and X-ray scattering, and that it is necessary to employ both NSE and XPCS to cover the whole dynamical range of the sample during phase separation. Probing at much larger length scales, i.e. in USAXS range, the spinodal peak can be observed and monitored to estimate the evolution of the phase separation. The correlation function shows features already seen in glasses and gels, as well as in other systems that show phase separation [126; 107; 121], namely a linear dependence of the decor-

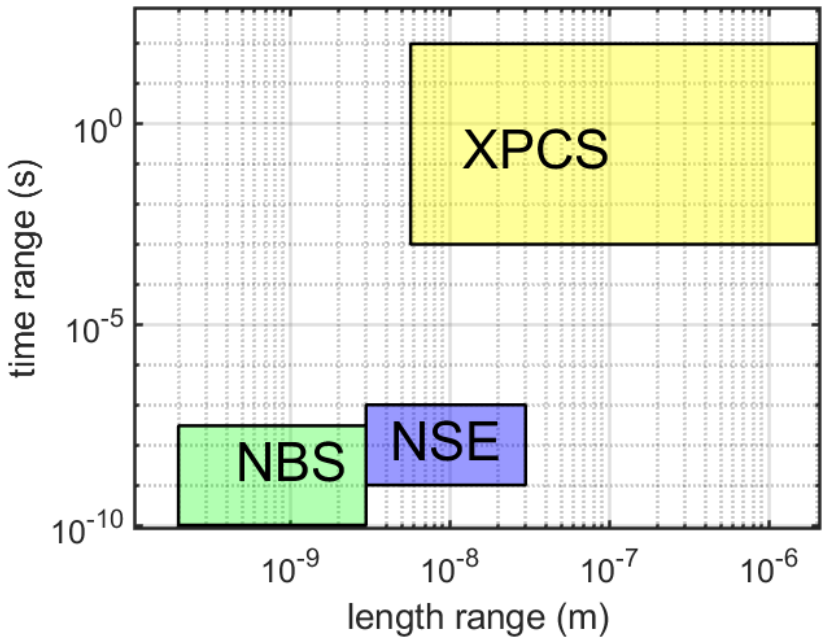

Figure 9.2: Summary of the measurements performed on the system in the phase separation region, indicating the time and length scales covered.

relation rate with q and an exponential growth of the decorrelation time with age, followed by a much slower growth. Two relaxation channels are present, the faster one corresponds to a decay in the correlation function which is the main contribution to the overall correlation function in the early stage of the spinodal decomposition, with a decay time that is larger at high temperature. The slower relaxation is visible only 30 s after the temperature quench and its decorrelation time is smaller at high temperature. Simulations show that this behavior can be reproduced via the Cahn-Hilliard equation if a strongly concentration-dependent mobility is introduced. This is confirmed by the data gathered at molecular length scale. Comparing the real space images and the correlation function we associate the fast mode to the dynamics of the fluctuation of the concentration and the second one to the dynamics of the domains, where the concentration is already elevated enough to be affected by the gel transition.

With this thesis, we show the possibility of measuring protein solution with XPCS. This novel method allowed us for the first time to probe the system in a range from micrometer to tens of nanometers in length scale. Furthermore, we deepened the knowledge on beam damage of protein solutions, such as the effects of the beam on the sample structure as well as the diffusion of its components. These insights can benefit future research using XPCS

on biological systems. By combining the different techniques, we successfully connected the kinetics and dynamics of phase separation with the molecular diffusion of the proteins via the Cahn-Hilliard equation. The model we used describes the kinetics and qualitatively the dynamics of the phase separation. In the micrometer length scales, we observed different types of diffusion in the single phase and in the phase separation region. However, a sharp transition between a classical phase separation and an arrested phase transition does not occur. This suggests a smooth transition between the liquid state to the gel state.

9.2 Perspectives

While we covered a very wide range of time and length scales, the question of which type of diffusion is present in the long time diffusion in the arrested phase separation state is not answered yet. The limit of the beam damage in the SAXS range is still present. With the investigation described in this thesis, we were able collect some information on the beam effects on the sample, but it was not possible to measure an unaffected diffusion yet. This problem could be solved with a change in setup configuration, where the distance between the sample and detector is increased, to increase the contrast and hence the signal to noise ratio. Another possible approach includes the addition of antioxidants to increase the value of the critical dose.

Until now the sample measured was a mixture Ig-PEG with a high PEG concentration, at which the phase separation becomes permanently arrested. A sample with lower PEG concentration instead induces a temporary gel and the phase separation in this case is arrested only for a limited time interval. In the literature, this behavior was associated to the visco-elastic properties of the sample [245]. The study of the dynamics of the system along with the addition of visco-elastic properties in the simulations can allow a deeper understanding of the underlining reason for this temporary arrest.

A possible follow up project would consist of the measurement of a more globular protein, such as apoferritin, with the goal of comparing the results for that system with the ones obtained in this thesis and isolate the effects of the non-sphericity of the protein both on protein length scales and on the microscopic phase behaviour.

This work has implications that go beyond the study of this specific protein system or in general of arrested phase transition. The possibility of measuring protein solution with XPCS gives access time and length scales which were not accessible before. This includes mea-

suring the long-time diffusion of protein gels and glasses on micrometer length scales with synchrotron radiation and the short-time diffusion of very crowded solutions, as it is usually the case in biological systems, with XFEL radiation.

List of Pubblications

- **Kinetics of Network Formation and Heterogeneous Dynamics of an Egg White Gel Revealed by Coherent X-Ray Scattering**

  Nafisa Begam, Anastasia Ragulskaya, Anita Girelli, Hendrik Rahmann, Sivasurender Chandran, Fabian Westermeier, Mario Reiser, Michael Sprung, Fajun Zhang, Christian Gutt, Frank Schreiber.

  Physical Review Letters 126 (9), 098001

  `https://doi.org/10.1103/PhysRevLett.126.098001`

- **Microscopic Dynamics of Liquid-Liquid Phase Separation and Domain Coarsening in a Protein Solution Revealed by X-Ray Photon Correlation Spectroscopy**

  Anita Girelli, Hendrik Rahmann, Nafisa Begam, Anastasia Ragulskaya, Mario Reiser, Sivasurender Chandran, Fabian Westermeier, Michael Sprung, Fajun Zhang, Christian Gutt, Frank Schreiber.

  Physical Review Letters 126 (13), 138004

  `https://doi.org/10.1103/PhysRevLett.126.138004`

- **Molecular Flexibility of Antibodies Preserved Even in the Dense Phase after Macroscopic Phase Separation**

  Anita Girelli, Christian Beck, Famke Baäuerle, Olga Matsarskaia, Ralph Maier, Fajun Zhang, Baohu Wu, Christian Lang, Orsolya Czakkel, Tilo Seydel, Frank Schreiber, Felix Roosen-Runge.

  Molecular pharmaceutics 18 (11), 4162-4169

  `https://doi.org/10.1021/acs.molpharmaceut.1c00555`

- **Interplay between Kinetics and Dynamics of Liquid–Liquid Phase Separation in a Protein Solution Revealed by Coherent X-ray Spectroscopy**

Anastasia Ragulskaya, Nafisa Begam, Anita Girelli, Hendrik Rahmann, Mario Reiser, Fabian Westermeier, Michael Sprung, Fajun Zhang, Christian Gutt, Frank Schreiber

The Journal of Physical Chemistry Letters 12 (30), 7085-7090

https://doi.org/10.1021/acs.jpclett.1c01940

- **Automated matching of two-time X-ray photon correlation maps from protein dynamics with Cahn-Hilliard type simulations using autoencoder networks**

  Sonja Timmermann, Vladimir Starostin, Anita Girelli, Anastasia Ragulskaya, Hendrik Rahmann, Mario Reiser, Nafisa Begam, Lisa Randolph, Michael Sprung, Fabian Westermeier, Fajun Zhang, Frank Schreiber and Christian Gutt

  Journal of Applied Crystallography (Accepted)

- **Resolving molecular diffusion and aggregation of antibody proteins with megahertz X-ray free-electron laser pulses**

  Mario Reiser, Anita Girelli, Anastasia Ragulskaya, Sudipta Das, Sharon Berkowicz, Maddalena Bin, Marjorie Ladd-Parada, Mariia Filianina, Hanna-Friederike Poggemann, Nafisa Begam, Mohammad Sayed Akhundzadeh, Sonja Timmermann, Lisa Randolph, Yuriy Chushkin, Tilo Seydel, Ulrike Boesenberg, Jörg Hallmann, Johannes Möller, Angel Rodriguez-Fernandez, Robert Rosca, Robert Schaffer, Markus Scholz, Roman Shayduk, Alexey Zozulya, Anders Madsen, Frank Schreiber, Fajun Zhang, Fivos Perakis, Christian Gutt

  Nature Communications (submitted)

Acknowledgments

Firstly, I would like to express my gratitude to my two supervisors, PD Dr. Fajun Zhang and Prof. Dr. Frank Schreiber, thank you for believing in me and giving me the chance to be part of this project. In particular, I would like to thank Prof. Dr. Frank Schreiber for encouraging me during the project and always offering his guidance in the perspective of the project, and PD Dr. Fajun Zhang for helping with the interpretations of results and technical discussions as well as organisational issues. I extent my gratitude also to Prof. Dr. Martin Oettel, who agreed to be the second reviewer of this thesis and for the discussions regarding the simulations.

A special thanks goes to Prof. Dr. Christian Gutt, who introduced me to the world of coherent x-rays, was always present when I needed advice and ready to help with discussions and suggestions during the experiments as well as for the analysis. I thank also Dr. Tilo Seydel for sharing his enthusiastic passion for quasi elastic neutron scattering and his knowledge in the data analysis. A special thank you goes also to Prof. Dr. Felix Roosen-Runge, with whom I shared many discussions on the interpretation of the data.

I would like to thank the beamline scientist who helped me during the experiments: Dr. Fabian Westermeier, Dr. Michael Sprung, Dr. Tilo Seydel, Dr. Baohu Wu, Dr. Christian Lang, Dr. Orsolya Czakkel, Dr. Olga Matsarskaia, Dr. Ulrike Boesenberg, Dr. Jörg Hallmann, Dr. Johannes Möller and Dr. Angel Rodriguez-Fernandez.

I would also like to thank all the collaborators, colleagues and students with whom I shared long days and nights at the beamtimes, it was exhausting but also very exciting, and I am grateful that we could do the experiments as well as share a beer (or a tea) afterwards. In particular thanks to Dr. Nafisa Begam, Dr. Mario Reiser, Dr. Hendrik Rahmann, Anastasia Ragulskaya, Sonja Timmermann, Hanna-Friederike Poggemann, Sebastian Retzbach, Dennis Gutmueller, Ralph Maier, Famke Bäuerle, Dr. Christian Beck, Maximillian Senft, Mohammad Sayed Akhundzadeh, Ahmed Al-Masoodi and Marvin Kowalski.

Thanks to all the proofreaders of this thesis for their patience: Alessandro Greco, Dr. Olga Matsarskaia, Dr. Christian Beck, Dr. Nafisa Begam, Hadra Banks, Ingrid Dax, Maximilian Senft, Ralph Maier, Zarah Weiss, and Irene Girelli.

I would like to thank all my colleagues and former colleagues in the group, for the their help and the nice time spent together. I really enjoyed my time there, and the support at work or during teaching and also the group activities.

Thanks to all my family. To my wife, Zarah Weiss, who was always there, both when I was excited and I was not stopping to talk about proteins or disappointed and complaining about the same proteins. Grazie alla parte italiana della mia famiglia: a Irene Girelli che mi ha sempre ascoltato e incoraggiato a continuare, a Nicola Girelli per avermi resa più testarda, a Maria Grazia Tosi e Luigi Girelli che mi hanno dato la possibilità di seguire la mia passione per la fisica e mi hanno sostenuta in questi anni e a Carla Girelli, che mi ha insegnato la perserveranza e l'accettazione. Thanks also to the German part of my family: Carsten Thielmann and Heidi Weiss, as well as Maximillian Weiss and Tatjana Weiss, for always being there whenever I needed anything.

Abbreviations

CHE Cahn-Hilliard Equation.

DESY Deutsches Elektronen-Synchrotron.

DLS Dynamic Light Scattering.

EISF Elastic Incoherent Structure Factor.

FWS Fixed Window Scan.

GISAXS Grazing Incidence Small Angle Scattering.

ILL Institut Laue-Langevin.

ISF Intermediate scattering function.

KWW Kohlrausch–Williams–Watts.

LLPS liquid-liquid phase separation.

MSD Mean-Squared Displacement.

MW Molecular Weight.

NBS Neutron Backscattering.

NSE Neutron Spin-Echo.

PCS Photon Correlation Spectroscopy.

PDB Protein Data Bank.

PEG Poly(ethylene glycol).

SANS Small Angle Neutron Scattering.

SAXS Small Angle X-Ray Scattering.

SLS Static Light Scattering.

TTC two-time correlation function.

USAXS Ultra Small Angle X-Ray Scattering.

UV-vis Ultraviolet–Visible Spectroscopy.

VSANS Very Small Angle Neutron Scattering.

XFEL X-Ray Free Electron Laser.

XPCS X-Ray Photon Correlation Spectroscopy.

Bibliography

[1] K. Binder, "Spinodal decomposition," in *Systems Far from Equilibrium*, pp. 76–90, Springer, 1980.

[2] J. Levelt, *How Fluids Unmix: Discoveries by the School of Van Der Waals and Kamerlingh Onnes*. No. 9069843579, Royal Netherlands Academy of Arts and Sciences, Amsterdam,, 2002-09-01 2002.

[3] L. Landau, "The theory of phase transitions," *Nature*, vol. 138, no. 3498, pp. 840–841, 1936.

[4] J. W. Cahn and J. E. Hilliard, "Free energy of a nonuniform system. i. interfacial free energy," *J. Chem. Phys*, vol. 28, no. 2, pp. 258–267, 1958.

[5] D. Bracha, M. T. Walls, and C. P. Brangwynne, "Probing and engineering liquid-phase organelles," *Nature biotechnology*, vol. 37, no. 12, pp. 1435–1445, 2019.

[6] E. B. Wilson, "The structure of protoplasm," *Science*, vol. 10, no. 237, pp. 33–45, 1899.

[7] C. P. Brangwynne, C. R. Eckmann, D. S. Courson, A. Rybarska, C. Hoege, J. Gharakhani, F. Jülicher, and A. A. Hyman, "Germline p granules are liquid droplets that localize by controlled dissolution/condensation," *Science*, vol. 324, no. 5935, pp. 1729–1732, 2009. 10.1126/science.1172046.

[8] J. A. Thomson, P. Schurtenberger, G. M. Thurston, and G. B. Benedek, "Binary liquid phase separation and critical phenomena in a protein/water solution," *Proceedings of the National Academy of Sciences*, vol. 84, no. 20, pp. 7079–7083, 1987.

[9] E. J. Shimshick and H. M. Mcconnell, "Lateral phase separation in phospholipid membranes," *Biochemistry*, vol. 12, no. 12, pp. 2351–2360, 1973.

[10] X. Su, J. A. Ditlev, E. Hui, W. Xing, S. Banjade, J. Okrut, D. S. King, J. Taunton, M. K. Rosen, and R. D. Vale, "Phase separation of signaling molecules promotes T cell receptor signal transduction," *Science*, vol. 352, no. 6285, pp. 595–599, 2016.

[11] C. J. Decker and R. Parker, "P-bodies and stress granules: possible roles in the control of translation and mrna degradation," *Cold Spring Harbor perspectives in biology*, vol. 4, no. 9, p. a012286, 2012.

[12] B. Wang, L. Zhang, T. Dai, Z. Qin, H. Lu, L. Zhang, and F. Zhou, "Liquid–liquid phase separation in human health and diseases," *Signal Transduction and Targeted Therapy*, vol. 6, no. 1, pp. 1–16, 2021.

[13] Q. Li, X. Wang, Z. Dou, W. Yang, B. Huang, J. Lou, and Z. Zhang, "Protein databases related to liquid–liquid phase separation," *International Journal of Molecular Sciences*, vol. 21, no. 18, p. 6796, 2020.

[14] Y. Shin and C. P. Brangwynne, "Liquid phase condensation in cell physiology and disease," *Science*, vol. 357, no. 6357, p. eaaf4382, 2017.

[15] S. Elbaum-Garfinkle, "Matter over mind: Liquid phase separation and neurodegeneration," *Journal of Biological Chemistry*, vol. 294, no. 18, pp. 7160–7168, 2019.

[16] Y. Shin, J. Berry, N. Pannucci, M. P. Haataja, J. E. Toettcher, and C. P. Brangwynne, "Spatiotemporal control of intracellular phase transitions using light-activated optodroplets," *Cell*, vol. 168, no. 1, pp. 159–171.e14, 2017.

[17] C. P. Brangwynne, P. Tompa, and R. V. Pappu, "Polymer physics of intracellular phase transitions," *Nature Physics*, vol. 11, no. 11, pp. 899–904, 2015.

[18] A. Stradner and P. Schurtenberger, "Potential and limits of a colloid approach to protein solutions," *Soft Matter*, vol. 16, no. 2, pp. 307–323, 2020.

[19] V. J. Anderson and H. N. W. Lekkerkerker, "Insights into phase transition kinetics from colloid science," *Nature*, vol. 416, no. 6883, pp. 811–815, 2002.

[20] R. Joosten, "X-ray structure re-refinement. combining old data with new methods for better structural bioinformatics," *Electronic Notes in Theoretical Computer Science - ENTCS*, 01 2010.

[21] J. Israelachvili, *Intermolecular and Surface Forces*. Academic Press, London, 1991.

[22] S. Asakura and F. Oosawa, "On Interaction between Two Bodies Immersed in a Solution of Macromolecules," *The Journal of Chemical Physics*, vol. 22, pp. 1255–1256, 1954.

[23] A. Kulkarni and C. Zukoski, "Depletion interactions and protein crystallization," *Journal of Crystal Growth*, vol. 232, no. 1, pp. 156–164, 2001. Proceedings of the Eighth International Conference on Crystalliza tion of Biological Macromolecules.

[24] K. J. Mutch, J. S. van Duijneveldt, and J. Eastoe, "Colloid–polymer mixtures in the protein limit," *Soft Matter*, vol. 3, no. 2, pp. 155–167, 2007.

[25] M. G. Noro and D. Frenkel, "Extended corresponding-states behavior for particles with variable range attractions," *The Journal of Chemical Physics*, vol. 113, no. 8, pp. 2941–2944, 2000.

[26] F. Platten, N. E. Valadez-Pérez, R. Castañeda Priego, and S. U. Egelhaaf, "Extended law of corresponding states for protein solutions," *The Journal of Chemical Physics*, vol. 142, p. 174905, 2015.

[27] M. Muschol and F. Rosenberger, "Liquid–liquid phase separation in supersaturated lysozyme solutions and associated precipitate formation/crystallization," *The Journal of Chemical Physics*, vol. 107, no. 6, pp. 1953–1962, 1997.

[28] D. Fusco and P. Charbonneau, "Soft matter perspective on protein crystal assembly," *Colloids and Surfaces B: Biointerfaces*, vol. 137, pp. 22–31, 2016.

[29] P. R. ten Wolde and D. Frenkel, "Enhancement of protein crystal nucleation by critical density fluctuations," *Science*, vol. 277, no. 5334, pp. 1975–1978, 1997.

[30] Y. Wang, A. Lomakin, R. F. Latypov, and G. B. Benedek, "Phase separation in solutions of monoclonal antibodies and the effect of human serum albumin," *Proceedings of the National Academy of Sciences*, vol. 108, no. 40, pp. 16606–16611, 2011.

[31] S. Da Vela, C. Exner, R. S. Schäufele, J. Möller, Z. Fu, F. Zhang, and F. Schreiber, "Arrested and temporarily arrested states in a protein-polymer mixture studied by USAXS and VSANS," *Soft Matter*, vol. 13, no. 46, pp. 8756–8765, 2017.

[32] J. K. G. Dhont, *An Introduction to Dynamics of Colloids*. Elsevier Science B. V., 1996.

[33] A. Gast, C. Hall, and W. Russel, "Polymer-induced phase separations in nonaqueous colloidal suspensions," *Journal of Colloid and Interface Science*, vol. 96, no. 1, pp. 251–267, 1983.

[34] D. Sappelt and J. Jäckle, "Computer simulation study of phase separation in a binary mixture with a glass-forming component," *Physica A: Statistical Mechanics and its Applications*, vol. 240, no. 3, pp. 453–479, 1997.

[35] F. Sciortino, R. Bansil, H. E. Stanley, and P. Alstrøm, "Interference of phase separation and gelation: A zeroth-order kinetic model," *Physical Review E*, vol. 47, no. 6, pp. 4615–4618, 1993.

[36] H. Tanaka, "Coarsening mechanisms of droplet spinodal decomposition in binary fluid mixtures," *The Journal of Chemical Physics*, vol. 105, no. 22, pp. 10099–10114, 1996.

[37] H. Tanaka, "New mechanisms of droplet coarsening in phase-separating fluid mixtures," *The Journal of Chemical Physics*, vol. 107, no. 9, pp. 3734–3737, 1997.

[38] A. J. Wagner and J. M. Yeomans, "Breakdown of scale invariance in the coarsening of phase-separating binary fluids," *Physical Review Letters*, vol. 80, no. 7, p. 1429, 1998.

[39] H. Tanaka and Y. Nishikawa, "Viscoelastic phase separation of protein solutions," *Physical Review Letters*, vol. 95, p. 078103, 2005.

[40] C. P. Royall, M. A. Faers, S. L. Fussell, and J. E. Hallett, "Real space analysis of colloidal gels: triumphs, challenges and future directions," *Journal of Physics: Condensed Matter*, vol. 33, no. 45, p. 453002, 2021.

[41] V. Testard, L. Berthier, and W. Kob, "Intermittent dynamics and logarithmic domain growth during the spinodal decomposition of a glass-forming liquid," *The Journal of Chemical Physics*, vol. 140, no. 16, p. 164502, 2014.

[42] E. Zaccarelli, "Colloidal gels: equilibrium and non-equilibrium routes," *Journal of Physics: Condensed Matter*, vol. 19, no. 32, p. 323101, 2007.

[43] W. C. K. Poon, A. D. Pirie, and P. N. Pusey, "Gelation in colloid–polymer mixtures," *Faraday Discussions*, vol. 101, pp. 65–76, 1995.

[44] W. Poon, "The physics of a model colloidal-polymer mixture," *Journal of Physics: Condensed Matter*, vol. 14, pp. R859–R880, 2002.

[45] P. J. Lu, E. Zaccarelli, F. Ciulla, A. B. Schofield, F. Sciortino, and D. A. Weitz, "Gelation of particles with short-range attraction," *Nature*, vol. 453, no. 7194, pp. 499–503, 2008.

[46] G. Foffi, C. D. Michele, F. Sciortino, and P. Tartaglia, "Scaling of dynamics with the range of interaction in short-range attractive colloids," *Physical Review Letters*, vol. 94, no. 7, p. 078301, 2005.

[47] A. M. Puertas, M. Fuchs, and M. E. Cates, "Competition between glass transition and liquid–gas separation in attracting colloids," *Journal of Physics: Condensed Matter*, vol. 19, no. 20, p. 205140, 2007.

[48] D. Sappelt and J. Jäckle, "Spinodal decomposition with formation of a glassy phase," *EPL (Europhysics Letters)*, vol. 37, no. 1, p. 13, 1997.

[49] J. Bergenholtz, W. C. Poon, and M. Fuchs, "Gelation in model colloid- polymer mixtures," *Langmuir*, vol. 19, no. 10, pp. 4493–4503, 2003.

[50] M. E. Cates, M. Fuchs, K. Kroy, W. C. Poon, and A. M. Puertas, "Theory and simulation of gelation, arrest and yielding in attracting colloids," *Journal of Physics: Condensed Matter*, vol. 16, no. 42, p. S4861, 2004.

[51] M. Tateno and H. Tanaka, "Power-law coarsening in network-forming phase separation governed by mechanical relaxation," *Nature communications*, vol. 12, no. 1, pp. 1–12, 2021.

[52] M. Tateno, T. Yanagishima, and H. Tanaka, "Microscopic structural origin behind slowing down of colloidal phase separation approaching gelation," *The Journal of Chemical Physics*, vol. 156, no. 8, p. 084904, 2022.

[53] F. Cardinaux, T. Gibaud, A. Stradner, and P. Schurtenberger, "Interplay between spinodal decomposition and glass formation in proteins exhibiting short-range attractions," *Physical Review Letters*, vol. 99, p. 118301, 2007.

[54] T. Gibaud, F. Cardinaux, J. Bergenholtz, A. Stradner, and P. Schurtenberger, "Phase separation and dynamical arrest for particles interacting with mixed potentials — the case of globular proteins revisited," *Soft Matter*, vol. 7, pp. 857–860, 2011.

[55] P. Schurtenberger, R. A. Chamberlin, G. M. Thurston, J. A. Thomson, and G. B. Benedek, "Observation of critical phenomena in a protein-water solution," *Physical Review Letters*, vol. 63, no. 19, pp. 2064–2067, 1989.

[56] S. Bucciarelli, L. Casal-Dujat, C. De Michele, F. Sciortino, J. Dhont, J. Bergenholtz, B. Farago, P. Schurtenberger, and A. Stradner, "Unusual dynamics of concentration fluctuations in solutions of weakly attractive globular proteins," *J. Phys. Chem. Lett*, vol. 6, no. 22, pp. 4470–4474, 2015.

[57] S. Wegmann, B. Eftekharzadeh, K. Tepper, K. M. Zoltowska, R. E. Bennett, S. Dujardin, P. R. Laskowski, D. MacKenzie, T. Kamath, and C. Commins, "Tau protein liquid-liquid phase separation can initiate tau aggregation," *The EMBO journal*, vol. 37, no. 7, p. e98049, 2018.

[58] S. Bhat, R. Tuinier, and P. Schurtenberger, "Spinodal decomposition in a food colloid–biopolymer mixture: evidence for a linear regime," *Journal of Physics: Condensed Matter*, vol. 18, no. 26, p. L339, 2006.

[59] N. Mahmoudi and A. Stradner, "Making food protein gels via an arrested spinodal decomposition," *The Journal of Physical Chemistry B*, vol. 119, no. 50, pp. 15522–15529, 2015.

[60] A. Banc, J. Pincemaille, S. Costanzo, E. Chauveau, M.-S. Appavou, M.-H. Morel, P. Menut, and L. Ramos, "Phase separation dynamics of gluten protein mixtures," *Soft Matter*, vol. 15, no. 30, pp. 6160–6170, 2019.

[61] S. Da Vela, M. K. Braun, A. Dörr, A. Greco, J. Möller, Z. Fu, F. Zhang, and F. Schreiber, "Kinetics of liquid-liquid phase separation in protein solutions exhibiting LCST phase behavior studied by time-resolved USAXS and VSANS," *Soft Matter*, vol. 12, no. 46, pp. 9334–9341, 2016.

[62] O. Matsarskaia, S. Da Vela, A. Mariani, Z. Fu, F. Zhang, and F. Schreiber, "Phase-Separation Kinetics in Protein-Salt Mixtures with Compositionally Tuned Interactions," *The Journal of Physical Chemistry B*, vol. 123, pp. 1913–1919, 2019.

[63] T. Gibaud, N. Mahmoudi, J. Oberdisse, P. Lindner, J. S. Pedersen, C. L. P. Oliveira, A. Stradner, and P. Schurtenberger, "New routes to food gels and glasses," *Faraday Discussions*, vol. 158, p. 267, 2012.

[64] R. Mezzenga, P. Schurtenberger, A. Burbidge, and M. Michel, "Understanding foods as soft materials.," *Nature Materials*, vol. 4, pp. 729–740, 2005.

[65] R. Mezzenga and P. Fischer, "The self-assembly, aggregation and phase transitions of food protein systems in one, two and three dimensions," *Reports on Progress in Physics*, vol. 76, no. 4, p. 046601, 2013.

[66] N. A. Verhaegh, D. Asnaghi, H. N. Lekkerkerker, M. Giglio, and L. Cipelletti, "Transient gelation by spinodal decomposition in colloid-polymer mixtures," *Physica A: Statistical Mechanics and its Applications*, vol. 242, no. 1-2, pp. 104–118, 1997.

[67] B. Alberts, A. Johnson, J. Lewis, M. Rafi, K. Roberts, and P. Walter, *Molecular Biology of the Cell*. Garland Science, Taylor & Francis Group, New York, 5th revised ed., 2008.

[68] M. Grimaldo, F. Roosen-Runge, F. Zhang, F. Schreiber, and T. Seydel, "Dynamics of proteins in solution," *Quarterly Reviews of Biophysics*, vol. 52, 2019.

[69] A. R. Altenberger, M. Tirrell, and J. S. Dahler, "Hydrodynamic screening and particle dynamics in porous media, semidilute polymer solutions and polymer gels," *The Journal of Chemical Physics*, vol. 84, no. 9, pp. 5122–5130, 1986.

[70] J.-M. Petit, B. Roux, X. Zhu, and P. Macdonald, "A new physical model for the diffusion of solvents and solute probes in polymer solutions," *Macromolecules*, vol. 29, no. 18, pp. 6031–6036, 1996.

[71] B. Amsden, "Modeling solute diffusion in aqueous polymer solutions," *Polymer*, vol. 43, no. 5, pp. 1623–1630, 2002.

[72] B. Amsden, "An obstruction-scaling model for diffusion in homogeneous hydrogels," *Macromolecules*, vol. 32, no. 3, pp. 874–879, 1999.

[73] D. M. Weinreich, S. Sivapalasingam, T. Norton, S. Ali, H. Gao, R. Bhore, J. Xiao, A. T. Hooper, J. D. Hamilton, B. J. Musser, *et al.*, "Regen-cov antibody combination and outcomes in outpatients with covid-19," *New England Journal of Medicine*, 2021.

[74] S. Jiang, C. Hillyer, and L. Du, "Neutralizing antibodies against sars-cov-2 and other human coronaviruses," *Trends in immunology*, vol. 41, no. 5, pp. 355–359, 2020.

[75] O. Shpilberg and C. Jackisch, "Subcutaneous administration of rituximab (mabthera) and trastuzumab (herceptin) using hyaluronidase," *British Journal of Cancer*, vol. 109, no. 6, pp. 1556–1561, 2013.

[76] D. Leveque, "Subcutaneous administration of anticancer agents," *Anticancer research*, vol. 34, no. 4, pp. 1579–1586, 2014.

[77] C. Jackisch, V. Müller, C. Maintz, S. Hell, and B. Ataseven, "Subcutaneous administration of monoclonal antibodies in oncology," *Geburtshilfe und Frauenheilkunde*, vol. 74, no. 4, p. 343, 2014.

[78] P. Garidel, A. B. Kuhn, L. V. Schäfer, A. R. Karow-Zwick, and M. Blech, "High-concentration protein formulations: How high is high?," *European Journal of Pharmaceutics and Biopharmaceutics*, vol. 119, pp. 353–360, 2017.

[79] A. L. Daugherty and R. J. Mrsny, "Formulation and delivery issues for monoclonal antibody therapeutics," *Advanced Drug Delivery Reviews*, vol. 58, no. 5, pp. 686 – 706, 2006. Engineered antibody therapeutics.

[80] R. Harris, S. Shire, and C. M. Winter, "Commercial manufacturing scale formulation and analytical characterization of therapeutic recombinant antibodies," *Drug Development Research*, vol. 61, 2004.

[81] M. Kastelic and V. Vlachy, "Theory for the liquid–liquid phase separation in aqueous antibody solutions," *The Journal of Physical Chemistry B*, vol. 122, no. 21, pp. 5400–5408, 2018.

[82] Y. Wang, A. Lomakin, R. F. Latypov, J. P. Laubach, T. Hideshima, P. G. Richardson, N. C. Munshi, K. C. Anderson, and G. B. Benedek, "Phase transitions in human igg solutions," *The Journal of Chemical Physics*, vol. 139, no. 12, p. 121904, 2013.

[83] S. Da Vela, F. Roosen-Runge, M. W. A. Skoda, R. M. J. Jacobs, T. Seydel, H. Frielinghaus, M. Sztucki, R. Schweins, F. Zhang, and F. Schreiber, "Effective interactions and colloidal stability of bovine γ-globulin in solution," *The Journal of Physical Chemistry B*, vol. 121, pp. 5759–5769, 2017.

[84] K. Reiche, J. Hartl, A. Blume, and P. Garidel, "Liquid-liquid phase separation of a monoclonal antibody at low ionic strength: Influence of anion charge and concentration," *Biophysical Chemistry*, vol. 220, pp. 7–19, 2017.

[85] N. Skar-Gislinge, M. Ronti, T. Garting, C. Rischel, P. Schurtenberger, E. Zaccarelli, and A. Stradner, "A colloid approach to self-assembling antibodies," *Molecular Pharmaceutics*, vol. 16, no. 6, pp. 2394–2404, 2019. PMID: 31059276.

[86] W. G. Lilyestrom, S. J. Shire, and T. M. Scherer, "Influence of the cosolute environment on IgG solution structure analyzed by small-angle X-ray scattering," *Journal of Physical Chemistry B*, vol. 116, no. 32, pp. 9611–9618, 2012.

[87] L. Nicoud, M. Sozo, P. Arosio, A. Yates, E. Norrant, and M. Morbidelli, "Role of cosolutes in the aggregation kinetics of monoclonal antibodies," *The Journal of Physical Chemistry B*, vol. 118, no. 41, pp. 11921–11930, 2014. PMID: 25243487.

[88] D. Corbett, M. Hebditch, R. Keeling, P. Ke, S. Ekizoglou, P. Sarangapani, J. Pathak, C. F. Van Der Walle, S. Uddin, C. Baldock, *et al.*, "Coarse-grained modeling of antibodies from small-angle scattering profiles," *The Journal of Physical Chemistry B*, vol. 121, no. 35, pp. 8276–8290, 2017.

[89] H. Inouye, D. Houde, D. B. Temel, and L. Makowski, "Utility of solution X-ray scattering for the development of antibody biopharmaceuticals," *Journal of Pharmaceutical Sciences*, vol. 105, no. 11, pp. 3278–3289, 2016.

[90] C. Calero-Rubio, A. Saluja, and C. J. Roberts, "Coarse-grained antibody models for "weak" protein-protein interactions from low to high concentrations," *The Journal of Physical Chemistry B*, vol. 120, no. 27, pp. 6592–6605, 2016.

[91] D. Arzenšek, D. Kuzman, and R. Podgornik, "Colloidal interactions between monoclonal antibodies in aqueous solutions," *Journal of colloid and interface science*, vol. 384, no. 1, pp. 207–216, 2012.

[92] S. Yadav, A. Sreedhara, S. Kanai, J. Liu, S. Lien, H. Lowman, D. S. Kalonia, and S. J. Shire, "Establishing a link between amino acid sequences and self-associating and viscoelastic behavior of two closely related monoclonal antibodies," *Pharmaceutical research*, vol. 28, no. 7, pp. 1750–1764, 2011.

[93] S. Yadav, T. M. Laue, D. S. Kalonia, S. N. Singh, and S. J. Shire, "The influence of charge distribution on self-association and viscosity behavior of monoclonal antibody solutions," *Molecular Pharmaceutics*, vol. 9, no. 4, pp. 791–802, 2012.

[94] B. J. Dear, A. Chowdhury, J. J. Hung, C. A. Karouta, K. Ramachandran, M. P. Nieto, L. R. Wilks, A. Sharma, T. Y. Shay, J. K. Cheung, T. M. Truskett, and K. P. Johnston, "Relating collective diffusion, protein–protein interactions, and viscosity of highly concentrated monoclonal antibodies through dynamic light scattering," *Industrial & Engineering Chemistry Research*, vol. 58, no. 50, pp. 22456–22471, 2019.

[95] A. Lanzaro, A. Roche, N. Sibanda, D. Corbett, P. Davis, M. Shah, J. A. Pathak, S. Uddin, C. F. van der Walle, X.-F. Yuan, *et al.*, "Cluster percolation causes shear thinning behavior in concentrated solutions of monoclonal antibodies," *Molecular Pharmaceutics*, vol. 18, no. 7, pp. 2669–2682, 2021.

[96] M. A. Pindrus, S. J. Shire, S. Yadav, and D. S. Kalonia, "The effect of low ionic strength on diffusion and viscosity of monoclonal antibodies," *Molecular Pharmaceutics*, vol. 15, no. 8, pp. 3133–3142, 2018.

[97] M. A. Woldeyes, W. Qi, V. I. Razinkov, E. M. Furst, and C. J. Roberts, "How well do low- and high-concentration protein interactions predict solution viscosities of monoclonal antibodies?," *Journal of Pharmaceutical Sciences*, vol. 108, no. 1, pp. 142–154, 2019.

[98] M. A. Woldeyes, L. L. Josephson, D. L. Leiske, W. J. Galush, C. J. Roberts, and E. M. Furst, "Viscosities and protein interactions of bispecific antibodies and their monospecific mixtures," *Molecular Pharmaceutics*, vol. 15, no. 10, pp. 4745–4755, 2018.

[99] M. Grimaldo, F. Roosen-Runge, F. Zhang, T. Seydel, and F. Schreiber, "Diffusion and dynamics of γ- globulin in crowded aqueous solutions," *The Journal of Physical Chemistry B*, vol. 118, pp. 7203–7209, 2014.

[100] L. R. Stingaciu, O. Ivanova, M. Ohl, R. Biehl, and D. Richter, "Fast antibody fragment motion: flexible linkers act as entropic spring," *Scientific Reports*, vol. 6, 2016.

[101] Y. Alpert, L. Cser, B. Faragó, F. Franěk, F. Mezei, and Y. M. Ostanevich, "Segmental flexibility in pig immunoglobulin g studied by neutron spin-echo technique," *Biopolymers*, vol. 24, no. 9, pp. 1769–1784, 1985.

[102] J. J. Hung, W. F. Zeno, A. A. Chowdhury, B. J. Dear, K. Ramachandran, M. P. Nieto, T. Y. Shay, C. A. Karouta, C. C. Hayden, J. K. Cheung, *et al.*, "Self-diffusion of a highly concentrated monoclonal antibody by fluorescence correlation spectroscopy: insight into protein–protein interactions and self-association," *Soft matter*, vol. 15, no. 33, pp. 6660–6676, 2019.

[103] W. G. Lilyestrom, S. Yadav, S. J. Shire, and T. M. Scherer, "Monoclonal antibody self-association, cluster formation, and rheology at high concentrations," *The Journal of Physical Chemistry B*, vol. 117, no. 21, pp. 6373–6384, 2013.

[104] S. von Bülow, M. Siggel, M. Linke, and G. Hummer, "Dynamic cluster formation determines viscosity and diffusion in dense protein solutions," *Proceedings of the National Academy of Sciences*, vol. 116, no. 20, pp. 9843–9852, 2019.

[105] J. Rouwhorst, C. Ness, S. Stoyanov, A. Zaccone, and P. Schall, "Nonequilibrium continuous phase transition in colloidal gelation with short-range attraction," *Nature communications*, vol. 11, no. 1, pp. 1–8, 2020.

[106] C. Patrick Royall, S. R. Williams, T. Ohtsuka, and H. Tanaka, "Direct observation of a local structural mechanism for dynamic arrest," *Nature materials*, vol. 7, no. 7, pp. 556–561, 2008.

[107] S. Manley, H. Wyss, K. Miyazaki, J. Conrad, V. Trappe, L. Kaufman, D. Reichman, and D. Weitz, "Glasslike arrest in spinodal decomposition as a route to colloidal gelation," *Physical review letters*, vol. 95, no. 23, p. 238302, 2005.

[108] P. G. De Gennes, "Liquid dynamics and inelastic scattering of neutrons," *Physica*, vol. 25, no. 7-12, pp. 825–839, 1959.

[109] N. Mahmoudi and A. Stradner, "Structural arrest and dynamic localization in biocolloidal gels," *Soft matter*, vol. 13, no. 26, pp. 4629–4635, 2017.

[110] P. Pusey, A. Pirie, and W. Poon, "Dynamics of colloid-polymer mixtures," *Physica A: Statistical Mechanics and its Applications*, vol. 201, no. 1-3, pp. 322–331, 1993.

[111] F. Sciortino, "One liquid, two glasses," *Nature materials*, vol. 1, no. 3, pp. 145–146, 2002.

[112] A. P. Eberle, N. J. Wagner, and R. Castañeda-Priego, "Dynamical arrest transition in nanoparticle dispersions with short-range interactions," *Physical Review Letters*, vol. 106, no. 10, p. 105704, 2011.

[113] A. P. Eberle, R. Castaneda-Priego, J. M. Kim, and N. J. Wagner, "Dynamical arrest, percolation, gelation, and glass formation in model nanoparticle dispersions with thermoreversible adhesive interactions," *Langmuir*, vol. 28, no. 3, pp. 1866–1878, 2012.

[114] F. Varrato, L. Di Michele, M. Belushkin, N. Dorsaz, S. H. Nathan, E. Eiser, and G. Foffi, "Arrested demixing opens route to bigels," *Proceedings of the National Academy of Sciences*, vol. 109, no. 47, pp. 19155–19160, 2012.

[115] G. Brown, P. A. Rikvold, M. Sutton, and M. Grant, "Speckle from phase-ordering systems," *Physical Review E*, vol. 56, no. 6, p. 6601, 1997.

[116] G. Brown, P. A. Rikvold, M. Sutton, and M. Grant, "Evolution of speckle during spinodal decomposition," *Physical Review E*, vol. 60, no. 5, p. 5151, 1999.

[117] F. Livet, F. Bley, R. Caudron, E. Geissler, D. Abernathy, C. Detlefs, G. Grübel, and M. Sutton, "Kinetic evolution of unmixing in an alli alloy using X-ray intensity fluctuation spectroscopy," *Physical Review E*, vol. 63, no. 3, p. 036108, 2001.

[118] K. Ludwig, F. Livet, F. Bley, J.-P. Simon, R. Caudron, D. Le Bolloc'h, and A. Moussaid, "X-ray intensity fluctuation spectroscopy studies of ordering kinetics in a cu-pd alloy," *Physical Review B*, vol. 72, no. 14, p. 144201, 2005.

[119] A. Malik, A. R. Sandy, L. B. Lurio, G. B. Stephenson, S. G. J. Mochrie, I. McNulty, and M. Sutton, "Coherent X-ray study of fluctuations during domain coarsening," *Physical Review Letters*, vol. 81, no. 26, pp. 5832–5835, 1998.

[120] A. Fluerasu, M. Sutton, and E. M. Dufresne, "X-ray intensity fluctuation spectroscopy studies on phase-ordering systems," *Physical Review Letters*, vol. 94, p. 055501, Feb 2005.

[121] Y. Gao, J. Kim, and M. E. Helgeson, "Microdynamics and arrest of coarsening during spinodal decomposition in thermoreversible colloidal gels," *Soft matter*, vol. 11, no. 32, pp. 6360–6370, 2015.

[122] A. Duri and L. Cipelletti, "Length scale dependence of dynamical heterogeneity in a colloidal fractal gel," *EPL (Europhysics Letters)*, vol. 76, no. 5, p. 972, 2006.

[123] S. Bucciarelli, J. S. Myung, B. Farago, S. Das, G. A. Vliegenthart, O. Holderer, R. G. Winkler, P. Schurtenberger, G. Gompper, and A. Stradner, "Dramatic influence of patchy attractions on short-time protein diffusion under crowded conditions," *Science Advances*, vol. 2, p. e1601432, 2016.

[124] B. M. Fine, J. Pande, A. Lomakin, O. O. Ogun, and G. B. Benedek, "Dynamic critical phenomena in aqueous protein solutions," *Physical Review Letters*, vol. 74, no. 1, pp. 198–201, 1995.

[125] H. Burstyn and J. Sengers, "Decay rate of critical concentration fluctuations in a binary liquid," *Physical Review A*, vol. 25, no. 1, p. 448, 1982.

[126] A.-M. Philippe, L. Cipelletti, and D. Larobina, "Mucus as an arrested phase separation gel," *Macromolecules*, vol. 50, no. 20, pp. 8221–8230, 2017.

[127] S. Ray, N. Singh, R. Kumar, K. Patel, S. Pandey, D. Datta, J. Mahato, R. Panigrahi, A. Navalkar, S. Mehra, *et al.*, "α-synuclein aggregation nucleates through liquid–liquid phase separation," *Nature chemistry*, vol. 12, no. 8, pp. 705–716, 2020.

[128] M. Sutton, S. Mochrie, T. Greytak, S. Nagler, L. Berman, G. Held, and G. Stephenson, "Observation of speckle by diffraction with coherent X-rays," *Nature*, vol. 352, no. 6336, pp. 608–610, 1991.

[129] F. Lehmkühler, W. Roseker, and G. Grübel, "From femtoseconds to hours—measuring dynamics over 18 orders of magnitude with coherent X-rays," *Applied Sciences*, vol. 11, no. 13, 2021.

[130] B. Ruta, E. Pineda, and Z. Evenson, "Relaxation processes and physical aging in metallic glasses," *Journal of Physics: Condensed Matter*, vol. 29, no. 50, p. 503002, 2017.

[131] J. Verwohlt, M. Reiser, L. Randolph, A. Matic, L. A. Medina, A. Madsen, M. Sprung, A. Zozulya, and C. Gutt, "Low dose X-ray speckle visibility spectroscopy reveals nanoscale dynamics in radiation sensitive ionic liquids," *Physical Review Letters*, vol. 120, no. 16, p. 168001, 2018.

[132] A. Madsen, B. Struth, and G. Grübel, "Structure and dynamics of a free liquid crystal surface at the n-to-sma phase transition," *Physica B: Condensed Matter*, vol. 336, no. 1, pp. 216–221, 2003. Proceedings of the Seventh International Conference on Surface X-ray and Neutron Scattering.

[133] A. Madsen, L. L. Robert, G. Hongyu, S. Michael, and C. Orsolya, "Beyond simple exponential correlation functions and equilibrium dynamics in X-ray photon correlation spectroscopy," *New J. Phys.*, vol. 12, no. 5, p. 055001, 2010.

[134] A. Takahara, Y. Higaki, T. Hirai, and R. Ishige, "Application of synchrotron radiation X-ray scattering and spectroscopy to soft matter," *Polymers*, vol. 12, no. 7, p. 1624, 2020.

[135] F. Westermeier, B. Fischer, W. Roseker, G. Grübel, G. Nägele, and M. Heinen, "Structure and short-time dynamics in concentrated suspensions of charged colloids," *The Journal of Chemical Physics*, vol. 137, no. 11, p. 114504, 2012.

[136] N. Begam, A. Ragulskaya, A. Girelli, H. Rahmann, S. Chandran, F. Westermeier, M. Reiser, M. Sprung, F. Zhang, C. Gutt, *et al.*, "Kinetics of network formation and heterogeneous dynamics of an egg white gel revealed by coherent X-ray scattering," *Physical Review Letters*, vol. 126, no. 9, p. 098001, 2021.

[137] Y. Chen, S. A. Rogers, S. Narayanan, J. L. Harden, and R. L. Leheny, "Microscopic dynamics of stress relaxation in a nanocolloidal soft glass," *Physical Review Materials*, vol. 4, no. 3, p. 035602, 2020.

[138] T. Narayanan, M. Sztucki, T. Zinn, J. Kieffer, A. Homms-Puron, J. Gorini, P. Van Vaerenbergh, and P. Boesecke, "Performance of the time-resolved ultra-small-angle X-ray scattering beamline with the Extremely Brilliant Source," *Journal of Applied Crystallography*, vol. 55, pp. 98–111, Feb 2022.

[139] T. Thurn-Albrecht, W. Steffen, A. Patkowski, G. Meier, E. W. Fischer, G. Grübel, and D. Abernathy, "Photon correlation spectroscopy of colloidal palladium using a coherent X-ray beam," *Physical Review Letters*, vol. 77, no. 27, p. 5437, 1996.

[140] D. Orsi, A. Fluerasu, A. Moussaïd, F. Zontone, L. Cristofolini, and A. Madsen, "Dynamics in dense hard-sphere colloidal suspensions," *Physical Review E*, vol. 85, no. 1, p. 011402, 2012.

[141] M. Spannuth, S. Mochrie, S. Peppin, and J. Wettlaufer, "Dynamics of colloidal particles in ice," *The Journal of Chemical Physics*, vol. 135, no. 22, p. 224706, 2011.

[142] T. Zinn, L. Sharpnack, and T. Narayanan, "Phoretic dynamics of colloids in a phase separating critical liquid mixture," *Physical Review Research*, vol. 2, no. 3, p. 033177, 2020.

[143] A. Pal, T. Zinn, M. A. Kamal, T. Narayanan, and P. Schurtenberger, "Anomalous dynamics of magnetic anisotropic colloids studied by xpcs," *Small*, vol. 14, no. 46, p. 1802233, 2018.

[144] R. Dattani, E. F. Semeraro, and T. Narayanan, "Phoretic motion of colloids in a phase separating medium," *Soft Matter*, vol. 13, no. 15, pp. 2817–2822, 2017.

[145] R. L. Leheny, "Xpcs: Nanoscale motion and rheology," *Current Opinion in Colloid & Interface Science*, vol. 17, no. 1, pp. 3–12, 2012.

[146] P. N. Pusey and W. van Megen, "Phase behaviour of concentrated suspensions of nearly hard colloidal spheres," *Nature*, vol. 320, no. 6060, pp. 340–342, 1986.

[147] E. Zaccarelli, P. J. Lu, F. Ciulla, D. A. Weitz, and F. Sciortino, "Gelation as arrested phase separation in short-ranged attractive colloid–polymer mixtures," *Journal of Physics: Condensed Matter*, vol. 20, no. 49, p. 494242, 2008.

[148] H. Guo, S. Ramakrishnan, J. L. Harden, and R. L. Leheny, "Gel formation and aging in weakly attractive nanocolloid suspensions at intermediate concentrations," *The Journal of Chemical Physics*, vol. 135, no. 15, p. 154903, 2011.

[149] L. Cipelletti, S. Manley, R. C. Ball, and D. A. Weitz, "Universal aging features in the restructuring of fractal colloidal gels," *Physical Review Letters*, vol. 84, no. 10, pp. 2275–2278, 2000.

[150] L. Cipelletti, L. Ramos, S. Manley, E. Pitard, D. A. Weitz, E. E. Pashkovski, and M. Johansson, "Universal non-diffusive slow dynamics in aging soft matter," *Faraday discussions*, vol. 123, pp. 237–251, 2003.

[151] L. Frenzel, F. Lehmkühler, I. Lokteva, S. Narayanan, M. Sprung, and G. Grübel, "Anomalous dynamics of concentrated silica-pnipam nanogels," *The Journal of Physical Chemistry Letters*, vol. 10, no. 17, pp. 5231–5236, 2019.

[152] B. Chung, S. Ramakrishnan, R. Bandyopadhyay, D. Liang, C. Zukoski, J. Harden, and R. Leheny, "Microscopic dynamics of recovery in sheared depletion gels," *Physical Review Letters*, vol. 96, no. 22, p. 228301, 2006.

[153] S. Narayanan, D. R. Lee, A. Hagman, X. Li, and J. Wang, "Particle dynamics in polymer-metal nanocomposite thin films on nanometer-length scales," *Physical Review Letters*, vol. 98, no. 18, p. 185506, 2007.

[154] O. Oparaji, S. Narayanan, A. Sandy, S. Ramakrishnan, and D. Hallinan Jr, "Structural dynamics of strongly segregated block copolymer electrolytes," *Macromolecules*, vol. 51, no. 7, pp. 2591–2603, 2018.

[155] J. Moeller, M. Sprung, A. Madsen, and C. Gutt, "X-ray photon correlation spectroscopy of protein dynamics at nearly diffraction-limited storage rings," *Journal of Synchrotron Radiation*, vol. 6, no. 5, pp. 794–803, 2019.

[156] F. Perakis and C. Gutt, "Towards molecular movies with X-ray photon correlation spectroscopy," *Physical Chemistry Chemical Physics*, vol. 22, pp. 19443–19453, 2020.

[157] L. B. Lurio, G. M. Thurston, Q. Zhang, S. Narayanan, and E. M. Dufresne, "Use of continuous sample translation to reduce radiation damage for xpcs studies of protein diffusion," *Journal of Synchrotron Radiation*, vol. 28, no. 2, 2021.

[158] P. Vodnala, N. Karunaratne, L. Lurio, G. M. Thurston, M. Vega, E. Gaillard, S. Narayanan, A. Sandy, Q. Zhang, E. M. Dufresne, G. Foffi, P. Grybos, P. Kmon, P. Maj, and R. Szczygiel, "Hard-sphere-like dynamics in highly concentrated alpha-crystallin suspensions," *Physical Review E*, vol. 97, no. 2, p. 020601(R), 2018.

[159] Y. Chushkin, A. Gulotta, F. Roosen-Runge, A. Pal, A. Stradner, and P. Schurtenberger, "Probing cage relaxation in concentrated protein solutions by xpcs," *arXiv preprint arXiv:2203.12695*, 2022.

[160] P. J. Chung, Q. Zhang, H. L. Hwang, A. Leong, P. Maj, R. Szczygiel, E. M. Dufresne, S. Narayanan, E. J. Adams, and K. Y. C. Lee, "α-synuclein sterically stabilizes spherical nanoparticle-supported lipid bilayers," *ACS Applied Bio Materials*, vol. 2, no. 4, pp. 1413–1419, 2019.

[161] J. Möller, M. Reiser, J. Hallmann, U. Boesenberg, A. Zozulya, H. Rahmann, A.-L. Becker, F. Westermeier, T. Zinn, M. Sprung, *et al.*, "Using low dose X-ray speckle visibility spectroscopy to study dynamics of soft matter samples," *arXiv preprint arXiv:2106.14311*, 2021.

[162] B. D. Partain, Q. Zhang, M. Unni, J. Aldrich, C. M. Rinaldi-Ramos, S. Narayanan, and K. D. Allen, "Spatially-resolved nanometer-scale measurement of cartilage extracellular matrix mobility," *Osteoarthritis and Cartilage*, vol. 29, no. 9, pp. 1351–1361, 2021.

[163] D. Larobina, A. Pommella, A.-M. Philippe, M. Y. Nagazi, and L. Cipelletti, "Enhanced microscopic dynamics in mucus gels under a mechanical load in the linear viscoelastic regime," *Proceedings of the National Academy of Sciences*, vol. 118, no. 45, 2021.

[164] A. A. D'souza and R. Shegokar, "Polyethylene glycol (peg): a versatile polymer for pharmaceutical applications," *Expert opinion on drug delivery*, vol. 13, no. 9, pp. 1257–1275, 2016.

[165] D. I. Svergun, M. H. J. Koch, P. A. Timmins, and R. P. May, *Small Angle X-ray and Neutron Scattering from Solutions of Biological Macromolecules*. Oxford University Press, 2013.

[166] P. Lindner and T. Zemb, *Neutrons, X-rays, and Light: Scattering Methods Applied to Soft Condensed Matter*. Elsevier North-Holland, 2002.

[167] F. Mezei, *The principles of neutron spin echo*. Springer, 1980.

[168] M. Bée, *Quasielastic neutron scattering*. Adam Hilger, Bristol, 1988.

[169] L. van Hove, "Correlations in space and time and born approximation scattering in systems of interacting particles," *Physical Review*, vol. 95, no. 1, pp. 249–262, 1954.

[170] R. Brown, "Xxvii. a brief account of microscopical observations made in the months of june, july and august 1827, on the particles contained in the pollen of plants; and on the general existence of active molecules in organic and inorganic bodies," *The philosophical magazine*, vol. 4, no. 21, pp. 161–173, 1828.

[171] A. Fick, "über diffusion," *Annalen der Physik*, vol. 170, no. 1, pp. 59–86, 1855.

[172] G. H. Vineyard, "Scattering of slow neutrons by a liquid," *Physical Review*, vol. 110, no. 5, p. 999, 1958.

[173] F. Höfling and T. Franosch, "Anomalous transport in the crowded world of biological cells," *Reports on Progress in Physics*, vol. 76, no. 4, p. 046602, 2013.

[174] R. Bandyopadhyay, D. Liang, J. L. Harden, and R. L. Leheny, "Slow dynamics, aging, and glassy rheology in soft and living matter," *Solid State Communications*, vol. 139, no. 11, pp. 589–598, 2006.

[175] R. Metzler and J. Klafter, "The random walk's guide to anomalous diffusion: a fractional dynamics approach," *Physics Reports*, vol. 339, no. 1, p. 1, 2001.

[176] C. Caronna, Y. Chushkin, A. Madsen, and A. Cupane, "Dynamics of nanoparticles in a supercooled liquid," *Physical Review Letters*, vol. 100, no. 5, p. 055702, 2008.

[177] D. Comoletti, A. Grishaev, A. E. Whitten, I. Tsigelny, P. Taylor, and J. Trewhella, "Synaptic arrangement of the neuroligin/β-neurexin complex revealed by X-ray and neutron scattering," *Structure*, vol. 15, no. 6, pp. 693–705, 2007.

[178] G. Grübel, A. Madsen, and A. Robert, *X-ray Photon Correlation Spectroscopy (XPCS)*, pp. 953–995. Dordrecht: Springer Netherlands, 2008.

[179] G. Gruebel and F. Zontone, "Correlation spectroscopy with coherent X-rays," *J. Alloys Compd.*, vol. 362, no. 1–2, pp. 3–11, 2004.

[180] A. R. Sandy, Q. Zhang, and L. B. Lurio, "Hard x-ray photon correlation spectroscopy methods for materials studies," *Annual Review of Materials Research*, vol. 48, no. 1, 2018.

[181] O. Bikondoa, "On the use of two-time correlation functions for X-ray photon correlation spectroscopy data analysis," *Journal of Applied Crystallography*, vol. 50, no. 2, pp. 357–368, 2017.

[182] A. Madsen, A. Fluerasu, and B. Ruta, *Structural Dynamics of Materials Probed by X-ray Photon Correlation Spectroscopy*, pp. 1617–1641. Cham: Springer International Publishing, 2016.

[183] J. W. Goodman, *Statistical Properties of Laser Speckle Patterns*, pp. 9–75. Berlin, Heidelberg: Springer Berlin Heidelberg, 1975.

[184] A. Balerna and S. Mobilio, *Synchrotron Radiation: Basics, Methods and Applications*, ch. 1. Introduction to Synchrotron Radiation. Springer Berlin-Heidelberg, 2016.

[185] P. Vodnala, N. Karunaratne, S. Bera, L. Lurio, G. M. Thurston, N. Karonis, J. Winans, A. Sandy, S. Narayanan, L. Yasui, *et al.*, "Radiation damage limits to xpcs studies of protein dynamics," in *AIP Conference Proceedings*, vol. 1741, p. 050026, AIP Publishing LLC, 2016.

[186] P. Falus, L. Lurio, and S. Mochrie, "Optimizing the signal-to-noise ratio for X-ray photon correlation spectroscopy," *Journal of Synchrotron Radiation*, vol. 13, no. 3, pp. 253–259, 2006.

[187] A. Allahgholi, J. Becker, A. Delfs, R. Dinapoli, P. Goettlicher, D. Greiffenberg, B. Henrich, H. Hirsemann, M. Kuhn, R. Klanner, *et al.*, "The adaptive gain integrating pixel detector at the european xfel," *Journal of synchrotron radiation*, vol. 26, no. 1, pp. 74–82, 2019.

[188] T. Tschentscher, C. Bressler, J. Grünert, A. Madsen, A. P. Mancuso, M. Meyer, A. Scherz, H. Sinn, and U. Zastrau, "Photon beam transport and scientific instruments at the european xfel," *Applied Sciences*, vol. 7, no. 6, p. 592, 2017.

[189] F. Dallari, M. Reiser, I. Lokteva, A. Jain, J. Möller, M. Scholz, A. Madsen, G. Grübel, F. Perakis, and F. Lehmkühler, "Analysis strategies for mhz xpcs at the european xfel," *Applied Sciences*, vol. 11, no. 17, p. 8037, 2021.

[190] M. Hennig, B. Frick, and T. Seydel, "Optimum velocity of a phase-space transformer for cold-neutron backscattering spectroscopy," *Journal of Applied Crystallography*, vol. 44, no. 3, pp. 467–472, 2011.

[191] B. Frick, E. Mamontov, L. van Eijck, and T. Seydel, "Recent backscattering instrument developments at the ill and sns," *Zeitschrift für physikalische Chemie*, vol. 224, no. 1-2, pp. 33–60, 2010.

[192] O. Arnold, J. Bilheux, J. Borreguero, A. Buts, C. S.I., L. Chapon, M. Doucet, N. Draper, R. Ferraz Leal, M. Gigg, and V. Lynch, "Mantid data analysis and visualization package

for neutron scattering and micro-sr experiments," *Nuclear Instruments and Methods in Physics Research Section A: Accelerators, Spectrometers, Detectors and Associated Equipment*, vol. 764, no. 764, pp. 156–166, 2014.

[193] O. Matsarskaia, F. Baeuerle, C. Beck, S. Da Vela, A. Girelli, M. Grimaldo, F. Roosen-Runge, F. Schrieber, T. Seydel, and F. Zhang, "Determination of the short-time self-diffusion of antibodies approaching an arrested state.," 2020. Institut Laue-Langevin (ILL),DOI:10.5291/ILL-DATA.9-13-829.

[194] C. Beck, F. Baeuerle, O. Czakkel, A. Girelli, O. Matsarskaia, S. Prevost, F. Roosen-Runge, F. Schrieber, T. Seydel, and F. Zhang, "Determination of the short-time self-diffusion of antibodies approaching an arrested state.," 2020. Institut Laue-Langevin (ILL), DOI: 10.5291/ILL-DATA.9-13-879.

[195] Y. Liu, "Short-time dynamics of proteins in solutions studied by neutron spin echo," *Current Opinion in Colloid & Interface Science*, vol. 42, pp. 147 – 156, 2019.

[196] D. F. Griffiths and D. J. Higham, *Numerical methods for ordinary differential equations: initial value problems*. Springer Science & Business Media, 2010.

[197] R. C. Desai and R. Kapral, *Dynamics of Self-organized and Self-assembled Structures*. Cambridge University Press, 2009.

[198] S. Puri and Y. Oono, "Effect of noise on spinodal decomposition," *Journal of Physics A: Mathematical and General*, vol. 21, no. 15, p. L755, 1988.

[199] F. Corberi, G. Gonnella, and A. Lamura, "Spinodal decomposition of binary mixtures in uniform shear flow," *Physical Review Letters*, vol. 81, no. 18, p. 3852, 1998.

[200] P. Padilla and S. Toxvaerd, "Spinodal decomposition under shear flow," *The Journal of Chemical Physics*, vol. 106, no. 6, pp. 2342–2347, 1997.

[201] A. Onuki, "Phase transitions of fluids in shear flow," *Journal of Physics: Condensed Matter*, vol. 9, no. 29, p. 6119, 1997.

[202] A. Girelli, H. Rahmann, N. Begam, A. Ragulskaya, M. Reiser, S. Chandran, F. Westermeier, M. Sprung, F. Zhang, C. Gutt, and F. Schreiber, "Microscopic dynamics of liquid-liquid phase separation and domain coarsening in a protein solution revealed by

X-ray photon correlation spectroscopy," *Physical Review Letters*, vol. 126, p. 138004, Apr 2021.

[203] J. Berry, C. P. Brangwynne, and M. Haataja, "Physical principles of intracellular organization via active and passive phase transitions," *Reports on Progress in Physics*, vol. 81, no. 4, p. 046601, 2018.

[204] A. A. Hyman and C. P. Brangwynne, "Beyond stereospecificity: Liquids and mesoscale organization of cytoplasm," *Developmental Cell*, vol. 21, no. 1, pp. 14–16, 2011.

[205] L. Malinovska, S. Kroschwald, and S. Alberti, "Protein disorder, prion propensities, and self-organizing macromolecular collectives," *Biochimica et Biophysica Acta (BBA) - Proteins and Proteomics*, vol. 1834, no. 5, pp. 918–931, 2013.

[206] S. C. Weber and C. P. Brangwynne, "Getting rna and protein in phase," *Cell*, vol. 149, no. 6, pp. 1188–1191, 2012.

[207] J. Conrad, H. Wyss, V. Trappe, S. Manley, K. Miyazaki, L. Kaufman, A. Schofield, D. Reichman, and D. Weitz, "Arrested fluid-fluid phase separation in depletion systems: Implications of the characteristic length on gel formation and rheology," *Journal of Rheology*, vol. 54, no. EPFL-ARTICLE-182455, p. 421, 2010.

[208] T. Gibaud and P. Schurtenberger, "A closer look at arrested spinodal decomposition in protein solutions," *Journal of Physics: Condensed Matter*, vol. 21, no. 32, p. 322201, 2009.

[209] B. Jiang, J. G. Tsavalas, and D. C. Sundberg, "Water whitening of polymer films: Mechanistic studies and comparisons between water and solvent borne films," *Progress in Organic Coatings*, vol. 105, pp. 56–66, 2017.

[210] S. Kim, J. Huang, Y. Lee, S. Dutta, H. Y. Yoo, Y. M. Jung, Y. Jho, H. Zeng, and D. S. Hwang, "Complexation and coacervation of like-charged polyelectrolytes inspired by mussels," *Proceedings of the National Academy of Sciences*, vol. 113, no. 7, pp. E847–E853, 2016.

[211] H. Cai, B. Gabryelczyk, M. S. S. Manimekalai, G. Grüber, S. Salentinig, and A. Miserez, "Self-coacervation of modular squid beak proteins – a comparative study," *Soft Matter*, vol. 13, no. 42, pp. 7740–7752, 2017.

[212] A. S. Raut and D. S. Kalonia, "Pharmaceutical perspective on opalescence and liquid–liquid phase separation in protein solutions," *Molecular Pharmaceutics*, vol. 13, no. 5, pp. 1431–1444, 2016.

[213] A. R. Strom, A. V. Emelyanov, M. Mir, D. V. Fyodorov, X. Darzacq, and G. H. Karpen, "Phase separation drives heterochromatin domain formation," *Nature*, vol. 547, no. 7662, pp. 241–245, 2017.

[214] S. Ambadipudi, J. Biernat, D. Riedel, E. Mandelkow, and M. Zweckstetter, "Liquid–liquid phase separation of the microtubule-binding repeats of the alzheimer-related protein tau," *Nature Communications*, vol. 8, no. 1, pp. 1–13, 2017.

[215] S. E. Reichheld, L. D. Muiznieks, F. W. Keeley, and S. Sharpe, "Direct observation of structure and dynamics during phase separation of an elastomeric protein," *Proceedings of the National Academy of Sciences*, vol. 114, no. 22, pp. E4408–E4415, 2017.

[216] A. Boire, C. Sanchez, M.-H. Morel, M. P. Lettinga, and P. Menut, "Dynamics of liquid-liquid phase separation of wheat gliadins," *Scientific Reports*, vol. 8, no. 1, p. 14441, 2018.

[217] X. Lu, S. G. J. Mochrie, S. Narayanan, A. R. Sandy, and M. Sprung, "How a liquid becomes a glass both on cooling and on heating," *Physical Review Letters*, vol. 100, no. 4, p. 045701, 2008.

[218] Q. Zhang, D. Bahadur, E. M. Dufresne, P. Grybos, P. Kmon, R. L. Leheny, P. Maj, S. Narayanan, R. Szczygiel, S. Ramakrishnan, and A. Sandy, "Dynamic scaling of colloidal gel formation at intermediate concentrations," *Physical Review Letters*, vol. 119, no. 17, p. 178006, 2017.

[219] G. Brown, P. A. Rikvold, and M. Grant, "Universality and scaling for the structure factor in dynamic order-disorder transitions," *Physical Review E*, vol. 58, no. 5, pp. 5501–5507, 1998.

[220] M. Grimaldo, H. Lopez, C. Beck, F. Roosen-Runge, M. Moulin, J. M. Devos, V. Laux, M. Härtlein, S. Da Vela, R. Schweins, A. Mariani, F. Zhang, J.-L. Barrat, M. Oettel, V. T. Forsyth, T. Seydel, and F. Schreiber, "Protein short-time diffusion in a naturally crowded environment," *The Journal of Physical Chemistry Letters*, vol. 10, no. 8, pp. 1709–1715, 2019. PMID: 30897330.

[221] C. M. Jeffries, M. A. Graewert, D. I. Svergun, and C. E. Blanchet, "Limiting radiation damage for high-brilliance biological solution scattering: practical experience at the embl p12 beamline petraiii," *Journal of Synchrotron Radiation*, vol. 22, no. 2, pp. 273–279, 2015.

[222] H. Furukawa, "Dynamics-scaling theory for phase-separating unmixing mixtures: Growth rates of droplets and scaling properties of autocorrelation functions," *Physica A: Statistical Mechanics and its Applications*, vol. 123, no. 2, pp. 497–515, 1984.

[223] G. Williams and D. C. Watts, "Non-symmetrical dielectric relaxation behaviour arising from a simple empirical decay function," *Transactions of the Faraday Society*, vol. 66, no. 0, pp. 80–85, 1970.

[224] G. S. Fulcher, "Analysis of recent measurements of the viscosity of glasses," *Journal of the American Ceramic Society*, vol. 8, no. 6, pp. 339–355, 1925.

[225] H. Vogel, "Das Temperaturabhängigkeitsgesetz der Viskosität von Flüssigkeiten," *Physikalische Zeitschrift*, vol. 22, pp. 645–646, 1921.

[226] G. Tammann and W. Hesse, "Die Abhängigkeit der Viskosität von der Temperatur bei unterkühlten Flüssigkeiten," *Zeitschrift für anorganische und allgemeine Chemie*, vol. 156, no. 1, pp. 245–257, 1926.

[227] W. van Megen, S. M. Underwood, and P. N. Pusey, "Nonergodicity parameters of colloidal glasses," *Physical Review Letters*, vol. 67, no. 12, pp. 1586–1589, 1991.

[228] A. Jain, F. Schulz, I. Lokteva, L. Frenzel, G. Grübel, and F. Lehmkühler, "Anisotropic and heterogeneous dynamics in an aging colloidal gel," *Soft Matter*, vol. 16, no. 11, pp. 2864–2872, 2020.

[229] P. Ballesta, A. Duri, and L. Cipelletti, "Unexpected drop of dynamical heterogeneities in colloidal suspensions approaching the jamming transition," *Nature Physics*, vol. 4, no. 7, pp. 550–554, 2008.

[230] Z. W. Wu, W. Kob, W.-H. Wang, and L. Xu, "Stretched and compressed exponentials in the relaxation dynamics of a metallic glass-forming melt," *Nature Communications*, vol. 9, no. 1, p. 5334, 2018.

[231] J. W. Cahn, "Phase separation by spinodal decomposition in isotropic systems," *The Journal of Chemical Physics*, vol. 42, no. 1, pp. 93–99, 1965.

[232] D. M. Mitrea and R. W. Kriwacki, "Phase separation in biology; functional organization of a higher order," *Cell Communication and Signaling*, vol. 14, no. 1, p. 1, 2016.

[233] A. Girelli, C. Beck, F. Bäuerle, O. Matsarskaia, R. Maier, F. Zhang, B. Wu, C. Lang, O. Czakkel, T. Seydel, F. Schreiber, and F. Roosen-Runge, "Molecular flexibility of antibodies preserved even in the dense phase after macroscopic phase separation," *Molecular Pharmaceutics*, vol. 18, no. 11, pp. 4162–4169, 2021. PMID: 34637319.

[234] M. Grimaldo, F. Roosen-Runge, N. Jalarvo, M. Zamponi, F. Zanini, M. Hennig, F. Zhang, F. Schreiber, and T. Seydel, "High-resolution neutron spectroscopy on protein solution samples," *EPJ Web of Conferences*, vol. 83, p. 02005, 2015.

[235] F. Volino, J.-C. Perrin, and S. Lyonnard, "Gaussian model for localized translational motion: application to incoherent neutron scattering," *The Journal of Physical Chemistry B*, vol. 110, no. 23, pp. 11217–11223, 2006.

[236] M. Hennig, F. Roosen-Runge, F. Zhang, S. Zorn, M. W. A. Skoda, R. M. J. Jacobs, T. Seydel, and F. Schreiber, "Dynamics of highly concentrated protein solutions around the denaturing transition," *Soft Matter*, vol. 8, pp. 1628–1633, 2012.

[237] C. Lindsey and G. Patterson, "Detailed comparison of the williams–watts and cole–davidson functions," *The Journal of Chemical Physics*, vol. 73, no. 7, pp. 3348–3357, 1980.

[238] M. Reiser, A. Girelli, A. Ragulskaya, S. Das, S. Berkowicz, M. Bin, M. Ladd-Parada, M. Filianina, H.-F. Poggemann, N. Begam, *et al.*, "Resolving molecular diffusion and aggregation of antibody proteins with megahertz X-ray free-electron laser pulses," *arXiv preprint arXiv:2202.10889*, 2022.

[239] G. Foffi, G. Savin, S. Bucciarelli, N. Dorsaz, G. M. Thurston, A. Stradner, and P. Schurtenberger, "Hard sphere-like glass transition in eye lens alpha-crystallin solutions," *Proceedings of the National Academy of Sciences*, vol. 111, no. 47, pp. 16748–16753, 2014. 10.1073/pnas.1406990111.

[240] M. J. Saxton, "A biological interpretation of transient anomalous subdiffusion. i. qualitative model," *Biophysical journal*, vol. 92, no. 4, pp. 1178–1191, 2007.

[241] M. Stransky, Z. Jurek, C. Fortmann-Grote, L. Juha, R. Santra, B. Ziaja, A. P. Mancuso, *et al.*, "Effects of radiation damage and inelastic scattering on single-particle imaging of hydrated proteins with an X-ray free-electron laser," *Scientific reports*, vol. 11, no. 1, pp. 1–11, 2021.

[242] E. M. Herzig, A. Robert, D. van't Zand, L. Cipelletti, P. Pusey, and P. S. Clegg, "Dynamics of a colloid-stabilized cream," *Physical Review E*, vol. 79, no. 1, p. 011405, 2009.

[243] G. Foffi, C. De Michele, F. Sciortino, and P. Tartaglia, "Arrested phase separation in a short-ranged attractive colloidal system: A numerical study," *The Journal of Chemical Physics*, vol. 122, no. 22, p. 224903, 2005.

[244] F. Lehmkühler, F. Dallari, A. Jain, M. Sikorski, J. Möller, L. Frenzel, I. Lokteva, G. Mills, M. Walther, H. Sinn, *et al.*, "Emergence of anomalous dynamics in soft matter probed at the European XFEL," *Proceedings of the National Academy of Sciences*, vol. 117, no. 39, pp. 24110–24116, 2020.

[245] H. Tanaka, "Viscoelastic phase separation," *Journal of Physics: Condensed Matter*, vol. 12, no. 15, p. R207, 2000.